Two-component Bose-Einstein condensates with competing interactions

by

Julio Sanz Sánchez

A thesis submitted in fulfillment of the requirements for the degree of Doctor of Philosophy in Photonics

Thesis supervisor: Prof. Dr. Leticia Tarruell
Ultracold Quantum gases group

The Barcelona Institute of Science and Technology - BIST
Institut de Ciències Fotòniques - ICFO
Universitat Politècnica de Catalunya - UPC

Dedicada a la meva família,
a la meva parella,
i als meus amics.

"Ojalá nuestra tecnología nunca deje atrás nuestra filosofía.
Ojalá nuestro poder nunca supere nuestra compasión.
Y que el motor del cambio no sea el miedo, sino el amor."
Edmond Kirsch

Abstract

This thesis reports the experimental study of two-component Bose-Einstein condensates with tunable interactions, which are exploited as a platform to perform quantum simulation of many-body quantum systems.

To perform this experiments, we have implemented an atomic source consisting on a glass cell 2D MOT vacuum chamber and a high resolution optical system to image and manipulate the atoms. Furthermore, we develop and characterize a polarization phase contrast technique which is able to probe optically dense atomic mixtures at intermediate and high magnetic fields in open transitions. This technique has been used to either probe the total column density of a two-component atomic cloud or the difference in column density between both components.

We report on the first observation of composite quantum liquid droplets in an incoherent mixture with residual mean field attraction. Strikingly, this novel phase is stabilized due to the repulsive beyond mean field corrections in a weakly interacting system. Moreover, we have characterized the liquid to gas phase transition which occurs for small atom numbers.

Additionally, we have compared two different self-bound states in a quasi-1D geometry with incoherent mixtures: quantum droplets and bright solitons. Depending on the atom number and interaction strengths both states can be smoothly connected through a crossover or be distinct entities separated by a transition. We have measured its composition, its phase diagram and mapped out the soliton to droplet transition.

Finally, we report on a technique to modify the elastic and inelastic inter-

actions in a two-component Bose-Einstein condensate with very unequal and competing interactions under the presence of strong coherent coupling. This technique provides a wide flexibility and has allowed us to observe bright solitons in quasi-1D in a coherently coupled dressed state. We exploit the fast temporal control of the effective interactions to quench them into the attractive regime and study the resulting modulational instability which develops into a bright soliton train.

Resum

Aquesta tesi descriu l'estudi experimental d'una mescla de dos condensats de Bose-Einstein amb interaccions ajustables. Aquest sistema és utilitzat com una plataforma per a estudiar sistemes quàntics formats per moltes partícules a partir de la simulació quàntica.

Per a fer aquests experiments, he construït una font atòmica formada per una trampa magneto-òptica en 2D que s'implementa en una cambra de buit feta de vidre. A més a més, he desenvolupat i caracteritzat una tècnica d'imatge de contrast de fase basada en la rotació de la polarització de la llum. Aquesta tècnica està preparada per fer imatges de mescles atòmiques a camps magnètics intermedis i alts amb una gran densitat òptica i amb transicions òptiques obertes. Hem utilitzat la tècnica per a mesurar la densitat integrada total en l'eix òptic així com la diferència entre ambdues components.

Es descriu la primera observació de gotes líquides quàntiques compostes per dues components incoherents amb una atracció residual en l'aproximació de camp mitjà. Sorprenentment, aquesta nova fase està estabilitzada a causa de la repulsió generada per les correccions de l'energia més enllà de l'aproximació de camp mitjà en un sistema amb interaccions dèbils. També hem caracteritzat la transició de fase líquid-gas que succeeix quan el sistema té un nombre d'àtoms reduït.

A més a més, hem comparat dos estats autoconfinats de diferent natura en una geometria quasi-1D amb una mescla d'àtoms incoherents: les gotes quàntiques i els solitons brillants. Segons el nombre d'àtoms i la força de les interaccions aquests estats poden estar connectats o bé suaument o bé per una transició de fase. Hem mesurat la seva composició, el diagrama de fases i hem traçat el mapa

de transició entre solitons i gotes en funció del camp magnètic i nombre d'àtoms.

Finalment, es descriu una tècnica per a modificar les interaccions elàstiques i inelàstiques en un condensat de Bose-Einstein format per dues components, amb interaccions diferents i en competició, coherentment acoblades. Aquesta tècnica ens proveeix d'una gran flexibilitat per a modificar les interaccions i ens ha permès observar solitons brillants en quasi-1D en un estat vestit per l'acoblament coherent. Hem utilitzat l'habilitat per a modificar temporalment les interaccions per a fer un canvi brusc de les interaccions cap al règim atractiu i estudiar la inestabilitat dels modes que es manifesta amb la formació d'un tren de solitons brillants.

List of publications

- C. R. Cabrera, L. Tanzi, J. Sanz, B. Naylor, P. Thomas, P. Cheiney, and L. Tarruell. Quantum liquid droplets in a mixture of Bose-Einstein condensates. Science **359**, 301 (2018)

- P. Cheiney, C. R. Cabrera, J. Sanz, B. Naylor, L. Tanzi, and L. Tarruell. Bright soliton to quantum droplet transition in a mixture of Bose-Einstein condensates. Phys. Rev. Lett. **120**, 135301 (2018)

- L. Tanzi, C. R. Cabrera, J. Sanz, P. Cheiney, M. Tomza, and L. Tarruell. Feshbach resonances in potassium Bose-Bose mixtures. Phys. Rev. A **98**, 062712 (2018)

- J. Sanz, A. Frölian, C. S. Chisholm, C. R. Cabrera, and L. Tarruell. Interaction control and bright solitons in coherently-coupled Bose-Einstein condensates. *Under peer review in Phys. Rev. Lett.*, preprint: arXiv:1912.06041

- C. R. Cabrera, J. Sanz, L. Tanzi, P. Cheiney, L. Tarruell. Dual Bose-Einstein condensation of ^{39}K-^{41}K. *In preparation.*

Acknowledgements

My story with the ultracold quantum gases group from ICFO started on 2014. I was finishing my bachelor studies. I was very curious about quantum physics and hesitating whether to focus on theory or experiments. I will always be grateful to Verònica Ahufinger and Jordi Mompart, who motivated me to study atomic and molecular physics in the ultracold quantum gases group from Leticia Tarruell at ICFO. At some point in life, you realize that one tends to be passionate about the topics that are taught by good professors. Certainly, they were fundamental in making me discover the passion about quantum physics. Professor Xavier Álvarez was the initial responsible for making me love physics. Thank you a lot for igniting my curiosity about nature. Among one of our conversations, he told me that having the bachelor in Physics and being a physicist was not the same thing. Honestly, at the time, I was not able to understand what he meant.

In 2014, I visited Leticia Tarruell at ICFO. She convinced me that I must become an experimentalist and gave me the opportunity to work in the ultracold quantum gases team. I barely had any experimental experience but still she gave me the chance to join the team. During all this time, you have really shown me what it means to be a physicist. From aligning a fiber to reviewing carefully my thesis manuscript, you have dedicated your time at each step in this adventure to help me grow as a scientist and as a person. For all the patience, motivation and positivism that you have transmitted me, from the best to the worst moments, and all the inspiring scientific discussions, I am extremely welcome, Leticia.

In this journey, I started working in the lab with the postdocs Pierrick Cheiney, Luca Tanzi and the PhD student César Cabrera. They have been the main people who showed me all the experimental techniques and tricks I know. Not only their expertise was fundamental for me to gain technical knowledge but to learn how to manage time and take decisions in such competitive environment. During this period, we went through some difficult times. I owe you the no surrender attitude and the team spirit to overcome all the challenges that we faced. Certainly, the 'futbolito' and beers in the 'chiringuito' also helped in keeping the team spirit high and, among many stories, make me enjoy all this time at ICFO. A huge thank you for everything!

Later on, I shared time in the lab with the postdoc Bruno Naylor and the PhD student Anika Frölian. Among many things that I learned thanks to Bruno, I finally understood two major things: the level structure of the atom and the 'level structure' of society. I thank you a lot for all the useful scientific and political discussions that enriched me both from the professional and personal point of view. At the time, we had a major accident in the experiment. The impact factor of such incident in my learning process at ICFO has been by far greater than that of any published results used to evaluate my success. Among all the team who helped to rebuild the experiment, I want to thank especially Anika. Besides all the pressure that I put you through, you kept pushing and were essential to revive the Fenix from its ashes. Moreover, together with the PhD student Craig Chisholm, who joined few months later, you have made my life extremely easy, becoming the new masters of the machine very fast. With you, Anika and Craig, I feel like the baby is in very good hands for long time. I also owe Craig many tricks about programming tricks and rf sources.

Around a year ago, the master student David Jacobs and the PhD student Jonathan Höschele started a new lab with Strontium. I wish I could have spent more time with you hand on hand in the lab. Still, it was a pleasure to have you in the team. I must admit that after some time seeing team members leave I was starting to be sad. This feeling changed for me after you arrived. Together with Anika and Craig you have been part of a new team generation who made my time at ICFO very fun. In this new generation, I am also very grateful to have shared time with the postdocs Ramón Ramos, Elletra Neri and Vasily Makhalov. You have suddenly provided a great deal of expertise to the Potassium and Strontium labs and have become essential members of the QGE family. From ICFO calçotadas, long discussions over lunch to the ICFO parties... I will keep great memories from all of you!

During all this time, I have also shared a fantastic time working with other people. I keep great memories from the always smiley Lisa Saemisch. Jordi Sastre master of Signadyne. The refined humor of Vincent (the 2^{nd}) Brunaud. The funny summers with Íñigo Urtiaga and Alberto Muñoz playing with the DMD. The lattice and language master Phillip Thomas. The amazing time with Teo Gil and Daniel Allepuz building the magnetic field stabilization and measuring

the aberrations of the DMD and the Raman master Manon Ballu. I also had the pleasure to meet the former team members Vincent (the 1^{st}) Lienhard and Manel Bosch. I am thankful for all these time at ICFO sharing good memories with you and learning from you.

The experimental work that we carried out during this time would not have been possible without the help of Xavier Menino, the mechanical workshop team, Jose Carlos Cifuentes and the electronic workshop team. They have been paramount not only in providing good advice and constructing all the devices that we use in the lab, but on teaching me mechanical and electronics design. I am also thankful to the IT, purchasing, logistics, maintenance and administration department who have made my work at ICFO extremely easy. I will especially remember Mika, Santi, Magda, Carlos, Luís and Núria.

Especial thanks to the members of the PhD committee Professor Luis Santos, Jordi Boronat and Thomas Bourdel for the very careful reading of the manuscript and the flattering reports. I have also had the pleasure of sharing very inspiring discussions on quantum droplets throughout my PhD with you. I will always be thankful for that.

My work during the PhD would not have been possible without my family, partner and friends. Com bé sabeu, el doctorat ha estat emocionalment com una montanya russa per a mi. A la meva familia, la meva parella i els meus amics us dedico aquesta tesi per tota la vostra estima i paciència per a treure'm un somriure en tot moment.

Als meus pares els ho dec tot. Vosaltres m'heu educat com sóc i m'heu portat fins aquí. M'heu ensenyat a ser perseverant, a tenir paciència, a treballar dur, a ser humil, a aixecar-me quan he caigut... M'heu fet veure quan m'ofegava en un got d'aigua i m'ho heu posat tot fàcil per a ser feliç. Infinites gràcies per tot!

A l'Alexandra, la meva parella, li estaré sempre agraït. Tú me has acompañado en todo momento en este trayecto de emociones durante estos años. Has sido mi balanza para mantenerme en pie cuando lo he pasado mal y me has sostenido todo este tiempo. Sin duda, eres la persona con la que más he pagado el estrés injustamente, y aun así has sido siempre paciente y comprensiva conmigo. Me has hecho muy feliz durante todo este tiempo y me has convencido día a día que todo este esfuerzo ha valido la pena. Te estaré eternamente agradecido. También

le agradezco muchísimo a tu familia todo el apoyo que me habéis dado. Por tratarme como a un hijo más. Mulțumesc mult.

Als meus amics del Maresme els agraeixo tots els moments viscuts. Heu sigut fonamentals per a fer-me feliç, evadir-me de l'estrés del doctorat i compartir alegries. Des dels festivals, les Santes, els Pirates, partits de futbol, paddle, barbacoes, aniversaris, divendres de barof i casal, els Z, nits de jocs de taula i vicis i mil i una històries. Moltes gràcies per tot! Sou molt grans!

Quiero agradecer especialmente a todos los amigos que me han apoyado todo este tiempo en Castelldefels. Érase una vez, una madrileña, un vasco y un catalán en un ático en avenida Constitució... evidentemente la historia no podía terminar más que en un cachondeo constante! A Sandra y Ugaitz, siempre enérgicos y alegres, habéis sido un ejemplo de motivación para mi y un apoyo fundamental durante estos años. Por todas las charlas de desayuno y cena en pijama. ¡Os echaré muchísimo de menos! To the best neighbors Pamina and Kavitha, adventurous and charming. For all the affection and support that you gave me and all the fun we had together during this time. Thank you! To Álvaro, Jose, Eduardo, Catherina, Anuja, Vikas and Rinu. Always ready to hang out, gossip and have fun. Thanks a lot!

Finalmente, quiero agradecer al Ministerio de Economía y Competitividad de España por concederme la beca de Formación de Personal Investigador que me ha permitido realizar los estudios de doctorado.

Contents

Introduction

Quantum simulation with ultracold quantum gases

The physical principles of the microscopic world are described by the laws of quantum mechanics. The understanding of these laws opened the so-called first quantum revolution, with the ground breaking invention of devices such as the laser and the semiconducting transistor, which have shaped our society in previously unimaginable ways. It was the underlying curiosity of human nature that has pushed our limits to understand and control condensed matter at the smallest scales.

In order to be able to do so, we need to understand the behavior of many interacting particles. Nowadays, using a classical computer we can simulate the physics of few particles. However, there are many degrees of freedom that must be taken into account. Thus, simulating the quantum mechanical behavior of many particles would require a gigantic computer memory and a very large amount of time. Although, the miniaturization of the transistors has offered scientists more powerful computing resources during a few decades [1], in most cases it is not enough to simulate many body interacting condensed matter systems. Prime examples are high-T_c superconductors [2], liquid Helium [3], frustrated spin systems [4] and neutron stars [5] among others. An alternative was proposed by Richard Feynman, who suggested that in order to simulate the physics of a quantum many body system we should use a quantum machine that could imitate it [6]. In other words, to simulate a quantum system we need a quantum simulator.

Since then, many experimental platforms have been used to simulate the physics of quantum systems such as trapped ions, photonic circuits, superconducting artificial atoms, and ultracold quantum gases [7]. In particular, in our experiment we perform quantum simulation with ultracold quantum gases with neutral atoms of potassium.

One of the main challenges to manipulate and understand the quantum mechanical behavior of interacting particles is the length scale at which quantum mechanics starts to play a fundamental role. This length scale corresponds to the so-called de Broglie wavelength $\lambda = h/p$, where λ is the wavelength associated to a particle with momentum p and h is the Planck constant. If the mean inter-particle distance of a system is on the order of the de Broglie wavelength, the wave nature of particles becomes relevant, and the particles start to behave coherently. At room temperature, this length scale is on the order of 0.1-1 Å. Hence, at room temperature, it is very challenging to observe and control the matter at such length scales.

The main strategy behind using ultracold quantum gases is to reduce the de Broglie wavelength associated to the particles by reducing the temperature of the cloud. Therefore, by cooling atoms at temperatures on the order of tens of nanokelvin, we can reach the quantum degenerate regime in systems which are ultra-dilute. Their typical densities are on the order of $10^{20}\,\mathrm{m}^{-3}$ and the inter-particle distances are on the order of a $1\,\mu$m. Consequently, we cannot only directly observe quantum phenomena in the macroscopic world with the help of optical microscopes but also manipulate it with laser light.

Thanks to the development of laser cooling [8–10] and evaporative cooling techniques [11, 12], the quantum degenerate regime was first achieved in Bose-Einstein condensates (BEC) [13, 14] and later on in Degenerate Fermi gases (DFG) [15]. As already mentioned, at ultracold temperatures, this regime is reached with very low densities. In the ultra-dilute regime the inter-particle distance l is much larger than the interaction range of the atomic potential r_0. In this regime, the interactions of the system can be described by a single parameter: the scattering length a.

Quantum simulation beyond the mean field approximation

For weakly interacting gases, where $l \gg a$ the description of the system can be simplified with a mean field approximation, which considers the interaction of a particle with the rest as an average effective potential. Therefore, the many-body problem can be simplified to an effective single particle problem. In order to observe beyond mean field effects there have been mainly two strategies.

On the one hand, the strongly interacting limit can be reached by tuning the scattering length so that $l \ll a$ thanks to Feshbach resonances [16]. Initial studies focused on the study of the unitary Fermi gas and the Bose-Einstein condensate to Bardeen-Cooper-Schrieffer crossover (for a review, see reference [17] and references therein). In Fermi gases, the Pauli exclusion principle forbids the presence of three and few body correlations. Hence, three-body recombination is suppressed and the Fermi gas is long lived. On the contrary, more than two body correlations play an important role on strongly interacting Bose gases. One of the first experiments to measure beyond mean field corrections to the energy of a Bose gas was performed in a regime where the energy of the system can be expanded perturbatively on the gas parameter na^3, where $n \propto l^{-3}$ is the density of the cloud. Very precise measurements of the equation of state of the gas were required to observe the first correction to the energy, the so-called Lee-Huang-Yang (LHY) correction, because it produces only a small shift to the mean field energy [18]. In the strongly interacting limit, three-body recombination processes lead to inelastic losses. Several approaches have been taken so far to circumvent this issue. Experiments in JILA [19] and Aahrus [20], probed few impurities that strongly interact ($na_{IB}^3 \gg 1$) with a weakly interacting Bose-gas ($na_B^3 \ll 1$), where a_{IB} is the scattering length between the impurities and the bath and a_B is the scattering length of particles in the bath. In this regime three-body losses are only a few per cent of the total atom number. The problem gets more challenging when the complete system strongly interacts ($na^3 \gg 1$). In this case experiments probing the system on a very short timescale are required, as done in JILA [21] and Cambridge [22]. Other alternatives were based on the measurement of three-body loss rates as it was done in ENS [23] and Cambridge [24].

On the other hand, beyond mean field effects can be observed without reaching the strongly interacting regime in optical lattices. In this case, the physics of the system are described by the Hubbard model. The strategy to observe strong correlations beyond the mean field approximation is to reduce the tunneling between neighboring sites, corresponding to the kinetic energy term, so that it is much smaller than the on-site interaction. Using this method M. Greiner *et al.* [25] observed the transition from a superfluid to a strongly correlated Mott insulator with bosons, A. Mazurenko *et al.* observed a long-range order Fermi-Hubbard anti-ferromagnet [26]. For a review, see reference [27].

Attractive Bose-Einstein condensates with competing interactions

In this thesis, we present an alternative way to study beyond mean field effects by working with quantum mixtures with competing interactions. In 2015, D. Petrov proposed that quantum fluctuations could stabilize a Bose-Bose mixture with effective attractive interactions into an ultradilute quantum liquid droplet [28]. In this system, repulsive intra-component interactions and attractive inter-component interactions can be tuned in such a way that the mean field contribution to the energy remains weakly attractive and comparable to the zero point motion energy caused by quantum fluctuations [28]. As a consequence, even though the beyond mean field contribution to the energy remains very small, it is able to stabilize the system into a self-bound quantum liquid droplet, as it has been observed with ^{39}K mixtures by our group [29, 30] and the LENS group [31]. Analogous quantum droplets have been observed in a system with anisotropic interactions: with dipolar gases of ^{164}Dy [32, 33], ^{166}Er [34] and ^{162}Dy [35].

Moreover, Bose-Einstein condensates with attractive mean-field interactions can also host another kind of self-bound states, bright solitons. These were previously observed with attractively interacting single component BECs in a quasi-1D geometry with ^{7}Li [36–38], ^{85}Rb [39–41], ^{39}K atoms [42] and ^{133}Cs [43]. In this case, the stabilization stems from the balance between attractive interactions and the repulsive quantum pressure. Hence, in a similar fashion as

for optical solitons [44, 45], the quantum pressure plays the role of dispersion and the attraction serves as a stabilizing non-linearity which keeps the system self-bound.

In this thesis, we have studied the interplay between quantum droplets and bright solitons in a quantum Bose-Bose mixture [30]. Whereas the stabilization of quantum droplets has a quantum many-body origin [28], the stabilization of bright solitons stems from quantum pressure, which is a single particle effect. Bright solitons and quantum droplets are *a priori* distinct states which exist in very different regimes. Solitons require the gas to remain effectively one-dimensional, which limits their maximal atom number [46–48]. In contrast, droplets are three-dimensional solutions that exist even in free space and require a minimum atom number to be stable [28, 29, 33, 34, 49, 50]. Until our work was published, quantum droplet experiments focused exclusively on systems where solitons were absent, enabling an unambiguous identification of the droplet state. Therefore, they could not provide any insights on their connections to solitons.

Furthermore, the interactions of two-component BECs can be modified in the presence of coherent coupling. In references, [51, 52] it was shown that the interaction strength of a coherently coupled state is a linear combination of the intra and inter-component interaction strengths and depends on the parameters of the coupling field. This technique was initially used by the Oberthaler group to explore the different dynamics and transition between the Rabi and Josephson regimes, where the coupling and interaction energies dominate respectively [53]. Further experiments focused on the study of the phase separation dynamics of a coherently coupled BEC (which were initially observed in a non-coherent mixture in reference [54]) due to the modification of the interactions in the presence of coherent coupling [55–57] and spin orbit coupling [58–60].

In my thesis, we have studied a two-component Bose-Einstein condensate with very unequal interactions in the strong coherent coupling regime, also known as the Rabi regime. This technique provides a flexible control of both the elastic and inelastic collisions. We have performed the first direct measurement of the modification of the elastic and inelastic scattering properties of the gas. Whereas elastic collisions do not modify the two-particle dressed states, inelastic collisions do. In the latter process, the atoms decay into a correlated atom pair in

a similar fashion as in other in cold atoms inelastic collisonal processes [61–64]. Furthermore, we can tune the interactions into the attractive regime. Hence, in a quasi-1D geometry we can produce single bright solitons formed by atoms in a dressed state. Moreover, by means of coherent coupling the interactions can be temporally controlled. We use this feature to quench the effective interactions of dressed atoms into the attractive regime. Consequently, a modulational instability develops due to the exponential enhancement of density fluctuations, ending up in a soliton train.

Outline of the thesis

This thesis has been carried out on the Ultracold Quantum gases group led by L. Tarruell at the Institute of Photonic Sciences. I arrived to the group as a master student without any experimental experience in October of 2014. I followed the construction of the main experimental apparatus while working on the design of a high resolution objective and learning the basic experimental techniques on electronics, optical design and laser technology. This experiment was mainly designed and constructed by C. R. Cabrera, P.Cheiney, L. Tanzi and L. Tarruell, and the description of the design and development of the experimental apparatus can be found in the thesis of my predecessor C. R. Cabrera [65]. During this period, we achieved the first Bose-Einstein condensate of Spain with ^{41}K. In November of 2015, I started my PhD in the group. In the following, I outline the organization of the manuscript which describes the main research which I have carried out, together with the potassium team, during the completion of this thesis.

- In **chapter 1** we describe the upgrades which I performed in the experimental apparatus. First of all, I present a brief summary of the experimental cooling sequence that we used to cool down to degeneracy the bosonic mixture of ^{39}K-^{41}K. Then, I present the design and installation of a new glass cell 2D MOT chamber which was installed to remove a previously leaking stainless-steel 2D MOT chamber. Finally, I describe the design, installation and characterization of an optical set-up for imaging and addressing atoms with high resolution.

- In **chapter 2**, we present a polarization phase contrast technique which we have used to image two-component potassium BECs in open transitions at high magnetic field. This technique has been crucial to perform the experiments developed in the following chapters.

- In **chapter 3**, we present the first observation of composite quantum liquid droplets, which are stabilized by quantum fluctuations. We study its stabilization mechanism and characterize its liquid to gas phase transition.

- In **chapter 4**, we study the similarities and differences between composite quantum droplets and bright solitons in a quasi-1D geometry. We measure the composition of the self-bound states and its phase diagram. We distinguish two regions separated by a critical interaction strength, above there is a crossover between the two types of solutions, below we are able to map out the soliton to droplet phase transition.

- In **chapter 5**, we study the modification of the interactions in a two-component Bose-Einstein condensate in the presence of strong coherent coupling. We perform direct measurements of the modification of the elastic and inelastic scattering across the resonance. Moreover, we are able to produce dressed state bright solitons and study the modulation instability which occurs when the interactions are quenched, resulting in a soliton train.

- Finally, we present the conclusions and discuss future perspectives of the experiment.

Chapter 1

The potassium experiment

Abstract

In this chaper, we introduce the cooling sequence which we use the cool the bosonic isotopes of potassium down to quantum degeneracy. For the first time, we have been able to condense the ^{39}K-^{41}K mixture. During my thesis, we have replaced a leaky stainless steel 2D MOT chamber by a new glass cell chamber which presents better performance. We present the design and developed a custom-made high resolution optical set-up for imaging and addressing the atoms *in situ*. Finally, we detail the modification of the cooling sequence which were performed due to the experimental upgrades.

1.1 Introduction

In our experiment we perform quantum simulation with ultracold potassium atoms. This atom was chosen for several reasons. First of all, potassium is an alkali atom, with only one electron in its valence band [66]. Thus, it is very simple to cool and manipulate potassium as compared to dipolar or two-electron atoms. Indeed, its two bosonic (^{39}K and ^{41}K) and fermionic (^{40}K) isotopes have been cooled down to the quantum degenerate regime [67–69]. Therefore, potassium is a very good candidate to study Bose-Bose, Bose-Fermi and Fermi-Fermi

mixtures. Moreover, potassium offers the possibility to control the interactions for each isotope and between different isotopes (^{40}K-^{41}K and ^{39}K-^{41}K) [70–75]. Since the mass of the different isotopes is very similar, the gravitational sag between them is very small and we do not need to have species dependent trapping potentials to have a good overlap between them.

Initially, my research in the potassium experimental apparatus started by producing a BEC of ^{39}K and dual BECs of ^{39}K and ^{41}K, which was achieved on January of 2016, and characterizing the Feshbach resonances of potassium Bose-Bose mixtures [75]. The complete description of the cooling sequence that we use to condense all the bosonic isotopes and the study of the Feshbach resonances can be found in the thesis of C. R. Cabrera [65] and in reference [75]. In the mean time, I kept working on the prototyping of the high resolution objective in order to be able to install it in the experiment to include a key tool of our research: the *in situ* imaging of potassium mixtures. The installation of the imaging objective was done in June of 2016, and it allowed us to proof the existence of quantum droplets [29] and show its interplay with composite bright solitons [30]. This works were completed around the fall of 2017 with the Sword of Damocles on top: a leaky 2D MOT steel chamber. In November of 2017, we upgraded our 2D MOT with a glass cell chamber. Moreover, we installed a second high resolution objective to be able to produce highly resolved optical potentials on the atoms.

The experimental chapter is organized as follows. In section 1.2 we briefly introduce the experimental apparatus and cooling strategy for condensing the bosonic isotopes of potassium. In section 1.3 we describe the 2D MOT upgrade. In section 1.4 we show the design, development and installation of two high resolution objectives to image and address potassium mixtures. In section 1.6 we present the conclusions and future experimental upgrades planned for the next years.

1.2 Experimental apparatus and cooling sequence

In this section, we give an overview of the experimental set-up and the experimental routine to cool down the atoms before the main upgrades of the experimental apparatus were performed.

The experimental set-up is divided into two different parts: a laser system where we prepare the frequencies required to laser cool, manipulate and probe the atoms, and a vacuum chamber where the production of a quantum degenerate gas takes place, see Fig. 1.1 (a).

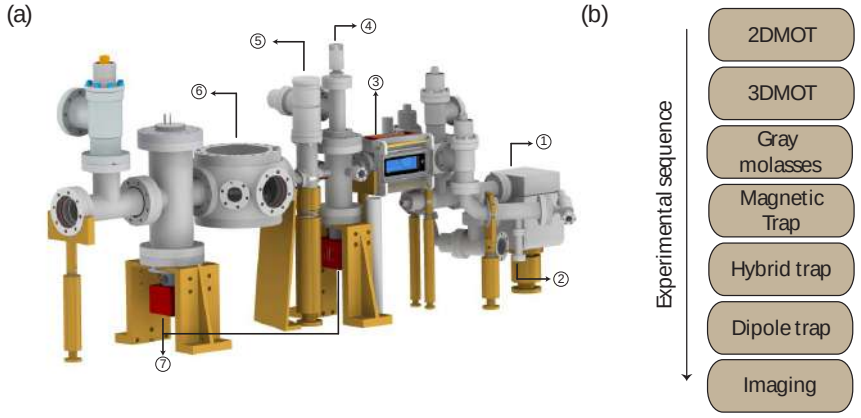

Figure 1.1: Old experimental apparatus. (a) 1. Ion pump. 2. Potassium source. 3. Stainless steel 2D MOT chamber. 4. Mechanical shutter connected to a cross where the 2D MOT (3) connects through a differential pumping tube. 5. Gate valve. 6. 3D MOT/science chamber. 7. Getter pumps. (b) Schematic of the experimental sequence. We perform a dual (^{39}K-^{41}K) laser cooling process consisting of a 2D MOT, 3D MOT and molasses. Both species are optically pumped and evaporatively cooled sequentially in a magnetic, hybrid and dipole trap until quantum degeneracy is reached. ^{39}K is sympathetically cooled in the magnetic trap through the thermal contact and good collision rate with ^{41}K. While ^{41}K can be cooled at zero field due to its positive background scattering length, ^{39}K is evaporatively cooled near a Feshbach resonance in the dipole trap due to its negative background scattering length. The atomic clouds are imaged either in time of flight or *in situ*.

The laser system to cool potassium consists on several lasers which are either close to the D2 (766.7007 nm) or D1 (770.7009 nm) transition from potassium ^{39}K. Two external cavity diode lasers[1] (ECDL) are locked on the D1 and D2 crossover lines of ^{39}K by using saturated absorption spectroscopy in two hot potassium vapor cells [65, 76]. Two Distributed FeedBack[2] (DFB) lasers are offset locked from the D2 master laser and are used, together with Acusto-Optic Modulators (AOM), as cooler and repumper lasers for the ^{41}K isotope. Their light is amplified with two independent Tappered Amplifiers (TA) and the light is coupled to a 4 by 4 fiber cluster which mixes the light generated from the laser table and sends it to the experimental apparatus table. An ECDL is offset locked from the D1 master laser and together with Electro Optical Modulators (EOM) and AOMs is used to do the molasses of ^{41}K and optical pumping of ^{41}K and ^{39}K. Its light is amplified with a TA. The molasses light is coupled to the fiber cluster and the optical pumping light is coupled to an independent fiber. A DFB and an ECDL laser are offset locked from the D2 and D1 master lasers respectively and combined sequentially in a TA together with EOMs and AOMs in order to produce the cooler and repumper for the MOT and molasses of ^{39}K. Its light is coupled into the fiber cluster.

We use two lasers to trap the atoms. A single mode YAG laser[3] (1064 nm) which is used to produce the red detuned optical dipole trap beams which are used in the evaporation process. And a single mode fiber amplifier laser[4] which is used to produce blue detuned optical potentials and was set up by P. Thomas [77]. A full description of the laser set-up can be found in the thesis of C. R. Cabrera [65].

The old version of the vacuum chamber set-up consisted mainly on two stainless steel chambers, see Fig. 1.1(a). A 2D MOT chamber and a chamber which is used as a 3D MOT and science chamber. The 2D MOT chamber was connected to the potassium ampoule sources and an ion pump[5] with an appropriate control of the temperature gradients in order to produce a potassium vapor pressure

[1] SYST DL PRO 780 - TOPTICA
[2] EYP-DFB-0767-00050-1500-TOC03-0005 - Eagleyard photonics
[3] Mephisto MOPA 25 W - Coherent
[4] ALS-GR-532-10-A-SP - ALS
[5] TiTanTM 25S Ion Pump - Gamma Vacuum

of $\sim 5 \times 10^{-8}$ mbar. This 2D MOT chamber is connected through a differential pumping tube to the 3D MOT/science chamber. This chamber has two re-entrant viewports with coated windows of 6 mm thickness and 50 mm clear aperture which are separated by 30 mm. This allow us to have currently a Numerical Apperture (NA) of 0.43. The pressure in this chamber was mantained around 10^{-11}mbar by two Non-Evaporable Getter (NEG) pumps[6]. The pressure of the science chamber was limited by the reading of our vacuum gauge[7] (10^{-11} mbar). A full description of the vacuum system can be found in the thesis of C. R. Cabrera [65].

The main ingredients for producing a degenerate quantum gas include MOTs, magnetic traps, optical traps and a magnetic field control for adjusting interactions. The experimental sequence to produce degenerate Bose-Bose mixtures, sketched in Fig. 1.1(b), is divided in different steps. In the following list, we describe them and show typical parameters which where used before the installation of the new 2D MOT and the high resolution objectives.

- We sequentially produce cold atomic beams of ^{41}K and ^{39}K in a 2D MOT. This is performed in a vacuum chamber with high vapor pressure of natural potassium.

- The atoms are sent from the 2D MOT chamber to the 3D-MOT/science chamber to load a dual species 3D MOT with $\sim 1.5 \times 10^9$ atoms of ^{41}K and 3×10^8 atoms of ^{39}K at a temperature ~ 1 mK. In order to increase the density, they are subsequently compressed in a hybrid D1-D2 compressed MOT reaching temperatures of ~ 70 μK.

- We perform simultaneously gray optical molasses on the D1-line for ^{39}K and ^{41}K to obtain efficient sub-Doppler cooling. We can achieve temperatures of $\sim 16\mu$K and 8×10^8 and 2×10^8 atoms of ^{41}K and ^{39}K, respectively.

- The atoms are prepared in $|F = 2, m_F = 2\rangle$ by optical pumping on the D1 line with almost 100% efficiency, capturing almost all the atoms in a magnetic quadrupole trap.

[6] NEXTorr D500 (500 l/s) and NEXTorr D200 (200 l/s) - SAES Getters
[7] UHV-24p extended range ion gauge, dual-thoria-iridium filaments (9715015)- Agilent

- Sympathetic cooling is performed in a compressed magnetic quadrupole trap by using radio-frequency (RF) evaporation on the hyperfine transition of ^{41}K, while ^{39}K is cooled by thermal contact. The rethermalization is very efficient due to the large ^{39}K - ^{41}K scattering length $a_{39-41} = 177a_0$. In this process we are able to increase the Phase Space Density (PSD) of ^{41}K and ^{39}K from 2×10^{-6} to 10^{-3} and from 10^{-7} to 2×10^{-4}, respectively. We obtained around 4×10^7 and 2.5×10^7 atoms of ^{41}K and ^{39}K at 30 μK. Instead, if we only cooled down ^{41}K we were able to obtain 6×10^7 atoms at 25 μK.

- A 15% of the atoms are transferred into a hybrid trap formed by the quadrupole magnetic trap and an optical dipole trap focused a waist below the magnetic field minimum, where they are evaporatively cooled from 9μK to $\sim 1\mu$K. Typically we end up with a total atom number of $\sim 2 \times 10^6$ atoms in total. Cooling both isotopes we reach similar temperatures with half of the atoms per isotope.

- Almost all the atoms are loaded into a crossed optical dipole trap where hyperfine and Zeeman transfers are performed to bring ^{39}K and ^{41}K to $|F = 1, m_F = -1\rangle$ and $|F = 2, m_F = -2\rangle$ respectively. There we perform evaporative cooling in the vicinity of a ^{39}K Feshbach resonance where $a_{39} = 150a_0$. Different resonances (33 G, 402 G) have been used, depending on the experiments. At low field, we use a magnetic field gradient in this process in order to distill ^{41}K from ^{39}K, being able to obtain different balances at will. This is possible because the states we use have magnetic susceptibilities of opposite sign.

- The largest ^{41}K and ^{39}K pure BECs which we have been able to produce had around 5×10^5 and 3.5×10^5 atoms. The dual condensation of both species lead to 1.5×10^5 atoms per species.

- In the end, the atomic clouds can be characterized either by absorption imaging in time of flight or by polarization phase contrast imaging *in situ*.

This sequence has been modified due to the upgrade of the 2D MOT and the installation of the two high resolution objectives. In section 1.5 we will detail

the modifications of the cooling sequence after introducing the 2D MOT upgrade and the installation of the objectives. In the following section we detail the implementation of a new 2D MOT.

1.3 2D MOT upgrade

The 2D MOT steel chamber that was installed initially presented several design and manufacturing problems which led to a large leak in one of the viewports after ten months of operation and to a continuous opening of micro-leaks on another viewport since August 2016. This steel chamber was substituted by a glass cell chamber on November 2017. With the new 2D MOT chamber we have been able to reach similar vapor pressures with smaller temperatures and we didn't have any leak since its installation. In section 1.3.1, we will introduce the problems of the first steel chamber 2D MOT. Then, in section 1.3.2, we will present the design of the new glass cell 2D MOT, explain its installation and show the results.

1.3.1 The leaky steel chamber

The steel 2D MOT chamber shown in Fig. 1.2(a) was a home-made design based on the design from ref. [78–80]. This vacuum chamber was thought to provide a large optical access in order to implement large elliptical beams to increase the atomic flux of the 2D MOT. Since the vacuum chamber geometry was rectangular, four custom made fused silica windows with Anti-Reflection (AR) coating[8] in both sides were used. These windows were sealed using indium wires[9]. Instead, the back vacuum window consisted of a CF40 view-port[10] made of a fused silica window which was brazed with Kovar[11] onto a 304 stainless steel flange.

The procedure to migrate the potassium from the source to the 2D MOT chamber was very complicated. To do so, the chamber was heated up to apply temperature gradients that brought the potassium into the 2D MOT. However, it was very hard to heat the 2D MOT chamber evenly and the potassium was

[8] AR 767 nm/0° - LaserOptik
[9] Indium wire 99.99% ⌀ 4mm (1N522407)-Advent research materials
[10] CF40 Fused Silica view-port 304L / Kovar - Trinos
[11] Kovar is a nickel-cobalt ferrous alloy that allows building glass-to-metal seals.

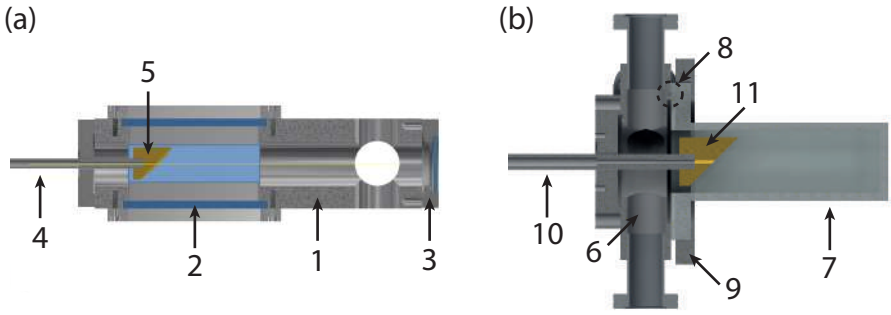

Figure 1.2: Comparison between steel and glass cell 2D MOT chambers. The scale of the images between the two chambers is set to 1:1.5. (a) Steel 2D MOT chamber. 1. The main body of the vacuum chamber is made of stainless steel. 2. Bottom indium-sealed rectangular fused silica view-port which leaked. 3. Back CF-sealed fused silica view-port with Kovar as a glass-to-metal transition. 4. Differential pumping tube. 5. Gold coated mirror to reflect the longitudinal molasses. (b) Glass cell 2D MOT. 6. The main body of the vacuum chamber is made of stainless steel. 7. Rectangular glass cell made of fused silica. 8. Groove of 69 mm ⌀ and 1 mm thickness to seal the glass cell (7) to the main body (8) using indium wire with 99.99% purity and 1.6 mm thickness. 9. Aluminum frame used to press the glass cell (7) against the main body (6). A thin aluminum foil frame is used to press the glass cell gently. 10 and 11. Differential pumping tube and gold-coated mirror which were already used in the steel 2D MOT chamber.

sticking onto the cold spots. In particular the potassium was concentrated on the vacuum view-ports and the ion pump.

Eventually, the high concentration of potassium on the ion pump presumably generated potassium filaments in between its high voltage plates, deteriorating it. Moreover, after ten months of operation, and just before I started my PhD, the back view-port started to leak. This view-port was replaced by a demountable conflat flange[12]. Although these view-ports normally use a Viton ring to do the glass to metal seal, the Viton ring was substituted by a 4 mm indium wire. This leak was due to the reaction between potassium and Kovar, which was accelerated due to the high concentration of potassium on the back view-port. Indeed, an analogous problem happened recently in the LENS experiment [81].

[12]VPCH42-Thorlabs

Therefore, we do not recommend to use view-ports that use Kovar as a glass-to-metal transition alloy to seal the vacuum windows in potassium experiments in chambers where the partial pressure of potassium is large.

After repairing the leak on the back view-port, the vacuum was maintained until August of 2016. A micro-leak appeared then on a corner of the bottom window. We were able to close this micro-leak by re-tightening the screws. However, this micro-leak continued to appear repeatedly for months and the re-tightening procedure was getting harder and harder every time. Indeed after replacing the chamber we realized that the teflon frame that we used to press the window gently (together with an aluminum frame) was completely deformed in a non-uniform manner. Our hypothesis is that the teflon was slowly deteriorating and eventually reducing the pressure over the window. Since the leak appeared in the bottom view-port, gravity didn't help us to keep the window sealed. Furthermore, it is more difficult to press evenly a rectangular window as compared to the circular ones. Indeed, the leak was located in a corner of the rectangular windows. After repeating the tightening process several times, the deformation of the teflon frame presumably became uneven and it didn't feel possible to close the leak forever.

Since the first micro-leak happened on the bottom view-port we started to design and prepare a new glass-cell 2D MOT chamber.

1.3.2 New glass cell 2D MOT

The glass cell 2D MOT that we use is sketched in Fig. 1.2(b). The main design of the new vacuum chamber was done by P. Cheiney. Its design was done taking into account the following key points:

- We used a quartz glass cell chamber in order to improve the vapor pressure on the 2D MOT. Quartz chambers have a better performence in comparison with stainless-steel because of two reasons. First, potassium sticks less into quartz and thus, we do not need very high temperatures on the chamber so that it does not stick into its surfaces. And second, quartz does not outgas as much as stainless steel and we do not need to continuously pump the 2D MOT chamber. Hence the lifetime of potassium in the chamber is

extended.

- We used a single circular indium wire in order to facilitate the sealing from the glass cell into the steel chamber. Thus, we avoided glass-to-metal transitions to prevent future leaks (such as the one of the back CF-seald view-port).
- We replaced the teflon by a thin aluminum foil frame in order to press the glass cell gently [82].
- We installed a copper feedthrough as a cold spot in order to simplify the potassium migration from the source to the glass cell.

The new vacuum chamber consists of a custom-made main body which is formed by solid stainless steel[13], see Fig. 1.2(b) and Fig. 1.3(a). As it can be seen in Fig. 1.4, it connects the main parts of the 2D MOT: the potassium sources, the ion pump[14], the glass cell[15] (see Fig. 1.3(b) and 1.3(c)) and the copper feedthrough used as cold spot (see Fig. 1.3(d)). The connection of the body to the potassium sources, ion pump and the cold spot is made through CF16 flanges using copper gaskets[16], silver coated screws and thread lubricant paste[17]. The glass cell is sealed with a single indium wire[18] of 1.6 mm ⌀ by pressing it with a stainless steel frame that we use together with thin aluminum foil, see Fig. 1.3(b) and 1.3(c). The sources and ion pump are separated by the main body of the 2D MOT by CF16 mechanical valves[19].

Cleaning procedure, installation and baking

Before assembling all the pieces and installing the new 2D MOT in the experiment we cleaned all the pieces except for the valves and glass cell. The cleaning

[13] 316L stainless steel electropolished on the inside - Vacom

[14] Ion pump 3 l/s 3SDI1D5KNN. Differential elements (50% Ti/50%Ta) are stable for noble gas loads - Gamma Vacuum. Digitel controller SPC1PS1E2ESNA - Gamma Vacuum. High voltage cable SCPSC35K - Gamma Vacuum

[15] 40 × 40 × 100 mm UVFS Cuvette with 5 mm wall attached to 76.2 mm outer ⌀ × 12.7 mm thick quartz flange. 5 outside surfaces of the cuvette AR coated for 767 nm.

[16] CF copper gasket, DN16, OFHC, OD 21.3mm, ID 16mm. CU16 - Vacom

[17] Molykote 1000 - Vacom

[18] Indium wire 99.99% ⌀ 1.6mm (IN5225)-Advent research materials

[19] 54124-GE02. Easy close all-metal angle valve DN 16 (5/8) flange: CF-R rotatable flange - VAT.

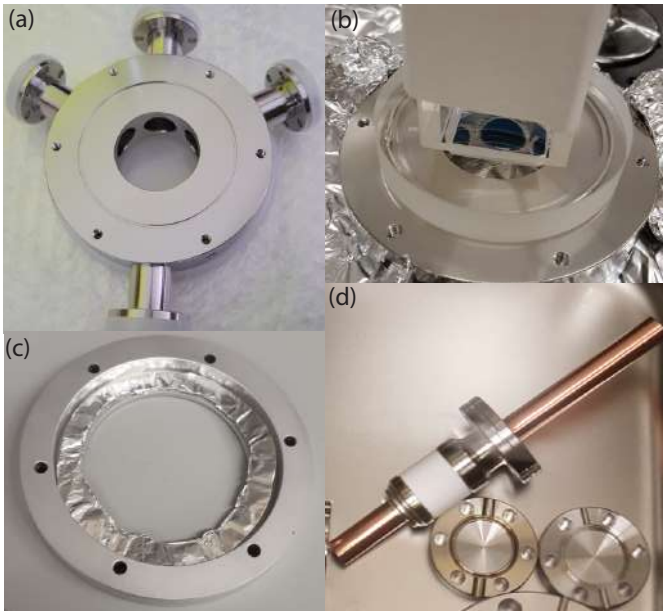

Figure 1.3: Details of the 2D MOT. (a) Main body of the new 2D MOT made of stainless steel. The top three CF16 flanges have been used (from left to right) to install cold finger made of copper, to install an ion pump, and to install a CF16 valve to be able to install a new source. The bottom CF16 flange has been used to install the current potassium source. As you can see there is a 1 mm width groove to be able to seel the glass cell with indium wire. (b) Sealing of the glass cell using indium wire. (c) A thin aluminum foil has been used together with a stainless steel frame to press the glass cell gently against the steel chamber. (d) Cold finger CF16 feedthrough made of copper.

procedure which we use consists on 3 steps:

- Cleaning with distilled water and soap[20] with a 5% concentration in an ultrasound bath at 50°C during 20 minutes.
- Cleaning with acetone[21] in an ultrasound bath at 50°C during 20 minutes.
- Cleaning with ethanol[22] in an ultrasound bath at 50°C during 20 minutes.

[20]Tickopur R 33 - Sigma Aldrich
[21]Acetone 99.8% - AC03102500 Scharlab
[22]Ethanol 99.9% - ET0002005P Scharlab

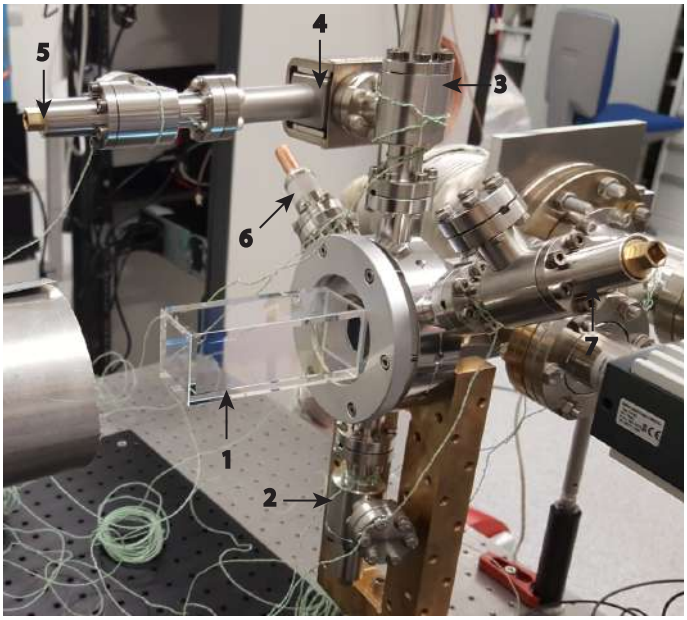

Figure 1.4: Starting the pre-baking of the glass cell. 1. Rectangular quartz glass cell. 2. CF16 valve which is used to connect the potassium source. 3. CF16 valve used to connect the (4) ion pump. 5. CF16 valve used to do a vacuum below 10^{-8}mbar (with a turbo-pump) in the ion pump before switching it on. 6. Cold finger CF16 feedthrough made of copper used to facilitate the migration of potassium from the source (connected through 2) to the glass cell (1). 7. CF16 valve which will be used to install an additional source.

After all the pieces were cleaned, we assembled them in order to pre-bake the chamber. In Fig. 1.4 we show the vacuum chamber assembled before realizing the pre-baking. In this process, we covered the glass-cell with a cylindrical aluminum foil of 1 mm thickness which was wrapped with oil-free thin aluminum foil in order to make a small oven to bake the glass cell. The rest of the chamber was covered with thin aluminum foil. To pre-bake the new 2D MOT we pumped the vacuum chamber with a turbo pump initially. When we reached a pressure below 10^{-8} mbar[23] we also switched on the ion pump. The hottest point during the baking

[23]The ion pump was opened for the first time inside a plastic bag which had been filled with Nitrogen.

procedure was kept below 110°C so that the indium wire did not soften. After the pre-baking process the pressure reading on the ion pump gauge read $< 10^{-10}$ mbar. The turbo-pump was disconnected and the 2D MOT chamber was kept under vacuum with the ion-pump on during a year before installing it on the experimental apparatus.

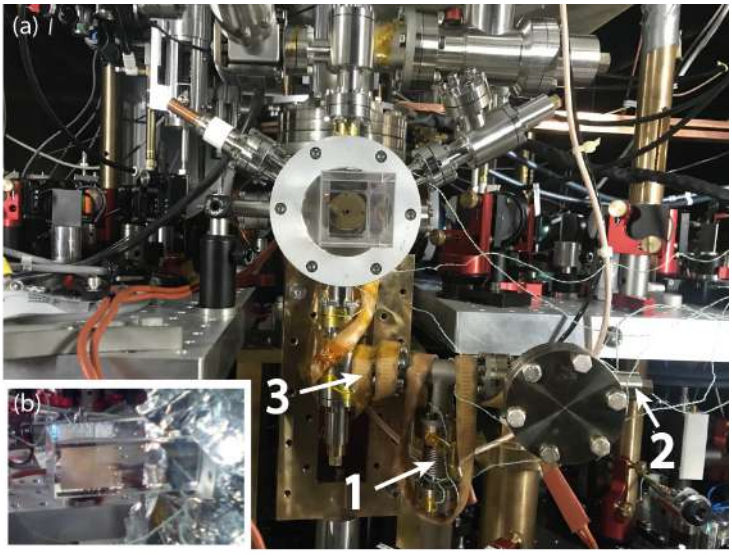

Figure 1.5: New 2D MOT vaccum chamber installed in the experiment. (a) 1. The source is connected to the bottom CF16 valve through a CF16 'T'. 2. A CF16 valve is used, together with a CF16 to CF40 flange adapter, in order to pump the vacuum chamber with a turbo pump. 3. Heating bads are used in order to heat up the source and the rest of the chamber. (b) The temperature gradients were such that the potassium tend to stick into back part of the glass cell.

One year afterwards, after the droplet experiments reported in chapters 3 and 4 were concluded, we decided to install the 2D MOT chamber in the experimental apparatus. Before removing the old 2D MOT we measured the absorption through the longitudinal axis using the molasses D2 cooler beam in order to target a similar potassium vapor pressure after installing the new 2D MOT. The absorption of the beam through the cell was 70%. Considering that the new

2D MOT is shorter[24] we should aim at having a 28% absorption to have similar vapor pressure.

During the upgrading process we installed the potassium source on the bottom part of the 2D MOT chamber, see Fig. 1.5(a). The potassium source is contained inside a glass ampoule[25] which is placed between two stainless steel cylinders inside a retractable below[26] which is used to crack the ampoule. The below is connected to the bottom valve by a CF Tee[27]. The Tee, below, blanks and stainless steel where cleaned and baked independently before the installation in a similar fashion as we described previously.

To install the new 2D MOT we closed the gate valve to the science chamber, and switched off the ion pump (labeled as 1 on Fig. 1.1(a)) and the ion pump of the NEG pump which is below the cross of the atomic shutter (labeled as 4 in Fig. 1.1(a)). The process of removing the old 2D MOT and installing the new one was performed while continuously flushing Nitrogen through the chamber with an over pressure. This was done in order to avoid any contamination from air to facilitate the pumping process. As soon as the new 2D MOT was installed we put it under vacuum using the turbo pumps initially, followed by the activation of the ion pumps as soon as the pressure was below 10^{-8} mbar. The cross of the atomic shutter and the 2D MOT where baked during few days. As done in the pre-baking stage, we kept the temperature close to the indium wire below 110°C. The small oven we made around the glass cell was also kept below 100°C to avoid damaging the coating. After the baking process, we activated the NEG pump, turned on its ion pump and cooled down the chamber. The pressure read by the ion and NEG pumps was 1.8×10^{-9}mbar and $< 10^{-10}$mbar respectively.

[24]Old 2D MOT. Back view-port to gold-coated mirror to bottom view-port: 215 mm + 28 mm. New 2D MOT. Back of glass cell to gold-coated mirror to bottom of glass cell: 84 mm + 15 mm

[25]Potassium, ingot, 99.95% metals basis. 244856-5G - Sigma-Aldrich

[26]CF hydroformed bellow, DN16, 1 flange rotatable, stainless steel 304/316L, length 80mm. V-FXB16R80-316 - Vacom.

[27]CF Tee, DN16, fixed, stainless steel 316L, bolt holes in line, length 76mm. TE16-316 - Vacom.

Potassium migration

After the baking process, we started the potassium migration from the source to the glass cell. The first time that the migration of potassium was done with the old 2D MOT we realized that the ion pump was also pumping the potassium, and eventually we pumped it all. For this reason, during the migration process we regulated the temperature gradients and the conductance between the ion pump and the glass cell in order to help the potassium migrate towards the glass cell without being completely sucked by the ion pump. After several days of adjustment of the gradient, the potassium arrived to the 2D MOT. In this process, we realized that the potassium was getting stuck on the back of the glass cell, as seen in Fig. 1.5(b). Since the glass cell was only heated through the thermal contact with the main body of the chamber, the back of the glass cell was cold and we couldn't regulate its temperature independently. We tried adjusting the temperature gradient and conductance of the ion pump and the valve from the source to the 2D MOT in order to maintain a good vapor pressure without having potassium stuck in the glass cell. However, this was not possible.

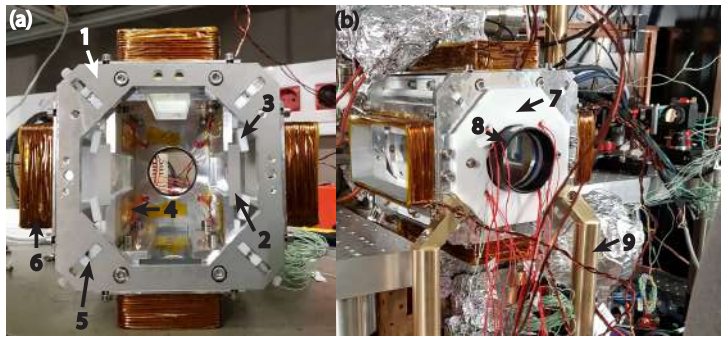

Figure 1.6: 2D MOT oven. (a) 1. Oven frame made of aluminum. 2. Windows from the old 2D MOT. 3. The windows are held against the aluminum frame (1) using a teflon piece, isolating the aluminum from the environment. 4. Thermoresistor bands are used to heat up the aluminum and make to make an oven for the glass cell. 5. A magnetic quadrupole for the 2D MOT is made with 4 permanent magnets. 6. To adjust the center of the magnetic quadrupole we use 4 coils to produce a bias field in the two transverse directions. (b) Oven installed. 7. Teflon cover to isolate the back part of the oven. 8. A 2″ N-BK7 window is used to close the oven from the back. 9 . Brass bars are used to held the oven.

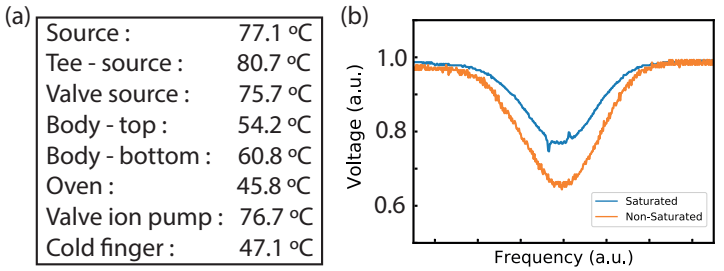

Figure 1.7: (a) Temperatures of the 2D MOT. (b) Absorption spectroscopy near the D2 transition. The blue and orange lines correspond to saturated and non-saturated spectroscopy. Both have been rescaled to its maximum value for comparison. The width of the absorption profile corresponds to the Doppler profile due to temperature broadening. The absorption is measured from the non-saturated spectroscopy.

For this reason, we installed an oven around the glass cell, see Fig. 1.6(a) and (b). The oven is composed by an aluminum frame which is heated up with thermoresistor bands[28]. It is held by two brass bars and its octogonal apperture (see Fig. 1.6(a)) fits on the main body of the 2D MOT chamber. Four side rectangular AR coated windows[29] and a circular back window[30] are used to provide optical access for the transversal 2D MOT beams, longitudinal molasses and push beams. The windows are held against the aluminum frame with teflon to thermally isolate the oven. The aluminum frame also holds four permanent magnets[31] and four coils which are used to produce and align the magnetic quadrupole which is necessary for the 2D MOT. Using this oven, we have been able to maintain a vapor pressure of potassium of $\sim 2 \times 10^{-7}$ mbar without having the potassium stuck on the glass cell. In the final configuration, the valve to the ion pump remains closed. The temperatures of the new 2D MOT on the current configuration are summarized in Fig. 1.7(a). The obtained Doppler profile can be observed in the absorption spectroscopy, see Fig. 1.7(b). In the final configuration we have a resonant absorption on the D2 of 35 %, and thus the vapor pressure should be similar to what we had before. Moreover, the oven is

[28] HT10K - Thorlabs
[29] Reused from the old 2D MOT
[30] WG12012-B - Thorlabs
[31] Rare earth magnet NdFeB - HKCM

only at 45.8°C, whereas for the old 2D MOT the main body was around 75°C.

In conclusion, we have been able to reach similar vapor pressure as we had with the old 2D MOT with lower temperatures. The design of this 2D MOT also allows for the addition of an extra source. In the future, we plan to install enriched potassium ^{40}K in order to produce degenerate Fermi gases. The loading parameters of the 2D MOT and 3D MOT will be summarized in section 1.5.

1.4 High resolution microscopes

Every experiment which we carry out ends up by imaging the atomic cloud so as to extract information from it. Therefore, mastering various imaging techniques is paramount to obtain the most insights in our experimental research. Two main techniques are used in cold atomic experiments. Time of flight imaging, which consists on releasing the atomic cloud from its trap in order to extract its momentum distribution after a long free fall, and *in situ* imaging, which consists on probing the cloud in the trap in order to probe its spatial distribution. Whereas typical sizes of the cloud after time of flight are on the order of $\sim 0.1 - 1$mm, *in situ* they are on the $\sim 1 - 10\mu$m order. Therefore, we need high numerical aperture microscopes in order to spatially resolve the atomic cloud *in situ*.

In the following section, we will describe the main experimental constraints for the design of a high numerical aperture objective which will allow us to image the atomic clouds with high resolution. Additionally, we have installed a second microscope to be able to generate highly resolved optical potentials on the atomic plane.

1.4.1 Experimental constraints

There are two main constrains that we should take into account to design the optical system to image the atoms: the physical constraints imposed by the choice of our science chamber and the pixel size of our camera.

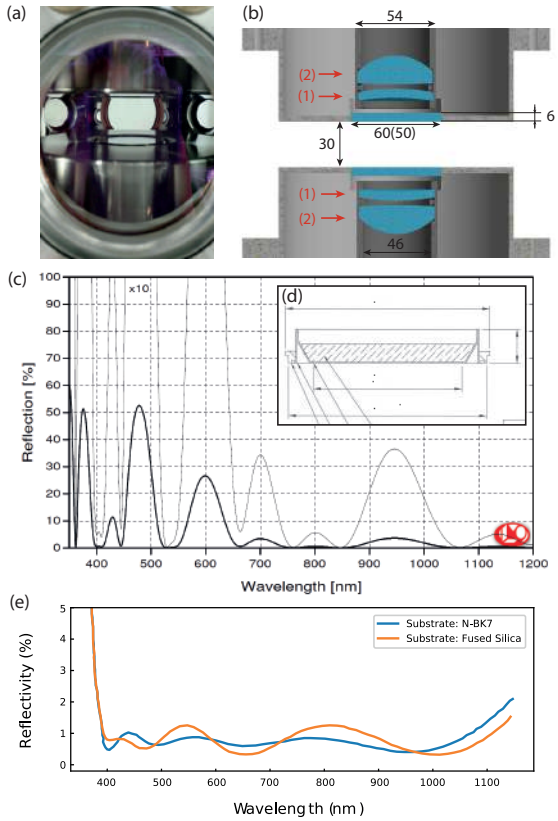

Figure 1.8: a) Side image of the science chamber showing the two re-entrant viewports. b) Schematic of the re-entrant view-ports including the imaging and addressing microscopes. All distances are in millimeters. The windows are made of synthetic fused silica and are AR coated for the cooling, trapping and imaging wavelengths. They are placed on a metallic frame and welded on the view-port. Although the metallic frame has an inner diameter of 60 mm the clear aperture is only 50 mm. The high resolution objectives are formed by a custom-made meniscus lens (1) and a high numerical aperture aspherical lens (2). The objective lenses are installed on a plastic tube and held by plastic rings in order to avoid the generation of Eddy currents when magnetic fields are switched on and off. (c) Reflectivity from the anti-reflection coating from the re-entrant view-ports vs. wavelength. (d) Detail of the vacuum window and its metallic frame. (e) Reflectivity from the anti-reflection coating from the asphere and meniscucs vs. wavelength for an average polarization.

For simplicity, our experiment was designed in order to have a single chamber as a 3D MOT and science chamber. Additionally, the laser cooling of potassium requires large beams in order to reduce the light assisted collisions in the 3D MOT [80, 83]. Thus, the optical access in our experimental apparatus cannot be directly compared to other experiments with independent 3D MOT and science chambers and other atomic species. Nevertheless, in order to have a large numerical aperture our science chamber has two re-entrant view-ports, see Fig. 1.8(a). The distance between both view-ports is 30 mm, the windows have a 6 mm thickness and a clear aperture of 50 mm, see Fig. 1.8(b). The windows are made of synthetic fused silica[32] and are AR coated for cooling, trapping and imaging lasers at 405, 532, 670, 767, 852, 1064 and 1178 nm at 0° of incidence [33], see Fig. 1.8(c). They are placed in a metallic frame which is welded on the view-port, see Fig. 1.8(d). Before the welding process the windows were specified to have a transmitted wave-front error (TWE) of $\lambda/10$.

The distance between view-ports, clear aperture and window thickness are the main constrains which limit the accessible numerical aperture. Therefore, the design of a $2''$ long working distance microscope is required in order to have a good resolution. Moreover, the window introduces aberrations on the wave-front of the light, which need to be appropriately corrected.

In our experiment, we have decided to image the atomic cloud *in situ* using a polarization phase contrast technique (see chapter 2). This technique requires the use of an Electron Multiplying Charged-Coupled Device camera (EMCCD), which amplifies the signal to noise ratio of the photogenerated electrons. This type of cameras use pixels with a large size. In particular, our camera has a pixel size of 16μm. Therefore, we must adjust the magnification of our imaging system accordingly. If the magnification is too small, the spatial resolution is limited by the pixel size. If the magnification is too large, the spatial resolution is limited by the diffraction limit of our optics at the expense of a smaller signal to noise ratio. In order to have a good compromise between the spatial resolution r_{DL} and signal to noise ratio, the magnification M of the optical system is normally

[32] Spectrosil 2000 synthetic fused silica, $\lambda/10$ TWE, 20/10 scratch/dig, 6 mm thickness - UKAEA

[33] Custom anti-reflection coating. B-11666 AR405+532+670+767+852+1064+1178nm/0° UHV - LaserOptik.

designed so that $M \times r_{\mathrm{DL}}$ is around 2 - 3 times the pixel size.

Before showing the design of the high resolution microscope, in the next section, we briefly review the concepts of spatial resolution, depth of focus and field of view.

1.4.2 Spatial resolution, depth of focus and field of view

The most common criterion to define the spatial resolution of an optical system is the minimum distance to distinguish two close by point sources. The imaging of a point source through an optical system is called the Point Spread Function (PSF). When the optical system is diffraction limited, the PSF is an Airy disk. To define the resolution of our optical system we will use the Rayleigh criterion. This criterion states that two point sources cannot longer be distinguished if the distance between the central maximum of both PSFs is closer than the distance between the central maximum and the first minimum of the Airy pattern. From this criterion we get that the resolution of a diffraction limited optical system r_{DL} is:

$$r_{\mathrm{DL}} = 0.61\frac{\lambda}{\mathrm{NA}}. \tag{1.4.1}$$

An optical system can only resolve the objects close to its optical axis and focal plane. The region along the optical axis in which the objects can be sharply imaged is called the Depth of Focus (DOF). In analogy to gaussian optics, the depth of focus in a diffraction limited system corresponds to the confocal parameter $\mathrm{DOF} = 2z_{\mathrm{R}}$, where $z_{\mathrm{R}} = \pi r_{\mathrm{DL}}^2/\lambda$ is the Rayleigh length. Thus, in the limits of the DOF, the spatial resolution of the imaging system is $\sqrt{2}r_{\mathrm{DL}}$. The Field of View (FOV) is the region on the object focal plane in which the objects can be sharply imaged.

Not all optical systems are diffraction limited. Besides the limitations imposed by the diffraction of light through an optical system, we also must take into account the imperfections of our optical system. If lenses are not perfect or they are misaligned, an optical system performance will not be limited by diffraction. The difference between the ideal propagation of a wave-front through an optical system and its real propagation is called the wave-front error. The

non-ideal propagation of light through an optical system results in optical aberrations. Indeed, the propagation of a spherical wave-front through a thick window introduces wave-front aberrations. For this reasons, we need to design an objective which corrects the aberrations introduced by the view-port and is diffraction limited.

In the following section we introduce the design of a diffraction limited high resolution objective.

1.4.3 Design

To implement a high resolution microscope in our experimental apparatus we need to address both the optical and mechanical design to adapt it to our experimental constraints. The optical design and initial mechanical prototypes of the objective were done by L. Saemisch [84]. The home made objective which we use has a NA = 0.43. Since the imaging transition is at $\lambda = 766.7$ nm, we expect to have a resolution $r_{\mathrm{DL}} = 1.1$ μm. During my master thesis, I measured the resolution of the imaging system in a replica set-up from the science chamber. The measurement consisted on determining the PSF of a gold dot of 250 nm, and we obtained a resolution of 1.5 μm [85].

At the beginning of my PhD, several challenges needed to be overcome in order to be able to install the imaging objective in the main experiment. First of all, the optical design of the full imaging system was not adapted for the pixel size of our EMCCD. Second, the design of the initial prototypes were not mechanically stable and thus we needed to ensure a submicron mechanical stability so that the resolution was not smeared out by vibrations. Indeed, we think that this was the limiting factor of the prototypes which were developed during my Master thesis. Moreover, since the MOT beams pass through the objectives, the MOT optics need to be adapted in order to have the MOT beams collimated in the science chamber. Initially, when we installed the imaging microscope this required the modification of the top MOT optics. Afterwards, we decided to install an addressing microscope to generate optical potentials in the atoms. Thus the optomechanical design of the imaging set-up and the MOT optics were adapted to install an addressing microscope below the science chamber.

Optical design of the home-made objective

The optical design of our home-made objective was made over the premise of simplicity and reduced cost. We decided to use only two lenses: a meniscus which corrects the spherical aberrations introduced by the window and an asphere which provides a high NA. The meniscus was designed with Zemax so that it would correct the spherical aberrations introduced by the window and together with the aspherical lens form a diffraction limited system. It was fabricated by Ross Optical Industries, is made of N-BK7 and has a custom-made broad band AR coating, see Fig. 1.8(e) . The asphere is a commercial asphere from Edmund Optics[34] which is made from L-BAL35. It has an Effective Focal Length (EFL) of ∼50 mm. A schematic of the objective can be seen in Fig. 1.8(b).

The optimization of the meniscus curvature, thickness and the distances between window and lenses was performed on Zemax by L. Saemisch assuming an exit pupil diameter of 46 mm. One of the criteria to determine whether an optical system is diffraction limited or not is to check whether the root mean square wave-front error (RMS-WE) is smaller than 0.07λ. Therefore, we have used the RMS-WE as a merit function to optimize the objective. Moreover, several tolerances were considered in the optimization process:

- Decentering of the window, meniscus and asphere by 0.2 mm.
- Tilt of the window, meniscus and asphere by 0.1°.
- 0.1% tolerance on the radii of the asphere.
- 0.25% tolerance on the radii of the meniscus.
- 0.1 mm tolerance on the thickness of the meniscus, asphere, window and distance in between.
- 0.3 mm tolerance on the distance between the vacuum window and the atoms.
- 0.0005 refraction index tolerance of the lenses.

[34] Aspheric lens, 50mm ⌀, 0.50 Numerical Aperture NIR Coated. Material L-BAL35. RMS surface flatness 0.75 μm. # 66-336 - Edmund Optics

In order to account for all the listed tolerances, we defined the distance between the meniscus and the window as a compensator with ±1mm. This does not mean that within 1 mm of tolerance the system will be diffraction limited, but that there should be at maximum ±1mm between the optimal distance and all the configurations required to have a diffraction limited microscope in the presence of imperfections within the listed tolerances.

The optimum configuration of the overall set-up is sketched in Fig. 1.9, where we obtain a $\mathrm{RMS}-\mathrm{WE}=0.028\lambda$. The Working Distance (WD) of the objective is 32.2 mm, the effective focal length of the system is 48.7 mm and the Back Focal Length (BFL) is 33 mm. The numerical aperture of the system is 0.43, the resolution is 1.1 μm and the depth of focus is around 10 μm. Moreover we have computed the FOV of the system by finding the object height at which the RMS-WE is 0.07λ. We found that the FOV comprises a circle of $\varnothing = 330\mu m$.

The tolerance of the optimal set-up has been computed by calculating the imperfections which lead the system to an $\mathrm{RMS}-\mathrm{WE}=0.07\lambda$ within the compensator limits. We obtain that the tolerance on the tilt between the lenses and the tilt of the whole objective are 0.3° and 0.07° respectively. The tolerance on the decentering between the lenses is 165 μm. The tolerance on the distance between lenses is 130 μm. The distance between the atoms and the window can always be compensated within the mechanical constraints of the system.

The performance of the objective at different wavelengths can be different due to the chromatic dependence of the index of refraction. Since the design of the objective was not optimized for different wavelengths the chromatic shifts at 532nm and 1064nm are -685μm and 415μm respectively. These shifts are far greater than the DOF, and thus the objective is not achromatic. Provided that the complexity of designing an achromatic objective is far greater and the group didn't have any expertise on high resolution imaging, we decided to deal with the chromatic shifts in order to simplify its complexity.

The imaging set-up: optical design

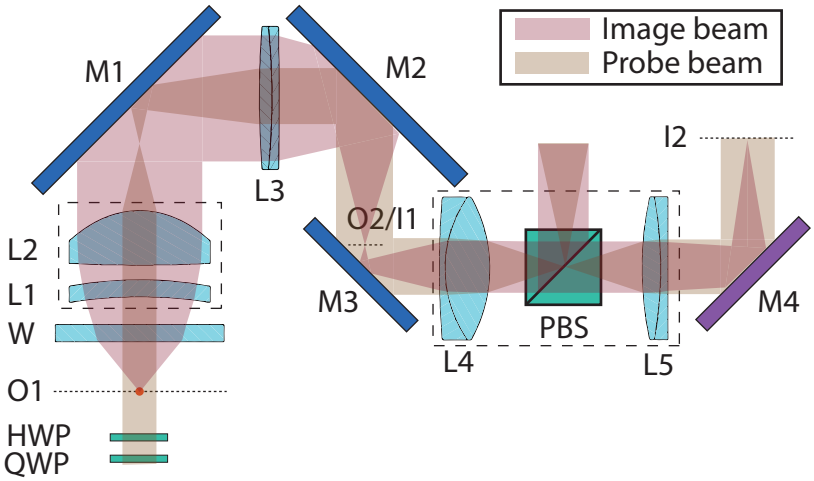

Figure 1.9: Scheme of the imaging set-up. Not to scale. (QWP) Zero order quarter and half waveplates (HWP) 768.4 nm. (O1) Object/Atomic plane. (W) Vacuum view-port. (L1) Meniscus. (L2) Aspheric lens. (L1+L2) form the microscope, have an EFL=48.7 mm and a BFL = 33 mm. They are centered together in a plastic tube and separated by a plastic spacer. (M1) 3″ dielectric mirror with NIR broad-band coating. (L3) Achromat EFL = 500 mm. (M3 and M4) 3″ and 2″ dielectric mirror with NIR broad-band coating. (L1+L2+L3) First telescope with a magnification $\sim$ 10.3. (O2/I1) Intermediate image plane which works as a second object plane in the full set-up. (L4) Achromat EFL = 80 mm. (PBS) 25 mm×25 mm×25 mm Polarization Beam Splitter. (L5) Achromat EFL = 250 mm. (L4+L5) Second telescope projecting and image from O2 into the image plane I2. Magnification of $\sim$ 3.1 (M4) Long pass dichroic mirror to remove Z beam . Distances between closest surface on the optical axis and thickness of optical elements: (O1-W) 15.478 mm, (W) 6mm, (W-L1) 10.476 mm, (L1) 6.045 mm, (L1-L2) 3.107 mm, (L2) 19.4 mm, (L2-L3) 547.737 mm, (L3) 4.5 mm + 2.6 mm, (L3-L4) 566.266 mm, (L4) 2 mm + 16 mm, (L4-L5) 327.692 mm, (L5) 6.6 mm + 2.6 mm, (L5 - I2) 243.155 mm.

The construction of the imaging set-up requires the inclusion of extra lenses in order to adapt the magnification of the optical system to match the pixel size of the camera. Since the EFL = 48.7 mm, we need a magnification between 32 and 48 so that $M \times r_{\mathrm{DL}}$ is between 2 - 3 times the pixel size. If we used a single lens we would need a lens with a focal length $\sim$ 2m. In general there are not commercial lenses with 2m focal length and we would need to ask for a custom-made lens. Thus we have decided to make an optical set-up formed by two telescopes. Moreover, since the BFL of the objective is 33 mm a collimated beam passing through the objective focuses inside the re-entrant viewport. Being able to access the back focal plane of the objective would be very useful, since it coincides with the Fourier plane and we could perform scalar phase contrast imaging. Having a two telescope set-up allows us to have an extra Fourier plane in which the imaging beam would be focused and accessible. Therefore, this set-up is flexible so that we could implement a scalar phase contrast technique by using a phase plate on such spot.

Initially, we used an optical set-up formed by the microscope and three 2″ achromats [35] with an effective focal length of 750 mm, 80 mm and 250 mm respectively. The set-up was very similar to the one sketched on Fig. 1.9. Due to space constraints, the distance between the objective and the lens sketched as L3 in Fig. 1.9, and the L4 and L5 lenses was smaller than the sum of their back focal lengths. This set-up was used to perform the experiments described in chapters 3 and 4. Later on, we modified the imaging set-up to get a smaller magnification and set the right distances so that the imaging beam was recollimated on the camera. We used an achromat with 500 mm[36] instead of the 750 mm focal length. Fig. 1.9 describes the set-up as it is used currently, which was used to perform the experiments described in chapter 5.

Whereas the initial set-up had a FOV of 240 μm, the current design has a FOV of 310μm. Since the EMCCD chip has 512 $\times$ 512 pixels, the image of the chip on the object plane (255μm $\times$ 255μm) is a bit smaller than the transverse FOV.

The tolerances of the full set-up have also been analyzed with Zemax. Very

[35] AC508-750-B, AC508-80-B and AC508-250-B - Thorlabs
[36] AC508-500-B - Thorlabs

similar tolerances have been found for the tilt and decentering of the objective lenses. Moreover, the most stringent tolerances are the tilt of the objective with respect to the vacuum window (0.3°) and the decentering between the objective and the next lenses (36μm). The tolerance on the decentering and tilt between the rest of the lenses are not so difficult to achieve. Whereas the DOF on the object plane is $\sim 10\mu$m, after the first telescope there is an intermediate image with a DOF of $\sim 800\mu$m. The image of the atomic cloud after the second telescope is focused on the camera with a DOF of 8mm.

Since the optical path is really long, we have used mirrors in between the lenses, see Fig. 1.9. The mirrors which we use are fused silica broadband dielectric mirrors[37] with an optical flatness of $\lambda/10$, except for the last one before the camera. This one is a long pass dichroic mirror which is used to remove the Z trapping beam (1064 nm) and has a specified optical flatness of $\lambda/4$ (at 633 nm)[38], although we have measured that its performance is considerably worse, see section 1.4.4. All the mirrors are glued into the mirror-mounts to avoid any mechanical stress which could bend the mirrors and introduce aberrations.

As we will describe in chapter 2, we use a polarization phase contrast imaging in order to image the atoms. To do that we adjust the polarization angle of a linearly polarized probe beam with a true zero order $\lambda/2$ waveplate[39] and analyze the polarization rotation with a Polarization Beam Splitter[40] (PBS), see Fig. 1.9. Moreover, we include a true zero order $\lambda/4$ waveplate[41] to compensate the difference in phase shift between the s and p polarizations introduced by the dielectric mirrors at 45° and generate a purely linearly polarized beam.

In the next section, we introduce the mechanical design to install the lenses in the experimental apparatus.

The imaging set-up: mechanical design

The mechanical design of the optical set-up is split in two parts. The high resolution objective and the achromatic lenses.

[37] BB3-E03 and BB2-E03 - Thorlabs
[38] DMLP900 $\varnothing = 2''$ - Thorlabs
[39] True Zero Order Half Waveplate 768.4 nm, WPF0388 - FOCtek.
[40] Thin Film Polarizer G33572900, Extinction ratio 10000:1
[41] True Zero Order Quarter Waveplate 768.5 nm, WPF212Q - FOCtek

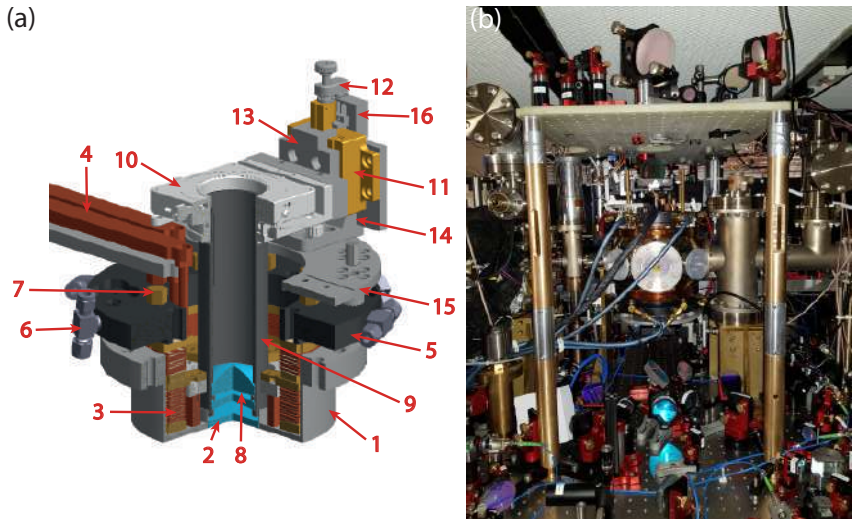

Figure 1.10: (a) Microscope set-up 3D section. (1) Re-entrant view-port. (2) Vacuum window. (3) Main coils of the experiment. (4) Copper bars bringing current to the coils. (5) Water distribution piece to cool down the coils. (6) Water distribution connectors. (7). Nut for sealing the water distribution. (8) Lenses of the objective. (9) Plastic tube where lenses are placed together with plastic spacers and holders. (10) 5 - axis stage. (11) Linear stage. (12) Linear-piezo nanopositioner. (13) Aluminum piece to connect 5 - axis and linear stages. (14) Aluminum piece which holds the objective mount on tope of a pacman-shaped aluminum breadboard (15). (16) Mechanical stop to avoid that the objective crashes on the view-port by accident. (b) Full set-up including imaging and addressing microscopes. The top breadboard is used to install the telescope lenses of the imaging set-up. Its held by four long demountable bars. The optics of the addressing set-up are installed on the optical table.

The high resolution objective design is constrained by the re-entrant view-port and the main coils of the experiment, see Fig. 1.10(a). The lenses are installed on a plastic tube and are separated and held by plastic rings. The objective tube is hold by a 5-axis stage[42] that we only use to adjust the centering and tilt of the

[42]LP-2A : Newport

lenses. This stage works together with a linear stage that we control with a linear-piezo nanopositioner[43] to adjust the focusing of the objective. The two stages are held by aluminum pieces which lie on top of a custom pacman-shaped aluminum breadboard. This breadboard lies on top of the water distribution piece which is used to cool the main coils of the experiment. The water distribution and the coils are held on top of the re-entrant viewport. With this set-up we avoid having independent mechanical vibrations between the objective and the science chamber.

The rest of the achromatic lenses which form the imaging set-up are installed in a fiber-glass reinforced plastic breadboard[44] which is on top of the science chamber and is used to avoid Eddy currents, see Fig. 1.10(b). The mirrors that we use on the top breadboard are either installed on mirror mounts from Newport[45] or Radiant-Dyes. The achromat with EFL = 500 mm is installed on a 2″ Thorlabs tube which is glued on a mirror mount from Radiant-Dyes in order to be able to adjust the angle. The second telescope is installed in a Thorlabs 2″ tube which centers the optical axis between the EFL = 80 mm and EFL = 250 mm achromats. The tube is mounted on a translational stage[46], and we use a micrometer screw in order to adjust the focusing between the EFL = 500 mm and EFL = 80 mm lenses. The EMCCD camera is installed over an aluminum support. Since the depth of focus on the image plane is on the order of 1 cm we do not use any translational stage to focus the camera.

The addressing set-up

Since the opto-mechanical design of the addressing set-up is very similar to the imaging set-up, we will focus on the main differences.

The optical design of the addressing set-up is sketched in Fig. 1.11. Basically it uses an objective like the one which is used for the imaging set-up. We mix the light to generate the potentials and the probe beam on a wedged window[47]

[43] N-470 PiezoMike Linear Actuator : PI

[44] Base material: glass cloth. Matrix resin: Epoxy (epoxide). 450 mm × 750 mm × 12.7 mm, EP GC 201 - Hippe

[45] Mirror Mount, ULTIMA, Clear Edge, 3.0 in., 3 Locking Knobs. U300-A3K : Newport

[46] Manual Linear Stage, Quick-Mount, 13 mm Travel, M6 Thread. M-460A-X + Vernier Micrometer, 13 mm Travel. SM-13 - Newport.

[47] WW42012 - ⌀2″ UVFS Wedged Window, Uncoated : Thorlabs

that we use as beam sampler. The Z dipole trap, the addressing beam and the probe beam are combined in a dichroic mirror[48]. The rest of the mirrors which are used in the set-up are dielectric mirrors with a broad band coating which allows to reflect wavelengths between 750 nm and 1100 nm[49]. Since the probe beam and the Z optical dipole traps go through the objective we have modified both set-ups so that they are collimated and focused on the atoms respectively.

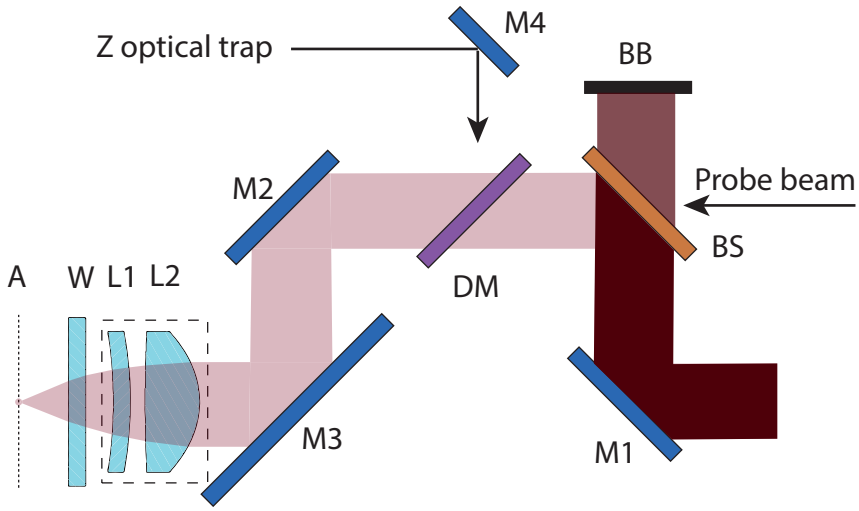

Figure 1.11: (A) Atomic plane. (W) Vacuum window. (L1) Meniscus lens. (L2) Aspheric lens. (M1, M2, M3 and M4) are dielectric broad band coating mirrors. (DM) Short pass dichroic mirror. (BS) Beam sampler. It is used to mix the addressing and probe beams. (BB) Beam block. The Z optical trap beam is combined on the dichroic mirror (DM) with the addressing and probe beams.

During my PhD I have participated in the supervision of a project to generate arbitrary potentials on the atoms using a digital micro-mirror device (DMD) [86]. Since the implementation of the DMD on the main experiment has not been performed yet, the description of the full set-up including the DMD will be explained in the thesis of future PhD students from the group.

The mechanical design of the addressing set-up is analogous to the one used

[48] DMSP900L - ⌀2″ Shortpass Dichroic Mirror, 900 nm Cutoff
[49] E03 coating from dielectric Thorlabs mirrors

for the imaging set-up. The only difference is the orientation of the objective mounts due to the top-bottom asymmetry of the copper bars which bring the current to the main coils of the experiment. Since the addressing objective is upside down, both the 5-axis stage and the linear stage are reversed so that the movable parts rest on the respective micrometric and nanopositioner screws. In this case, the linear stage has been replaced by another model for convenience[50].

In the following section, we detail the implementation of the imaging and addressing set-ups on the experimental apparatus.

1.4.4 Implementation

The installation of the imaging and addressing set-ups on the main experiment was performed in two stages.

In a first stage, we installed the imaging set-up using an achromat of EFL = 750 mm instead of 500 mm (lens L3 in Fig. 1.9). As explained before, the distance between the lenses was such that the probe beam was not collimated in the imaging plane. Moreover, in the installation process we took as a reference beam which was perpendicular to the top vacuum-window and was centered on the center of the magnetic quadrupole. Using this procedure we were not able to perfectly align the optical axis of the imaging set-up with the reference beam and ended up moving the last mirror before the camera to be able to image the atomic cloud. Thus, the imaging was presumably not centered on the field of view of the objective.

In a second stage, we modified the imaging set-up in order to improve it and understand its limitations. First of all, we removed the top objective, characterized the aberrations introduced by our vacuum view-ports and discovered that they introduce large astigmatism, trefoil and spherical aberrations. Afterwards, we installed two high NA objectives. The imaging one on top and a second objective on the bottom of the science chamber in order to be able to address the atoms with highly resolved optical potentials. Since the installation procedure of the first and second stages was very similar, we will only describe the installation on the second stage. Finally, we characterized the resolution after the second stage

[50] M-423 : Newport

of installation, corrected the astigmatism introduced by our vacuum view-ports and improves the performance of the complete high resolution optical set-up.

In the following section, we describe how do we characterize the imaging resolution of the imaging objective after the first installation stage.

First stage: characterization of the imaging resolution

To characterize the resolution of the imaging set-up we should measure its PSF. Ideally, we would trap a single atom on the center of the chamber and measure its fluorescence. However, it is not a trivial task to trap and image a single atom and generate a good point source inside the vacuum chamber. Instead, we measured the size of a bright soliton which has the size of the harmonic oscillator length of the trap $a_{\mathrm{ho}} = (\hbar/m\omega)^{1/2}$, where $\hbar$ is the reduced Planck constant, m is the mass of ^{39}K and ω is the trapping frequency. In our experiment, typically $a_{\mathrm{ho}} \sim 1.6$ μm and thus it is not a good point source. Taking as a reference the 1.5μm resolution which was measured in the re-entrant view-port replica set-up, we should observe an Airy disk with the first order minimum at ~ 2.2 μm from its center. After the first installation stage, we measured a distance of 2.9(1) μm, see Fig. 1.12(a), which indicates that the performance of the imaging set-up is worse than what we measured on the replica set-up and that the resolution is not better than 2.9(1) μm.

To determine the size of the bright soliton we performed independent measurements of the magnification of the imaging system. The magnification was calibrated by using Kapitza-Dirac diffraction of a BEC [87]. We imprint shortly a periodic modulation of the phase on a BEC (using a red detuned lattice) in order to generate diffraction. In this procedure, we keep the BEC in an optical waveguide so that the diffracted peaks propagate along the object plane. As it is shown in Fig. 1.12(b), side peaks with momentum $p = 2h/\lambda$ appear, where h is the constant of Planck constant. By comparing the expected distance between the central and side peaks on the object plane with the observed distances on the camera we can extract the magnification of the imaging system.

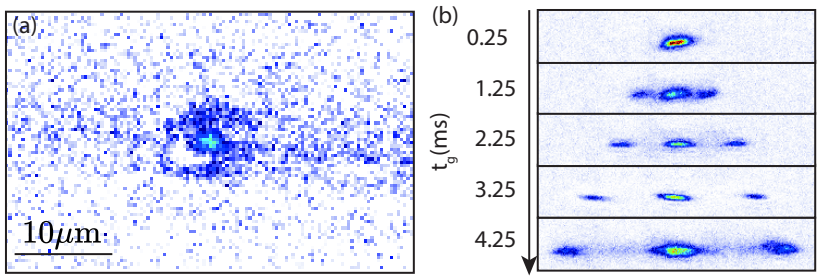

Figure 1.12: (a) *In situ* image of a bright soliton which was used to estimate the resolution after the first installation of the imaging set-up. As it can be seen there is not a ring but side lobes along the vertical direction. This indicates the presence of astigmatism. (b) *In situ* images of Kapitza-Dirac diffraction on a BEC vs. guide time on an optical waveguide. The magnification of the initial and new set-ups is 49.6(9) and 33.1(6), respectively. The images on (a) and (b) were taken with the polarization phase contrast technique which is explained in chapter 2.

In the next section, we show the observations of the aberrations introduced by the vacuum windows.

Second stage: aberrations introduced by the vacuum view-ports

In order to characterize the aberrations introduced by our vacuum view-ports we removed the imaging system which was installed in the first stage. To measure the aberrations introduced by the view-port we used a Twymann-Green interferometer. We use a standard non-polarizing beam splitter[51] with a reference arm and a path which was crossing the two vacuum windows twice, see Fig. 1.13(a). The mirrors which we use are 2″ broadband dielectric mirrors[52]. We used a gaussian beam of a 34 mm waist to crosscheck the biggest possible area of the windows. The interference is measured on a CCD camera by a lens with 300 mm effective focal length.

[51] 50/50 Non-Polarizing Cube Beamsplitter (700 - 1100 nm). Surface flatness $\lambda/4$ and wavefront error λ (at 633 nm). BS032 - Thorlabs)

[52] ⌀2″ Broadband Dielectric Mirror, 750 - 1100 nm. Optical flatness $\lambda/10$ (at 633 nm) - Thorlabs

Initially, we tested the interferometer without the vacuum chamber to cross-check that the elements of the interferometer itself where performing appropriately. In Fig. 1.13(b) we observe the interference without the vacuum chamber. The shape of the beam does not show any appreciable aberrations. Afterwards, we measured the aberrations introduced by the vacuum view-ports, as sketched in Fig. 1.13(a). We observe that the shape of the interference pattern is slightly modified and its elliptical shape might correspond to astigmatism introduced by the vacuum view-ports. Moreover we tested dichroic mirrors in an independent interferometer. Whereas the dielectric mirrors do not introduce any aberrations (see Fig. 1.13(b)), we have observed that the dichroic mirrors in reflection at 45° do introduce large astigmatism, see Fig. 1.13(d). For this reason, as depicted in Fig. 1.11, we have used a dichroic in transmission in the addressing set-up in order to mix the Z dipole trap with the probe and addressing beams.

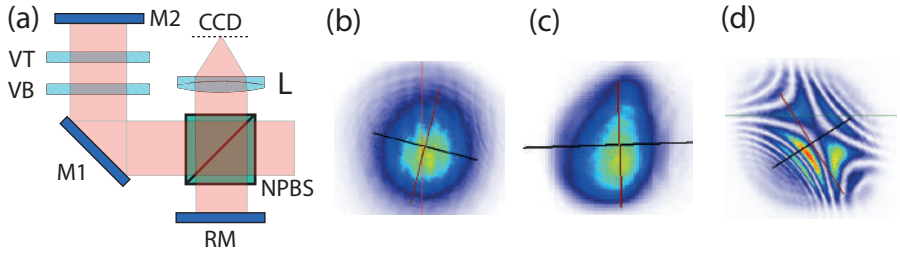

Figure 1.13: (a) Scheme of the Twymann-Green interferometer. (RM) Reference 2″ dielectric mirror. (M1 and M2) 2″ dielectric mirror. (VB and VB) Top and bottom vacuum view-ports. (NPBS) Non-polarizing beam splitter 2″. (L) Achromatic lens EFL = 300 mm ⌀ = 2″ (d) Wave-front error tested without the viewports (VT and VB). (c) Wave-front error measured by the set-up described in (a) including the vacuum view-ports. The ellipticity shows astigmatism. (b) Wave-front error tested without the viewports (VT and VB) and replacing the (M1) mirror by a dichroic. It shows a severe astigmatism of several λ.

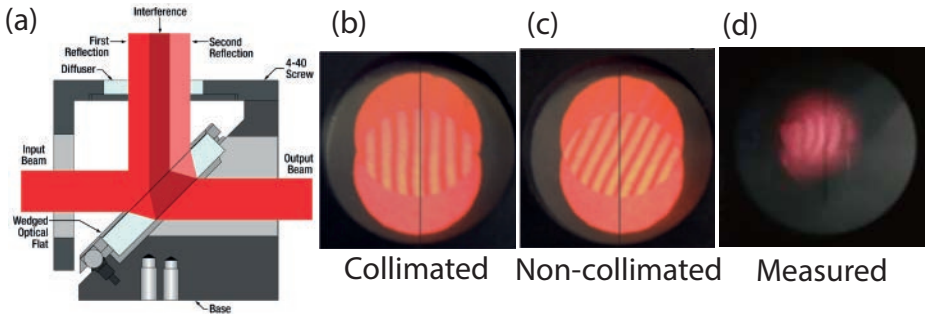

Figure 1.14: (a) Schematic of shearing plate taken from Thorlabs webpage. (b) Collimated and (c) non-collimated interference patterns taken from Thorlabs webpage. (d) Interference pattern formed after collimating a 34 mm beam which crosses through the vacuum windows of the science chamber. A small curvature of the fringes can be appreciated, showing additional aberrations apart from the observed astigmatism.

Additionally, we performed tests with a shearing plate interferometer[53] which also helped us to adjust the collimation of the 34 mm beam. The shearing plate is formed by a window which is optically very flat, see Fig. 1.14(a). It produces an interference between the reflection of the beam on its front and back faces. When the beam is collimated the interference fringes are parallel to the direction of propagation of the beam, see Fig. 1.14(b). Instead if the beam is defocused the fringes are tilted, see Fig. 1.14(c). We crosschecked how the collimation of the 34 mm beam is modified when it crosses the vacuum windows. Indeed, we realized that if we collimate the beam before the chamber it is slightly defocused after crossing the vacuum view-ports. This means that the optical flatness of the vacuum windows is no longer $\lambda/10$. This effect must be due to the pressure difference, which makes the windows work as a bi-concave lens. By re-collimating the beam after the vacuum chamber and crosschecking the interference with the shearing plate in two orthogonal directions, we realized that the divergence of the beam on the two axis is not symmetric. Hence, the windows also introduce astigmatism on the beam. Moreover, we observe that the

[53] SI500 - Shearing Interferometer : Thorlabs

fringes of the pattern of the shearing plate are slightly curved and thus we must have additional aberrations, see Fig. 1.14(d).

Second stage: Installation of imaging and addressing objectives

To install the high resolution objectives we adopted a different strategy. Instead of aligning the reference beam to the center of the magnetic quadrupole, we aligned the reference beam to the center of the vacuum window and then shifted the magnetic quadrupole to be on the field of view of the objectives.

Figure 1.15: Interference pattern formed from the reflection of the top reference beam on the imaging objective. Below the biggest patterns, on the left, we can observe the reflection from the bottom viewport. On top of this reflection and also below we can observe the same interference pattern repeated. This secondary reflections come from the back reflection of the wedged window that we use in the addressing set-up.

In the aligning procedure, we realized that the vacuum windows are not parallel between each other, there is an angle of 0.2° between them, see Fig. 1.15. This angle is not negligible since the tolerance alignment of the objective with respect to the window is 0.07°. Therefore, we used two reference beams: one for the top and one for the bottom window. We crosschecked in Zemax that the best strategy to have a diffraction limited optical system which comprises both objectives is to align each objective to its own window.

Thus each reference beam is perpendicular and centered to the respective window. To align the reference beams we used pinholes centered on the view-

ports and coupled the reflections from the vacuum windows back into the fiber.

We installed the top objective and aligned it roughly with the help of a pinhole and a mirror which we installed on top of the 5 axis stage to align the center and angle of the objective. Afterwards we fine tuned the center and tilt of the objective by checking the reflections of the top reference beam on the surfaces of the objective around 1 m far. The centering and tilts of the 5 axis stage can be adjusted until all the reflections from the different surfaces overlap. In Fig. 1.15, we show an image of the interference pattern which is observed when the objective is aligned. An analogous alignment procedure was performed for the bottom objective. In this case, the fine tune alignment of the reflections was more complicated since the reference beam reflected by the first optical surface of the objective diverges faster and the reflections needed to be crosschecked closer to the science chamber.

The achromatic lens with EFL = 500 mm was roughly aligned by hand, with the help of a pinhole and a mirror which were temporarily assembled on the lens tube so that the top reference beam crossed the lens through its optical axis. The fine tuning alignment was performed with the help of the mirror mount to adjust its angle so that its own optical axis coincides with the one of the objective. The telescope formed by the EFL = 80 mm and 250 mm lenses was aligned by using an additional reference beam which we installed on the top breadboard. This additional reference beam was aligned so that it crossed the EFL = 500 mm lens through its optical axis. The alignment of the telescope was performed roughly with the help of a pinhole and a mirror which was placed together with the telescope. The fine tuning alignment of the telescope was performed with the help of the previous 2 mirrors (labeled as M2 and M3 in Fig. 1.9) by overlapping the reflections from the lenses.

An additional long pass dichroic mirror[54] was used to remove the Z dipole trap beam and align the top reference beam on the center of the camera chip. Ideally, we would remove the Z dipole trap using a narrow bandpass filter in transmission. We could put it either in between the objective and first achromat or in between the second telescope so as to avoid the introduction of aberrations. In between the objective and first achromat we would need a 3″ filter and in

[54]DMLP900L : Thorlabs

between the second telescope we would need a custom mount to adjust the angle of a 1″ filter. For this reason, we decided to remove the Z dipole trap using a dichroic as a last mirror so that we can replace it easily in the future.

To adjust the focusing between the lenses, we decided to fix the position of the top objective with the planned distances to the vacuum window. The bottom objective was adjusted, with the help of the shearing plate, so that a collimated beam passing through both objectives is collimated at the output. We found the focus of the first achromat by focusing a collimated reference beam from the top breadboard. We placed a camera in the focusing spot which corresponds to the intermediate image (referenced as I1 in Fig. 1.9).

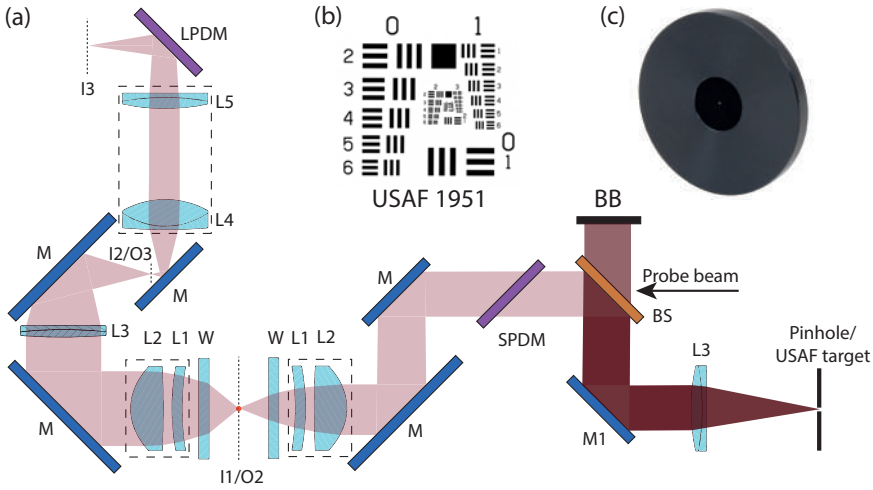

Figure 1.16: (a) Schematic of the optical set-up used for characterization with the USAF 1951 target (b) and a pinhole (c). All the optical elements in this set-up correspond to the elements described in Fig.1.9 and 1.11. Additionally we use an achromatic lens with an EFL of 400 mm to image either the USAF target or a 1μm$\varnothing$ pinhole in the atomic plane. (O1) USAF target/pinhole in the object plane. (I2/O1) Image on the atomic plane. It is also the object plane of the imaging set-up. (I2/O3) Intermediate image of the imaging set-up. (I3) Image on the EMCCD camera.

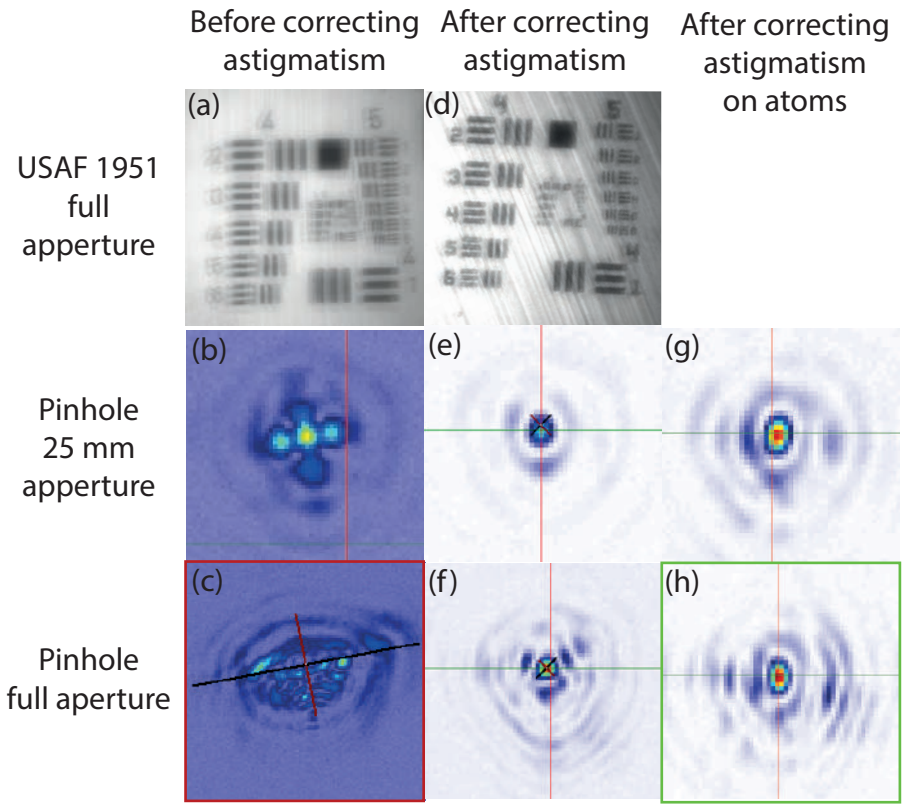

Figure 1.17: All the images in this figure are taken on the intermediate image camera. The images on the first column (a),(b) and (c) correspond to images of the USAF 1951 target (full aperture) and the pinhole (for 25 mm and full apperture) before the correction of astigmatism. The images on the second column (d),(e) and (f) correspond to images of the USAF 1951 target (full aperture) and the pinhole (for 25 mm and full apperture) after the correction of astigmatism. The images on the third column (g),(e) correspond to images of the pinhole (for 25 mm and full apperture) after the correction of astigmatism by correcting the images of bright solitons imaged on the EMCCD. All the images have been taken in its optimal configuration at each stage except for figure (c), which is an exemplary figure of the first images of the pinhole. In this case, the image was also taken with a slight defocus.

Second stage: Characterization of imaging and addressing objectives

To characterize the imaging set-up we performed several tests. First of all, we produced an image of a USAF 1951 target[55] on the atomic plane using an achromat with an EFL = 400 mm together with the addressing objective. We imaged it with the imaging set-up. The set-up which we used is shown in Fig. 1.16(a) and the ideal USAF 1951 target is shown in Fig. 1.16(b). The initial characterization was performed in the intermediate image. Using this set-up we measured the size of the square of the element 2 from group 2 to be 698 μm on the intermediate image. The real size of this element is 556.8 μm. Therefore the magnification of the complete system is 1.25. Given that we are using an EFL 400/50/50/500 mm lens system we also expect a magnification of 1.25. Therefore, we have assumed that the magnification of the addressing and imaging set-ups is 8 and 10 respectively. The smallest elements we were able to discern are the element 6 from group 5, see Fig. 1.17(a). These elements have a spacing of 8.77 μm which means that we are able to see elements of 1.09 μm spacing. This gives us an indication of the resolution of the imaging system but it does not mean that the resolution of the imaging system is 1.09 μm.

Moreover we performed an additional test with a 1 μm pinhole[56] and image it with the addressing set-up on the atomic plane, see Fig. 1.16(c). A typical picture of the initial PSF that we image of the pinhole using the full aperture of the objective is shown in Fig. 1.17(c). At this point it was crucial to count with the advise of J. Andilla, an expert from the Super-resolution Light and Nanoscopy lab from ICFO, to understand the response of our optical system. Initially, we optimized the point spread function with a 25 mm aperture by slightly tweaking the tilt and centering of the bottom objective (which was the most difficult to align properly). In Fig. 1.17(b) we show the image of the pinhole on the intermediate image after the initial optimization. Besides the central maximum we observe 4 lobes which indicate the presence of strong astigmatism. The additional features surrounding the area with biggest intensity show the presence of high order spherical aberrations.

To improve the performance of the optical system, we have corrected the

[55] R1DS1P - Thorlabs

[56] Mounted Precision Pinhole, 1(+0.25/ − 0.10) Pinhole ⌀. P1H - Thorlabs

astigmatism introduced by the vacuum windows by introducing astigmatism on the opposite direction to compensate. To do that we place a window[57] in a place where the image is focusing. In particular we placed it in between the EFL = 500 mm achromat and the intermediate image. Hence, the astigmatism was removed and the PSF recovers qualitatively the shape of an Airy disk, see Fig. 1.17(e) and (f). As it can be observed in Fig. 1.17(e), there are three lobes with small intensity which surround the central peak. This aberration is called trefoil, and it is presumably caused by the mechanical stress induced on the vacuum windows during the welding process. Indeed, this shows that is really crucial to crosscheck the flatness of the windows before and after the welding process. Furthermore, we crosschecked the image of the USAF target. The contrast of the smallest patterns was improved as it can be seen in Fig. 1.17(d).

The correction of the aberrations which we have performed is the correction from the full set-up. However, we do not know which aberrations are introduced by the addressing and the imaging set-ups independently. Indeed, it could be possible that they have independent aberrations which are compensated between each other.

To test the imaging system after correcting the aberrations of the complete optical set-up we imaged bright solitons as we had done in the first characterization stage. The measured sizes where very similar to those obtained in the first stage. Moreover, we imaged bright solitons with different angles of the correcting window and found that the angle of the window was already very close to its optimum. This could indicate that the view-port which introduces larger aberrations is the top view-port. The image of a bright soliton after the optimization process is shown in Fig. 1.18(a). From this image we estimate an upper bound of the imaging resolution of $\sim 3\mu$m.

Later on, we crosschecked the PSF of the pinhole in the intermediate image, see Fig. 1.17(g) and (h). We have observed that the images of the pinhole are not very different as compared to the images in Fig. 1.17(e) and (f). Moreover, we took pictures of the pinhole on the EMCCD camera, see Fig. 1.18(b) and (c). In this case we do observe an Airy disk with a radius of 1.1μm and 1.5μm in each direction. This PSF is much smaller than the size of the bright soliton. Hence,

[57] WG12012-B - Thorlabs

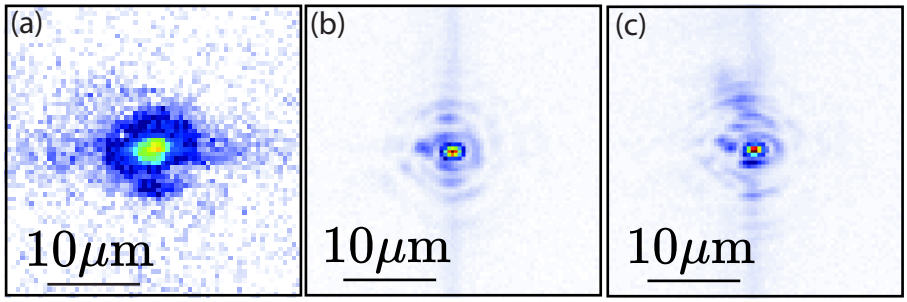

Figure 1.18: (a) *In situ* image of a bright soliton after adjusting the angle from the window taken with the EMCCD camera. (b) PSF of the pinhole on the EMCCD camera after adjusting the angle of the window to optimize the imaging of a bright soliton with a 25 mm aperture and (c) using the full aperture. Notice that the images from the EMCCD camera and the intermediate camera are rotated by 90°

the resolution of our custom-made optical system is not so far from its optimum 1.1μm resolution.

There are mainly three possibilities which might explain the discrepancy between the PSF size of the pinhole and the size of the bright solitons. Either the bright solitons are not small enough, the imaging set-up is not perfect or the imaging technique enlarges the size of the soliton. In order to assess these discrepancies we would need to image a smaller point source in the atomic plane and use a different imaging technique.

In conclusion, we have developed a custom-made optical set-up for imaging and addressing the atoms with high resolution with a performance which is very close to the diffraction limit. To do so, we have understood that the vacuum view-ports are the main source of aberrations of the optical set-up, inducing a small defocusing, large astigmatism, trefoil and high order spherical aberrations. We have corrected the astigmatism introduced by the vacuum view-ports by compensating it with a thick window. Finally, we have been able to image bright solitons with a size of 3 μm, and measured the point spread function. It has a radius (distance between the intensity maximum and the first minimum) of 1.1 μm and 1.5 μm in each direction.

1.5 Cooling sequence after the upgrades

The experimental sequence has been modified due to the upgrade of the 2D MOT and the installation of the imaging and addressing objectives. Since the main part of the cooling sequence remains unchanged, we will focus on the main differences and summarize the atom numbers and temperatures after each cooling stage.

1.5.1 Modifications due to the installation of the 2D MOT

Since the 2D MOT vapor pressure and the quadrupole magnetic field gradient is essentially the same, most of the parameters of the 2D MOT did not change. The powers of the push beams of ^{41}K and ^{39}K have been slightly reduced to $\sim 100\mu$W and 40 μW. The cooling parameters of the 3D MOT remain essentially the same. However in this case we increased the quadrupole gradient slightly from 5.25 G/cm to 6.4 G/cm.

1.5.2 Modifications due to the installation of the microscopes

Indeed, the main modifications of the cooling sequence are due to the installation of the imaging and addressing objectives.

Starting from the laser cooling sequence, the presence of the objectives constrains the size of the vertical MOT beams. Since the BFL length of the objective is very short, the lens needed to compensate the effect of the objective on the MOT beam makes a telescope with a magnification of 0.5, see Fig. 1.19. Therefore the MOT beams are reduced from 25 mm to 12.5 mm waist. Since the installation of the imaging and addressing set-ups was performed in different stages, we could compare the reduction in atom number of the MOT with a single small MOT beam and with the two smaller MOT beams. Whereas the reduction of the top MOT beam size reduced the number of captured atoms, the reduction of the bottom MOT beam size did not. This is because the volume of the MOT was already constrained by the top MOT beam.

Another major implication of the installation of the objectives was the decision to shift the quadrupole trap to center the atoms on the field of view of the

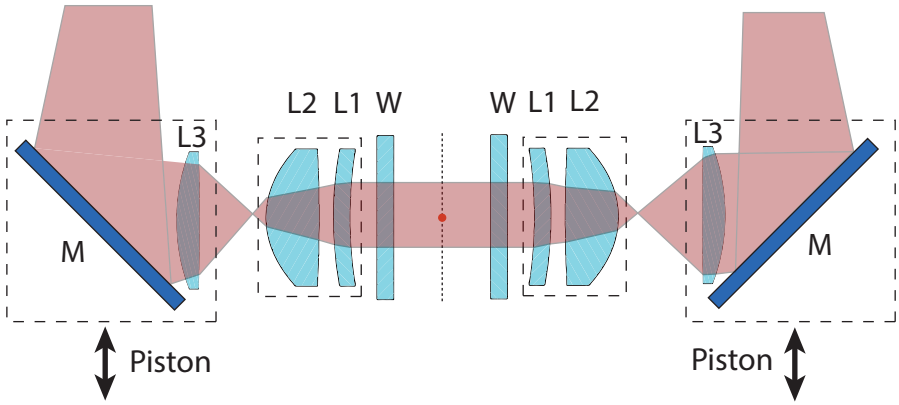

Figure 1.19: Scheme of the MOT beam set-up after the modifications due to the installation of the imaging and addressing microscopes. We have included a lens (L3) on both sides with an effective focal length of 100 mm in order to have the MOT beams collimated on the atomic plane. The back focal length of the microscope is 39.5 mm and the front focal length of the compensating lens is $\sim$ 100 mm. The distance between both lenses is slightly bigger than the sum of both focal lengths. For this reason the incoming beams are slightly diverging in order to be collimated on the atoms. In total, the additional lenses make a telescope with the corresponding objectives with a $\sim$0.5 magnification. The compensating lenses are installed together with an elliptical broad-band dielectric mirror in a pneumatic piston [65]. Thus, we can remove the compensating lenses after the laser cooling stage finishes to provide optical access for the imaging and addressing set-ups.

objectives. During the different installation stages of the imaging, we realized that the magnetic quadrupole is not exactly centered on the geometrical center of the science chamber. Indeed, it is shifted by $\sim$ 1.3 mm to the bottom of the chamber, by $\sim$ 0.75 mm towards the 2D MOT and by $\sim$ 1.1 mm towards the remaining orthogonal direction. The shift of the magnetic quadrupole is done by applying a magnetic field bias on each direction. Although the magnetic field biases are turned on when the magnetic quadrupole is compressed, the magnetic quadrupole is only shifted when we decompress it. The decompression is done in two steps. Initially, we decompress the magnetic quadrupole from 105 G/cm to 17.5 G/cm to place it a waist above the optical dipole trap. Then we reduce

the magnetic quadrupole to 8 G/cm while we reduce the magnetic field biases to keep the position of the quadrupole fixed and load the hybrid trap. After the evaporation of the hybrid trap, we remove the magnetic quadrupole together with the magnetic field shifts and keep a magnetic field bias to keep the quantization axis of the atoms. It is really important that the magnetic field gradient and magnetic field biases are removed avoiding that the zero of magnetic field crosses through the atoms because this would depolarize the cloud.

The rest of the sequence is essentially the same. However, since we need to apply a gradient to pull the state $|F = 2, m_F = 2\rangle$ downwards, we need to modify the coils configuration to perform the spin distillation of ^{41}K and ^{39}K in states $|F = 2, m_F = -2\rangle$ and $|F = 1, m_F = -1\rangle$. Hence, we use H-bridges to switch the vertical coils from Helmholtz to anti-Helmholtz configuration and reverse its polarity. Eventually, we stopped doing the spin distillation and loaded more atoms of ^{39}K so that there would not be any atoms of ^{41}K left after the final evaporation.

1.5.3 Summary of new cooling sequence results

The parameters that we obtain at the end of each cooling stage are summarized in the following list:

- The reduction of the MOT beams size leads to a total of 10^9 and 7×10^7 atoms of ^{41}K and ^{39}K respectively with a temperature around 1 mK.

- At the end of the hybrid D1-D2 compressed MOT we get 9×10^8 and 3×10^7 atoms of ^{41}K and ^{39}K respectively with a temperature around 70μK.

- The simultaneous gray optical molasses on the D1-line allow us to reach temperatures of 16μK with similar atom numbers. Initially we were not reducing the overall intensity of the D1 light for ^{39}K but only decreasing the repumper intensity so that all atoms remain in the gray state. The reason why the reduction of the intensity was not implemented initially was the lack of additional analogue channels to control the intensity. Eventually, we bought an extra analogue card and upgraded the molasses cooling stage.

This modification lead to reach temperatures from $\sim 70\mu$K to 16μK This modification was already reported in the thesis of C. R. Cabrera [65].

- The atoms are optically pumped to the $|F = 2, m_F = 2\rangle$ state and transferred into the magnetic quadrupole trap with almost 100% efficiency.

- We capture all the atoms in a compressed quadrupole trap at around 250μK. We sympathetically cool ^{39}K with ^{41}K reaching temperatures of 30μK and a total number of 4.5×10^7 atoms. We adjust the loading time of ^{39}K to achieve around 2.5×10^7 atoms and 1.5×10^7 atoms of ^{39}K and ^{41}K respectively. If we cool ^{41}K alone we can reach temperatures of 25μK. Due to the reduction of the temperature in the molasses for ^{39}K the efficiency of the sympathetic cooling was improved as compared to the values reported in the thesis of C. R. Cabrera [65], see Fig. 1.20.

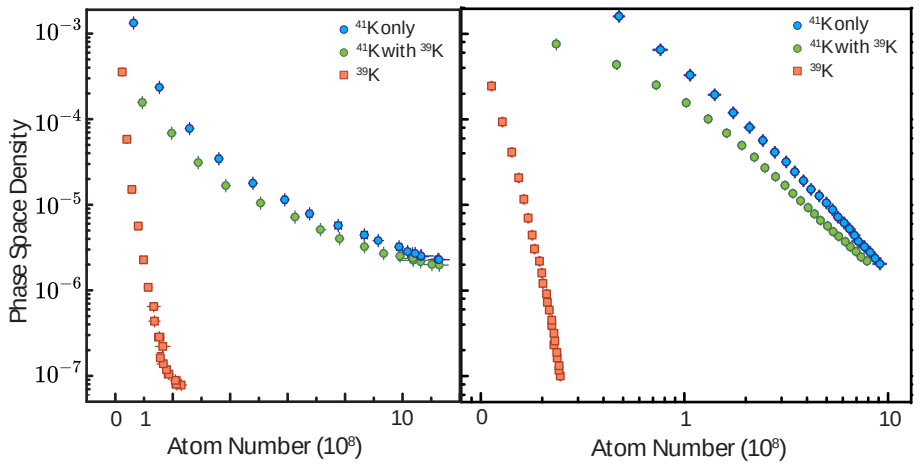

Figure 1.20: Phase space density vs. atom number in the magnetic trap for the cooling of ^{41}K alone, and the sympathetic cooling of ^{39}K with ^{41}K. The left panel shows the results reported in the thesis from C. R. Cabrera [65] and the right panel shows the results after the molasses of ^{39}K were improved.

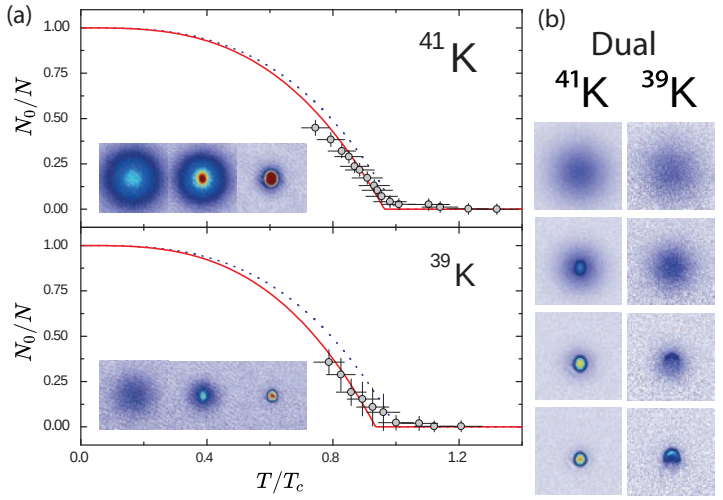

Figure 1.21: (a) Condensed fraction N_0/N vs. T/T_c, where T is the temperature of the cloud and T_c is the critical temperature of a non interaction BEC, for ^{41}K (top panel) and ^{39}K (bottom panel). The experimental data refers to the pure condensation of each species. Whereas the solid red line includes the effect of finite size and interactions on the critical temperature the dashed line does not [88]. The bigger shift on ^{39}K as compared to ^{41}K is due to the difference in scattering lengths ($154a_0$ vs. $60a_0$ respectively). The insets in the top and bottom panels show the distribution of velocities measured in time of flight. We observe the transition from the thermal to the quantum degenerate regime. (b) Dual condensation of ^{41}K and ^{39}K. From top to bottom we show pictures of the evaporation of the mixture. Since the critical temperatures are different they condense at different times. As soon as there is dual condensation there is phase separation [54].

- The atoms are transferred to the hybrid trap by shifting the magnetic quadrupole to center it on the field of view of the microscopes. In this process we do not longer transfer the 15% of the atoms but a 10% at around 8μK. The hybrid evaporation ends up with a total atom number of 1.7×10^6 atoms at 1μK. Cooling both species we can obtain roughly half the atom number of each.

- We transfer around 1.2×10^6 atoms into a crossed dipole trap. After successive hyperfine and Zeeman transfers we perform forced evaporation to reach the degenerate regime. If we want to obtain a pure BEC of ^{39}K, its MOT loading time is adjusted to be left without ^{41}K after the evaporation. We do not perform the spin distillation by transferring ^{41}K to $|F = 2, m_F = -2\rangle$.
- At the end of the evaporation we can obtain pure BECs of ^{41}K and ^{39}K with 1.7×10^5 atoms and 1.4×10^4 atoms respectively, see Fig. 1.21(a). If we adjust the MOT loading balance we can obtain dual BECs with around 7×10^4 atoms per species, see Fig. 1.21(b).

1.6 Conclusion and outlook

In conclusion, we have upgraded our apparatus with a new glass cell 2D MOT and an optical set-up to image and address the atoms with high resolution.

The design of the new glass cell 2D MOT tackles the main issues which we encountered during the operation of the old stainless steel 2D MOT. We have avoided the use metal-to-glass transition materials in order to seal the vacuum view-ports and used only a circular indium wire to seal the glass cell. The quartz glass cell not only provides a similar vapor pressure using smaller temperatures on the oven, but also has a reduced out-gassing as compared to the old stainless steel chamber. Hence, we have been able to maintain the pressure of the 2D MOT chamber with the pumping of the NEG pumps through the differential pumping tube. Additionally, the new 2D MOT contains a cold spot which could be used in the future to facilitate the installation of enriched ^{40}K. In summary, we have improved our 2D MOT and maintained similar atom numbers from the loading of the 2D to the 3D MOT using smaller push powers.

Moreover, we have designed and developed a custom-made high resolution optical set-up for imaging and addressing the atoms *in situ* a performance not too far from the diffraction limit. To do so, we have measured that the main source of aberrations of our optical set-up comes from the vacuum view-ports. We have observed that they introduce a small defocusing, large astigmatism, trefoil and high order spherical aberrations. We have corrected the astigmatism introduced by the windows by compensating it with a thick window. Finally, we

have observed bright solitons with a size of 3 μm, and measured the resolution of the complete optical set-up to be 1.1 μm and 1.5 μm in each direction.

In the future, we could correct the aberrations introduced in our imaging set-up by using a deformable mirror. If we introduce it in a Fourier plane of the image, we could modify the phase for each spatial frequency and also correct the higher order aberrations. Moreover, we could install a digital micromirror device in order to project arbitrary potentials on the atomic cloud. Up to now, we have learned how to use it either in the the Fourier plane or with direct imaging [89, 90]. Additionally, we have corrected the aberrations introduced by the own DMD and its window [86, 91]. Therefore, it is only left to install it in the experiment apparatus to test it on the atoms.

Chapter 2

In situ imaging of two-component Bose-Einstein condensates

Abstract

In this chapter, we develop a polarization phase contrast technique which is able to probe optically dense atomic mixtures at intermediate and high magnetic fields, while exploiting open atomic transitions. We have found a method to directly measure the atomic polarization phase shift and calibrate the corresponding Faraday coefficient, finding good agreement with our theoretical predictions. This technique has been used to image the total column density of a two-component atomic cloud at $B = 57$ G in a dark field. At $B = 396$ G we have demonstrated that we can measure the difference in column density between two states.

2.1 Introduction

In order to extract information of the atomic clouds we probe them with light. There are different techniques which can be used to image an atomic cloud.

Namely absorptive and dispersive techniques. Absorptive techniques are based on the absorption and re-emission of photons, also called fluorescence. Instead, dispersive techniques, also known as phase contrast techniques, are based on the phase shift introduced on the electric field of light by the presence of atoms.

The most commonly used technique is time of flight absorption imaging due to its simplicity. By shining resonant light on the atomic clouds after time of flight, we can compare the shadow cast on the camera with the light in absence of atoms to measure the optical density and extract the density profile of the atoms. In this case, and for long enough time of flight, the measured density profiles are related with the momentum distribution of the cloud *in situ*.

As explained in section 1.4, we have developed a high resolution imaging objective to probe the clouds *in situ* and extract its spatial distribution in the optical trap. The imaging complexity is increased for *in situ* techniques. In general there is not a preferred technique over the others, but one has to take into account the particularities of each system to evaluate the advantages and disadvantages of each technique in order to assess its appropriateness. Let us briefly introduce the different techniques which have been used to probe cold atoms *in situ*.

One of the *in situ* techniques which has been widely used in the cold atoms community is fluorescence imaging. By shining resonant light onto the atoms, they absorb and re-emit photons which are captured by an imaging set-up. Since the re-emission of photons is in general isotropic, only a few collected photons are captured by the imaging system. However, since the probing beam is not aligned with the optical axis of the imaging, fluorescence imaging has the advantage of having a dark background. This technique, has mainly been used to image systems with low optical density, such as atoms trapped in 1D and 2D optical lattices (see reference [92] and references therein) and one-dimensional waveguides [93]. Besides the partial collection of the re-scattered photons, the main limitation of this technique is the blurring of the images due to the photon recoil. In optical lattice experiments, exposure times on the order of a second are needed together with a sub-Doppler cooling mechanism and the use of pinning lattices in order to have single site resolution.

To image optically thick atomic gases *in situ*, such as Bose-Einstein conden-

sates with optical densities on the order of hundreds, absorptive techniques fail at low saturation. One alternative is to use highly saturated absorption imaging [94–96]. This technique involves a subtle calibration due to the nonlinear response of atoms on the imaging intensity. Moreover very short imaging pulses on the μs scale are needed in order to avoid motional blurring due to photon scattering [97]. It is important to note that absorption imaging has to be performed exactly on resonance. Otherwise the atomic cloud can act as a gradient-index lens due to phase dispersion [98].

Another possibility to image optically dense clouds are phase contrast techniques. The main strategy of these techniques is to reduce the optical cross-section by imaging far from resonance. Hence, photon scattering is reduced to reduce the motional blurring and perform non-destructive imaging at the expense of a lower signal. As a consequence electron multiplying cameras have to be used in order to get a good signal to noise ratio. Moreover the imaging can suffer from lensing effects which need to be taken into account [98].

There are different types of phase contrast techniques. As mentioned already, dispersive techniques exploit the phase shift introduced in the electric field of the probing light. This phase shift is produced by the real part of the atomic polarizability, which is a second order rank tensor. Therefore the shift can have a scalar, vectorial and tensor component. Although the tensorial component has been measured in references [99, 100] it is not usually exploited to image. Instead, the scalar and vector phase shifts have been used to image cold atoms. The scalar phase shift is measured by interfering the non-diffracted probe beam with the diffracted light [101]. The vector phase shift rotates the polarization of the probe beam and it can be measured with a polarization beam splitter which acts as a polarization analyzer [102].

In our experiment, we have developed a polarization phase contrast technique which is based on the work described in reference [103] and references therein. With our technique we are able to measure the column density of optically dense atomic mixtures *in situ* at intermediate and high magnetic fields in open transitions. To use this technique, we have developed a direct method to measure the polarization phase shift introduced by the atoms in order to calibrate the effective Faraday coefficient. This technique is flexible enough to measure the

total column density of an atomic cloud as well as to measure the difference in column densities.

In the following section we will explain the physical principle of the light-matter interaction in order to understand how the probing of cold atoms with light works. We show how the atomic polarizability is connected to the index of refraction and how to compute it in the presence of a magnetic field. Afterwards we motivate why polarization phase contrast is particularly suitable for the experiments we performed during the completion of this thesis. Finally we introduce a simple technique to calibrate the vector polarizability and analyse the results obtained at intermediate and high magnetic fields where the experiments carried out during this thesis have been performed.

2.2 Probing cold atoms with light

In order to understand how the different imaging techniques work we will describe the interaction between dilute atomic clouds and light. To do so we will first consider the semi-classical Lorentz model, which describes the atom as a damped harmonic oscillator [104]. This model allows us to calculate the electrically induced dipole moment on an atom and connect the macroscopic index of refraction with the atomic polarizability. As a result we can extract the dispersive and absorptive character of light propagating through a dilute cloud.

Even though this model captures the main features of light-matter interaction, a quantum-mechanical calculation is needed in order to account for the correct value of the polarizability. Thus, in a second stage, we develop briefly this calculation to be able to compute the polarizability of an atom under the presence of a magnetic field. Depending on the magnetic field strength there are analytic formulas for the polarizability. However, given that we want to be able to extract the polarizability for very different magnetic field regimes, we have performed a numerical calculation.

As mentioned previously, from the knowledge of the atomic polarizability we can compute the dispersion of light propagating through an atomic cloud. This dispersion can introduce scalar, vectorial and tensorial shifts depending on the detuning and polarization of the light. In the last part of the chapter we describe

the three processes and how we can compute the associated polarizabilities from the quantum-mechanical calculation.

2.2.1 Semi-classical treatment

The Lorentz model

The Lorentz model is a semi-classical model that assumes that the electron is bound to a steady nucleus with a spring-like force $\vec{F}_{\mathrm{s}} = -m\omega_0^2\vec{x}$, where m is the electron mass, ω_0 is the resonant frequency and $\vec{x}$ is the distance vector pointing from the nucleus to the electron. The electric field of the light induces a force $\vec{F}_{\mathrm{e}} = \vec{e_x} q_{\mathrm{e}} E_0 \cos(\omega t + \phi)$ that makes the electron oscillate at a frequency ω, where q_{e} is the electron charge. The acceleration of the electron induces a radiation that produces a damping force $\vec{F}_{\mathrm{d}} = m\Gamma\dot{\vec{x}}$, where Γ is the linewidth of the optical transition. The resulting equation of motion of the electron position $\vec{x}$ is the following:

$$\ddot{\vec{x}} + \Gamma\dot{\vec{x}} + \omega_0^2\vec{x} = \vec{e_x}\frac{q_{\mathrm{e}}E_0}{m}\cos(\omega t + \phi). \tag{2.2.1}$$

The dipole moment induced on an atom due to the presence of an electric field is proportional to the polarizability: $\vec{d}(\omega) = \alpha(\omega)\vec{E}(\omega)$. Moreover the electric dipole moment of an atom has a magnitude of $\vec{d} = q_{\mathrm{e}}\vec{x}$. Therefore, by solving the equation (2.2.1) of the Lorentz model it can be seen that the polarizability of an atom is given by:

$$\alpha(\omega) = \frac{q_{\mathrm{e}}^2/m}{\omega_0^2 - \omega^2 - i\Gamma\omega}. \tag{2.2.2}$$

For a dilute atomic cloud with an atomic density ρ probed with light with a wavelength λ such that $\rho\lambda^3 \ll 1$, the interaction between many atoms and photons can be treated independently. That is, neglecting collective effects. Under this approximation it can be seen that the index of refraction of an atomic cloud can be approximated to:

$$\tilde{n}(\omega) = \sqrt{1 + \chi(\omega)} \approx 1 + \frac{1}{2}\chi(\omega), \tag{2.2.3}$$

where $\chi(\omega) = \alpha(\omega)\rho/\epsilon_0$ is the electric susceptibility and ϵ_0 is the permittivity of

vacuum. It is easy to see that the real part of the index of refraction introduces a phase on the electric field of the light that propagates through an atomic cloud. Instead, the imaginary part is responsible for the absorption of light.

$$E = E_0 e^{ikz} = E_0 e^{i\tilde{n}k_0 z} = E_0 e^{i\,\mathrm{Re}[\tilde{n}]k_0 z} e^{-\,\mathrm{Im}[\tilde{n}]k_0 z}. \tag{2.2.4}$$

Thus, the phase index $n(\omega) = \mathrm{Re}[\tilde{n}(\omega)]$ and the absorption coefficient $a(\omega) = 2k_0\,\mathrm{Im}[\tilde{n}(\omega)]$ for small detunings $|\omega - \omega_0| \ll \omega_0$ are:

$$n(\omega) = 1 + \frac{\rho q_\mathrm{e}^2}{2m\epsilon_0} \frac{(\omega_0 - \omega)/2\omega_0}{(\omega_0 - \omega)^2 + (\Gamma/2)^2}, \tag{2.2.5}$$

$$a(\omega) = \frac{\rho q_\mathrm{e}^2}{mc\epsilon_0\Gamma} \frac{(\Gamma/2)^2}{(\omega_0 - \omega)^2 + (\Gamma/2)^2}. \tag{2.2.6}$$

The absorption coefficient $a(\omega)$ is related to the optical absorption cross-section $\sigma(\omega)$ by: $a(\omega) = \sigma(\omega)\rho$. Therefore the classical optical absorption cross-section on resonance is:

$$\sigma_0^\mathrm{C} = \frac{q_\mathrm{e}^2}{m\epsilon_0 c\Gamma}. \tag{2.2.7}$$

Although this model is quite simplified, it is able to capture the main features of light-matter interaction for a dilute cloud where atoms are reduced to a two level system. However there are different aspects that the classical model does not capture properly. The quantum mechanical optical cross section is:

$$\sigma_0^\mathrm{Q} = \frac{3\lambda^2}{2\pi}. \tag{2.2.8}$$

As compared to the classical optical cross section, the quantum mechanical one is much larger. In particular, for the D2 transition of potassium: $\sigma_0^\mathrm{C} = 3.95$ nm^2 and $\sigma_0^\mathrm{Q} = 0.28$ μm^2.

In general atoms have multiple energy levels that have to be taken into account. As a result the polarizability contains the contribution of all the possible transitions weighted by the absorption oscillator strength $f_\mathrm{eg} = \sigma_0^\mathrm{Q}/\sigma_0^\mathrm{C}$:

$$\alpha(\omega) = \frac{q_\mathrm{e}^2}{m} \sum_{\mathrm{e}\neq\mathrm{g}} \frac{f_\mathrm{eg}}{\omega_\mathrm{eg}^2 - \omega^2 - i\Gamma_\mathrm{eg}\omega}, \tag{2.2.9}$$

which is the quantum enhancement of the optical cross-section for the transition between the ground and excited states. Here Γ_{eg} corresponds to the linewidth of the transition between the excited state $|\mathrm{e}\rangle$ and the ground state $|\mathrm{g}\rangle$. Moreover we have considered the polarizability as a scalar quantity, whereas the transitions to spherically-non symmetric orbitals are different depending on the polarization of the light. This is the case for the transitions from S to P orbitals. Thus we should consider the polarizability as a tensor instead of a scalar. In conclusion, to evaluate the correct quantitative value of the polarizability a quantum mechanical approach needs to be considered.

Before introducing the quantum mechanical calculation, in the following section, we will introduce the polarizability as a tensor and explain the imaging principle of the Faraday effect which is exploited in the polarization phase contrast imaging technique.

The tensor polarizability and the Faraday rotation effect

As discussed previously, the atomic charge density may react differently to the application of the electric field in different directions due to the anisotropy of the electronic orbitals. Thus we should consider the polarizability as a tensor in analogy to what is done with anisotropic materials:

$$d_i = \alpha_{ij} E_j, \tag{2.2.10}$$

where d_i is the induced dipole on the i-th direction due to the application of an electric field in the j-th direction. If we consider that the "i" and "j" indices indicate principal axes of the system, the polarizability tensor is diagonal. In particular, if the polarizabilities are different for the different axes, the propagation of an electric field through an anisotropic system can introduce a differential phase shift between the electric field polarization of different axes. Therefore the polarization of light can be modified after propagating through an anisotropic system.

In particular, we will focus on the polarization rotation induced by an atomic cloud due to the differential phase shift introduced between the σ^+ and σ^- components of a linearly polarized beam. This effect is commonly known as Faraday

rotation. In the circular polarization basis, the Jones matrix describing the effect introduced by the propagation through the optical media is diagonal:

$$\tilde{M} = \begin{pmatrix} e^{i\theta_+} & 0 \\ 0 & e^{i\theta_-} \end{pmatrix}.$$

As a result, a linearly polarized beam picks up a scalar and vector phase shift after propagating through an atomic cloud. The Jones vector describing the output polarizability is:

$$\vec{J}^{\text{out}} = e^{i\theta_S} \begin{pmatrix} \cos(\theta_V) \\ -\sin(\theta_V) \end{pmatrix},$$

where $\theta_S = \frac{1}{2}(\theta_+ + \theta_-)$ and $\theta_V = \frac{1}{2}(\theta_+ - \theta_-)$ stand for the scalar and vector phase shift.

In the following section we discuss the quantum mechanical calculation. Starting from the calculation of the optical Stark shift we will express the tensor polarizability operator in the circular polarization basis to obtain the scalar and vector phase shifts. Then we will introduce the atomic level structure to understand its complexity and calculate the energy level splittings. Finally we explain the details of the calculation at different magnetic fields, show the relation between the dipole matrix elements and the transition linewidth and compute the scalar and vector polarizabilities at different magnetic fields.

2.2.2 Quantum - mechanical treatment

The optical Stark shift

The interaction of an atom with an oscillating electric field is given by the following Hamiltonian:

$$H_{\text{AF}} = -\vec{E}(t) \cdot \vec{d}, \tag{2.2.11}$$

where $\vec{d}$ is the dipole operator. Treating the electric field as a time-dependent perturbation to the atomic energy it can be seen that the electric field induces the so-called Stark shift:

$$\Delta E^{(2)} = -\frac{1}{2}\langle E_i^* \alpha_{ij}(\omega) E_j \rangle, \tag{2.2.12}$$

where α_{ij} is the polarizability tensor operator. When $|\omega_{\mathrm{eg}} - \omega| \ll \omega_{\mathrm{eg}}$ we can apply the Rotating Wave Approximation (RWA) and the expectation value of the polarizability tensor reads

$$\langle \alpha_{ij} \rangle_{\mathrm{gg}} = \frac{1}{\hbar} \sum_{\mathrm{e} \neq \mathrm{g}} \left(\frac{\langle \mathrm{g}| \vec{d}^{\dagger} \cdot \vec{\epsilon}_i |\mathrm{e}\rangle \langle \mathrm{e}| \vec{d} \cdot \vec{\epsilon}_j |\mathrm{g}\rangle}{\omega_{\mathrm{eg}} - \omega - i\Gamma_{\mathrm{eg}}/2} \right), \tag{2.2.13}$$

where $|\mathrm{g}\rangle$ and $|\mathrm{e}\rangle$ are the ground and excited states, $\vec{\epsilon}_i$ is the polarization of the light on the i-th direction, ω_{eg} is the transition frequency between ground and excited state and Γ_{e} is its natural linewidth. We recover the main features that were described by the Lorentz model. Notice that the expectation value of the polarizability tensor does not depend on the spatial-basis choice. Therefore

$$\langle \alpha_{ij} \rangle_{\mathrm{gg}} = \langle \alpha_{qq'} \rangle_{\mathrm{gg}} = \frac{1}{\hbar} \sum_{e \neq g} \left(\frac{\langle g| d_q^{\dagger} |e\rangle \langle e| d_{q'} |g\rangle}{\omega_{\mathrm{eg}} - \omega - i\Gamma_{\mathrm{eg}}/2} \right), \tag{2.2.14}$$

where q denotes a certain vector component of the spherical basis. In further sections it will be clear that this basis is particularly good to compute the dipole matrix elements.

In the following section we introduce the energy level structure of an atom under the presence of a magnetic field to be able to compute the dipole matrix elements and energy splittings ω_{eg}.

Fine-structure, hyper-fine structure and the Zeeman effect

The energy of an atom under the presence of a magnetic field is described by a Hamiltonian containing three contributions: the fine-structure, the hyperfine-structure and the Zeeman effect [105].

$$H = H_{\mathrm{FS}} + H_{\mathrm{HFS}} + H_{\mathrm{Z}} \tag{2.2.15}$$

The fine-structure splitting of an atom is the result of the coupling between the electronic spin $\vec{S}$ and its orbital angular momentum $\vec{L}$. The total electronic

angular momentum is given by $\vec{J} = \vec{L} + \vec{S}$. For alkali atoms this contribution gives rise to the D1 and D2 transitions. In particular, for potassium $\lambda_{D1} = 770.108$ nm and $\lambda_{D2} = 766.701$ nm [106].

The hyper-fine structure splitting is given by the coupling between the total electronic angular momentum $\vec{J}$ and the nuclear angular momentum $\vec{I}$:

$$H_{HFS} = \frac{A_{HF}}{\hbar^2} \vec{I} \cdot \vec{J}, \tag{2.2.16}$$

where A_{HF} is the magnetic dipole hyperfine constant. The energy levels of all the potassium isotopes at zero magnetic field are sketched in Fig. 2.1.

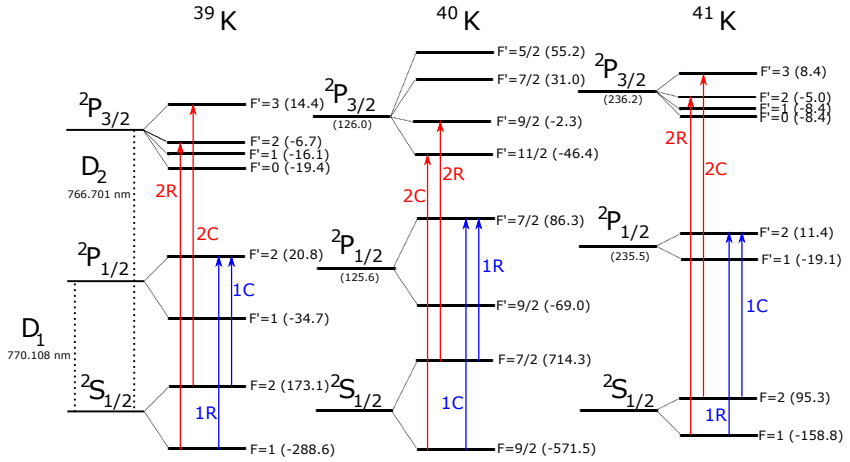

Figure 2.1: Fine and hyperfine structure of the three isotopes of potassium. In parenthesis we show the fine energy shifts of all isotopes in MHz with respect to the energy of the corresponding fine state for as well as the corresponding hyperfine energy shifts. The red and blue lines show the cooler (C) and repumper (R) transitions on the D2 and D1 lines. Image taken from [76] and energy level splittings taken from [106].

The Zeeman effect is the splitting of the hyperfine structure into different energy levels due to the presence of a magnetic field. The Zeeman Hamiltonian for $\vec{B} = B_z \vec{e_z}$ is:

$$H_Z = -\vec{\mu} \cdot \vec{B} = -\frac{\mu_B}{\hbar}(g_S \vec{S} + g_L \vec{L} + g_I \vec{I})\vec{B} = -\frac{\mu_B}{\hbar}(g_S S_z + g_L L_z + g_I I_z)B_z, \tag{2.2.17}$$

where μ_B is the Bohr magnetion, and g_S, g_L and g_I are the corresponding Landé factors. Given that $g_I \ll g_S, g_L$ we will just consider the Zeeman effect on the electronic part. Depending on the magnitude of B_z we can compute the energies under different approximations. At low magnetic fields H_Z can be treated as a perturbation to the hyperfine structure Hamiltonian. At this field the good quantum numbers to describe the atomic state are the total angular momentum $\vec{F} = \vec{I} + \vec{J}$ and its projection m_F. Instead, for strong magnetic fields the energy shift becomes larger and the hyper-fine splitting can be treated as a perturbation. In this regime, the so-called Paschen-Back regime, the nuclear and electronic angular momentum are decoupled and the good quantum numbers are $|I, m_I, J, m_J\rangle$. In particular, for potassium the hyperfine splittings are rather small and the Paschen-Back regime is reached for fairly low magnetic fields.

The atomic polarizability in the presence of a magnetic field

To calculate the atomic polarizability at a particular magnetic field we have to make a choice of basis. We have chosen to work on the high field basis $|I, m_I, J, m_J\rangle$ because we perform the imaging either in the Paschen Back regime or in an intermediate magnetic field regime. We have numerically diagonalized $H_{HFS} + H_Z$ for the states $^2S_{1/2}$, $^2P_{1/2}$ and $^2P_{3/2}$ to be able to compute all the energy level splittings ω_{eg}. The energies of these states are plotted in Fig. A.1, A.2 and A.3 of appendix A respectively.

To compute the dipole matrix elements $\langle e| d_q |g\rangle$ we make use of the Wigner-Eckart theorem. Considering a state $|\alpha, J, m_J\rangle$, where α denotes all the quantum numbers that do not have an angular dependency, the Wigner-Eckart theorem allows us to split the dipole matrix elements $\langle \alpha, J, m_J| d_q |\alpha', J', m'_J\rangle$ into reduced dipole matrix dipole elements $(\alpha, J||\vec{d}||\alpha', J')$, which are angular independent, and Clebsch-Gordan coefficients $\langle J, m_J; l = 1, m_{l=q}|J', m'_J\rangle$ [107]:

$$\langle \alpha, J, m_J| d_q |\alpha', J', m'_J\rangle = \frac{(\alpha, J||\vec{d}||\alpha', J')}{\sqrt{2J+1}} \langle J, m_J; l = 1, m_{l=q}|J', m'_J\rangle , \quad (2.2.18)$$

where l and m_l are the angular momentum of the photon and its projection along z, and $q = 1, -1, 0$ depending on whether the polarization of light is σ^+,

σ^- or π. From equation (2.2.18) it is implicit that the light only couples to the electronic state. The reduced matrix dipole elements are related to the decay rate as:

$$\Gamma_{\mathrm{eg}} = \frac{\omega_{\mathrm{eg}}^3 |\langle \mathrm{e}|\, \vec{d}\, |\mathrm{g}\rangle|^2}{3\pi\epsilon_0\hbar c^3}, \tag{2.2.19}$$

where the ground and excited states correspond to particular $|\alpha, J, m_J\rangle$ states. Typically, the decay rate Γ_{eg} between particular excited and ground states cannot be resolved and normally there is a total decay rate measurement for the D1 and the D2 transitions. As a result, the measurement of the reduced matrix dipole elements is given by [108]

$$|(\alpha, J||\vec{d}||\alpha', J')| = \left(\frac{3\pi\hbar c^3 \Gamma_{\mathrm{eg}}^{\mathrm{tot}}(2J+1)}{\omega_{\mathrm{eg}}^3}\right)^{1/2}. \tag{2.2.20}$$

Consequently, a normalization factor $\sqrt{2J+1}$ was included in equation (2.2.18) to account for the factor appearing in equation (2.2.20).

Finally, to compute the tensor polarizability, we have to calculate

$$\left\langle I, m_I, J, m_J \middle| d_q^\dagger | I', m_I', J', m_J' \right\rangle \langle I', m_I', J', m_J' | d_{q'} | I, m_I, J, m_J \rangle . \tag{2.2.21}$$

This product is equal to 0 if $q \neq q'$ and therefore the polarization tensor operator is diagonal on the $|I, m_I, J, m_J\rangle$ state basis represented on the spherical coordinate system. Hence, it becomes clear why this basis and coordinate representation are appropriate for the calculation of the atomic polarizability.

To compute the scalar and vector polarizabilities, and in analogy with the classical result from Jones calculus, we use the following equations:

$$\alpha_{\mathrm{g}}^{\mathrm{S}} = \frac{1}{2}\left(\langle\alpha_{q=1,q'=1}\rangle_{\mathrm{gg}} + \langle\alpha_{q=-1,q'=-1}\rangle_{\mathrm{gg}}\right), \tag{2.2.22}$$

$$\alpha_{\mathrm{g}}^{\mathrm{V}} = \frac{1}{2}\left(\langle\alpha_{q=1,q'=1}\rangle_{\mathrm{gg}} - \langle\alpha_{q=-1,q'=-1}\rangle_{\mathrm{gg}}\right). \tag{2.2.23}$$

The development of the program to compute the polarizability vs. magnetic field was developed by B. Naylor. To crosscheck that our calculation of the polarizability is correct we have computed the well-known scattering cross-section

for ^{39}K on the closed transition $|F = 2, m_F = 2\rangle \longrightarrow |F' = 3, m_{F'} = 3\rangle$. This is a particularly good transition for imaging because all the atoms in $|F' = 3, m_{F'} = 3\rangle$ can only spontaneously decay to $|F = 2, m_F = 2\rangle$. Hence it is a good two-level system. We can compare the results from Fig. 2.2 to the resonant quantum mechanical cross-section computed from equation (2.2.8). For this transition $\sigma^{\mathrm{Q}} = 0.281\ \mu\mathrm{m}^2$, which agrees with the computed cross-section on resonance, see Fig. 2.2. Moreover, as a crosscheck, we have computed the scalar and vector polarizabilities at zero magnetic field for ^{133}Cs and ^{87}Rb obtaining the results shown in references [99, 100].

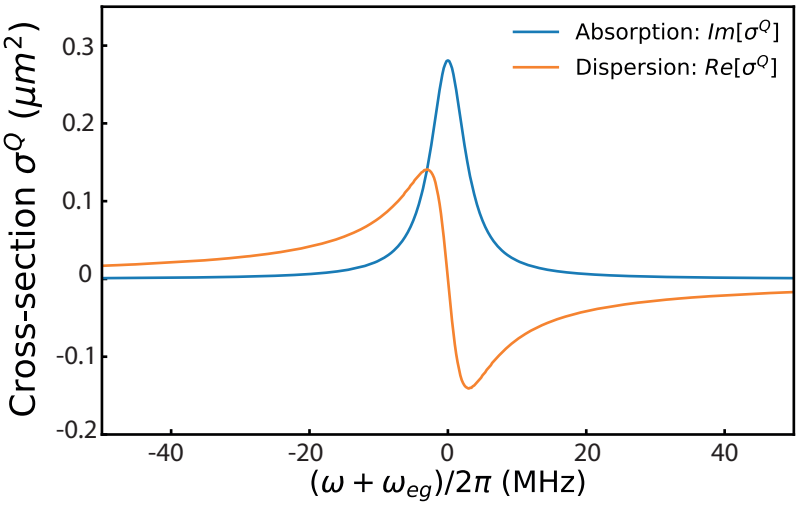

Figure 2.2: Quantum mechanical scattering cross-section for the $|F = 2, m_F = 2\rangle \longrightarrow |F' = 3, m_{F'} = 3\rangle$ of ^{39}K. The absorptive and dispersive parts correspond to the imaginary and real parts of $\sigma^{\mathrm{Q}} = k_0\alpha/\epsilon_0$ respectively.

Let us now focus on the polarizabilities of the states on the $F = 1$ manifold, which are the states that we have mainly used to perform experiments throughout the completion of this thesis. This states do not form a closed transition with any of the states on the D1 and D2 transitions. Hence their polarizability will have contributions from different allowed transitions.

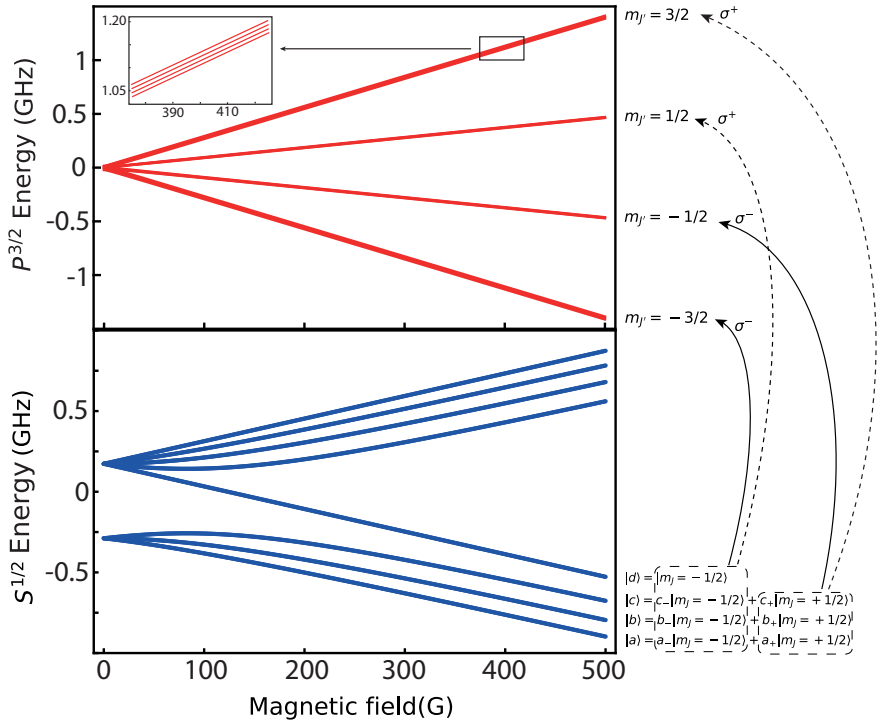

Figure 2.3: Top panel: Energy of the $^2P_{3/2}$ of ^{39}K state versus magnetic field. The energy is referenced with respect to the D2 transition. There are 16 energy levels from the $F' = 0, 1, 2$ and 3 manifolds, which at high field separate into four m'_J branches composed by four magnetic sublevels as shown in the inset. Bottom panel: Energy of the $^2S_{1/2}$ state of ^{39}K versus magnetic field. The zero of energy corresponds to the $^2S_{1/2}$ state fine structure energy. The three lowest energy levels, $|a\rangle$, $|b\rangle$ and $|c\rangle$, are superpositions of the corresponding $|m_J = -1/2\rangle$ and $|m_J = 1/2\rangle$ electronic states. Their composition depends on the magnetic field. The energy level labeled as $|d\rangle$ is a streched state. The ground states can be coupled to the excited states via σ^+ and σ^- light as shown by the dashed and solid arrows respectively.

For simplicity we will label the three-lowest energy states as: $|a\rangle$, $|b\rangle$ and $|c\rangle$,

see Fig. 2.3. At zero magnetic field we can identify them as:

$$\begin{aligned} |a\rangle &\equiv |F=1, m_F=1\rangle \\ |b\rangle &\equiv |F=1, m_F=0\rangle \\ |c\rangle &\equiv |F=1, m_F=-1\rangle \end{aligned}$$

whereas at high field they correspond to:

$$\begin{aligned} |a\rangle &\equiv |I=3/2, m_I=3/2, J=1/2, m_J=-1/2\rangle \\ |b\rangle &\equiv |I=3/2, m_I=1/2, J=1/2, m_J=-1/2\rangle \\ |c\rangle &\equiv |I=3/2, m_I=-1/2, J=1/2, m_J=-1/2\rangle \end{aligned}$$

At intermediate fields, such as $B \sim 57$ G, where the experiments from chapters 3, 4 and 5 are performed, these states contain contributions of different $|I, m_I, J, m_J\rangle$ states. In particular, for the droplet experiments, we have used the $|b\rangle$ and $|c\rangle$ states. At $B = 57$ G their composition is the following:

$$\begin{aligned} |b\rangle &= -0.815\,|3/2, 1/2, 1/2, -1/2\rangle + 0.580\,|3/2, -1/2, 1/2, 1/2\rangle \\ |c\rangle &= -0.642\,|3/2, -1/2, 1/2, -1/2\rangle + 0.767\,|3/2, -3/2, 1/2, 1/2\rangle \end{aligned}$$

If we probe these states with linear polarization close to the D2 transition, the σ^+ (σ^-) component will couple them to the excited states with $m_{J'} = 1/2$ and $3/2$ ($m_{J'} = -1/2$ and $-3/2$). In Fig. 2.4 we plot the scalar and vector polarizability of $|a\rangle$, $|b\rangle$ and $|c\rangle$ for frequencies around the D2 transition. As it can be seen both polarizabilities contain four features corresponding from the $m_{J'} = -3/2$ to the $m_{J'} = 3/2$ starting from around 0.1 GHz detuning to 0.5 GHz. Hence, the polarizability of these states at a particular frequency has contributions of several excited states as shown in Fig. 2.3.

At high field, the states on the $F = 1$ manifold are in the Paschen-Back regime and they correspond mainly to a single $|I, m_I, J, m_J\rangle$ state. Therefore the polarizability at high field will not contain as many contributions from the

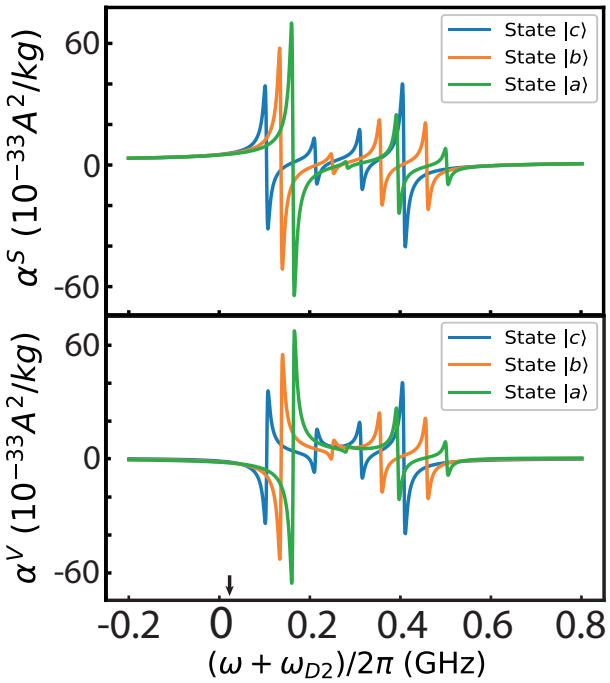

Figure 2.4: Scalar and vector polarizabilities of the ^{39}K $^2S_{1/2}$ states at $B = 57$ G vs frequency around the D2 transition, top and bottom panels respectively. The states $|a\rangle$, $|b\rangle$ and $|c\rangle$ are the ones that connect to the $|F = 1, m_F = 1\rangle$, $|F = 1, m_F = 0\rangle$ and $|F = 1, m_F = -1\rangle$ respectively at $B = 0$ G as shown in Fig. 2.3. The arrow points the frequency used to image at low field.

excited states. Currently, we are working on experiments on spin-orbit coupling[1] at 396 G with states $|a\rangle$, $|b\rangle$. In particular the composition of these states is:

$$\begin{aligned} |a\rangle &= 0.990\,|3/2, 3/2, 1/2, -1/2\rangle - 0.144\,|3/2, 1/2, 1/2, 1/2\rangle \\ |b\rangle &= 0.981\,|3/2, 1/2, 1/2, -1/2\rangle - 0.196\,|3/2, -1/2, 1/2, 1/2\rangle \end{aligned}$$

Therefore the scalar and vector polarizabilities around the D2 transition mainly have contributions of the transition to the $m_{J'} = -3/2$ and $m_{J'} = 1/2$

[1]These experiments will be explained in the PhD theses of A. Frölian and C. S. Chisholm.

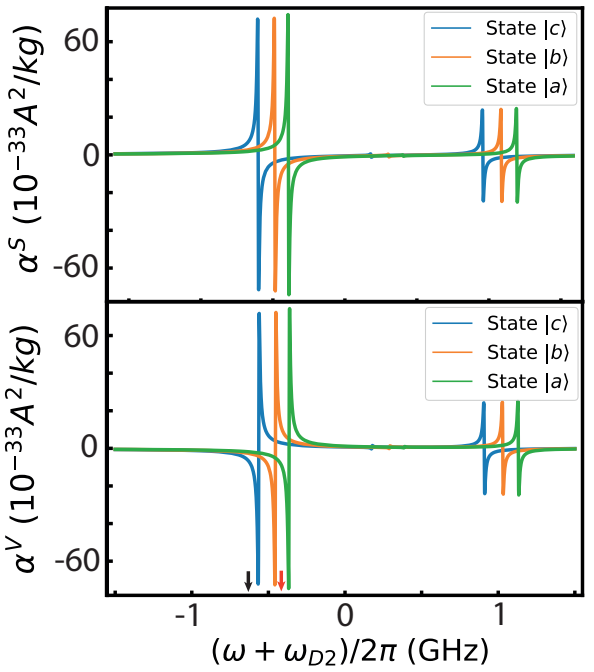

Figure 2.5: Scalar and vector polarizabilities of the ^{39}K $^2S_{1/2}$ states at $B = 396$ G vs frequency around the D2 transition, top and bottom panels respectively. The states $|a\rangle$, $|b\rangle$ and $|c\rangle$ are the ones that connect to the $|F = 1, m_F = 1\rangle$, $|F = 1, m_F = 0\rangle$ and $|F = 1, m_F = -1\rangle$ respectively at $B = 0$ G as shown in Fig. 2.3. The black and red arrows point the frequencies used to image at high field.

states. As it can be seen in Fig. 2.5 these transitions correspond to the dispersive features around -0.5 GHz and 1 GHz detuning respectively. Hence it becomes clear that the polarizability at high field at a particular frequency has more resemblance to the two-level system dispersion.

Now that we have introduced the polarizabilities at $B = 57$ G and $B = 396$ G, we have to make a choice between the scalar and vector polarization phase contrast techniques. In the experiments performed so far we decided to measure the vector instead of the scalar phase shift for simplicity. The technical details about this choice will be clarified in section 2.3. Before entering into details, in the following section we will discuss the differences between the scalar and

vector polarizabilities at intermediate and high fields, and the detunings that we chose to image potassium mixtures with a polarization phase contrast imaging technique.

Scalar vs. vector polarizability for imaging mixtures at intermediate and high magnetic fields

Whereas the scalar polarizability contains the sum of the σ^+ and σ^- contributions, the vector polarizability contains the difference, as seen from equations (2.2.22) and (2.2.23). Close to resonance, the magnitude of the scalar and vector polarizabilities are very similar, as shown in Fig. 2.4 and 2.5. Far from resonance, the contributions from the different transitions sum up for the scalar polarizability and can cancel each other for the vector polarizability depending on the spin composition of the ground states. As already explained, the composition of the ground states is formed by $m_J = -1/2$ and $m_J = 1/2$ electronic states, which couple respectively to the $m_{J'} = -3/2$ ($m_{J'} = 1/2$) and $m_{J'} = -1/2$ ($m_{J'} = 3/2$) via $\sigma^-(\sigma^+)$ light as shown in Fig. 2.3. Provided that the Clesbch-Gordan coefficients satisfy the symmetry relation $\langle J, m_J; l = 1, m_{l=\mathrm{q}}|J', m'_J\rangle = -\langle J, m_J; l = 1, m_{l=\mathrm{q}}|J', -m'_J\rangle$ [107], if the composition of the ground state is 50/50 then the vector polarizability vanishes far from resonance, see Fig. 2.4. For this reason, at B = 57 G, where the composition of $|b\rangle$ and $|c\rangle$ is almost balanced, we cannot measure the vector phase shift far from resonance. Instead, at B = 396 G, the scalar and vector phase shifts are also similar far from resonance, see Fig. 2.5.

In the presence of a mixture the polarization rotation contains the contribution of both components and thus

$$\theta_{\mathrm{A}} = c_{\mathrm{F}1} n_1 + c_{\mathrm{F}2} n_2 \tag{2.2.24}$$

where θ_{A} is the polarization phase shift introduced by the atoms and $c_{\mathrm{F}i}$ and $n_i = \int \rho_i(x, y, z)dz$ are the Faraday coefficient and column density (integrated along the imaging axis) from the i-th component. In general there are two interesting cases: if $c_{\mathrm{F}1} = c_{\mathrm{F}2}$, θ_{A} reflects the sum of the column densities whereas if $c_{\mathrm{F}1} = -c_{\mathrm{F}2}$ it reflects the difference. In the experiments that we carried out during the completion of this thesis (chapters 3, 4 and 5) it was crucial to work in a regime

where $c_{F1} \approx c_{F2}$ to measure the total atom number. Additionally, in this system the stability of the droplets depends on the ratio of population between the two components, and it would have been really interesting to measure the difference in population between the two. However, at low field the condition $c_{F1} = -c_{F2}$ is achieved very close to resonance. Instead, at high field the energy level splittings are much bigger and the $c_{F1} = -c_{F2}$ are met further from resonance.

Under the previous considerations, we have chosen to image the mixtures with a frequency such that for B = 57 G the light for $|b\rangle$ and $|c\rangle$ is red detuned by 17.5Γ and 12.2Γ from the closest transitions to measure the total atom number (black arrow in Fig. 2.4). Similarly, for B = 396 G, $|a\rangle$ and $|b\rangle$ are red detuned by 44.7Γ and 29.7Γ from the closest transitions (black arrow in Fig. 2.5). For these detunings, the imaging is destructive, as it is shown in section 2.3. Additionally, to measure the difference of column densities, at B = 396 G, we performed some experiments with light which was red (blue) detuned from the $|a\rangle$ ($|b\rangle$)$\rightarrow m_{J'} = -3/2$ transitions by 7.5Γ (red arrow in Fig. 2.5).

In the following section we will explain how the polarization phase contrsat technique works, how do we calibrate it, what are the results obtained at intermediate and high magnetic fields and how the technique is used to image a spin mixture *in situ*.

2.3 Experimental characterization of polarization phase contrast imaging

As mentioned previously the motivation to image the clouds *in situ* with a polarization phase contrast technique is to image optically dense mixtures with column densities on the order of 10^{14} m^{-2} with good signal to noise ratio and minimal motional blurring. The technique that we use was initially developed in reference [102]. In particular, the implementation we employ is closely based on the work from M. Gajdacz *et al.* [103]. In section 2.3.1, we will explain the concept of the experimental implementation of the polarization phase contrast technique. The setup that we developed to implement this technique is detailed in section 2.3.2. Afterwards, in section 2.3.3, we explain the imaging analysis procedure

to extract the atomic polarization phase shift. Then we describe the technique used to calibrate the atomic polarization phase shift in section 2.3.4. Finally, in section 2.3.5, we present the results that we obtained to image the sum and difference of column densities of a potassium mixture.

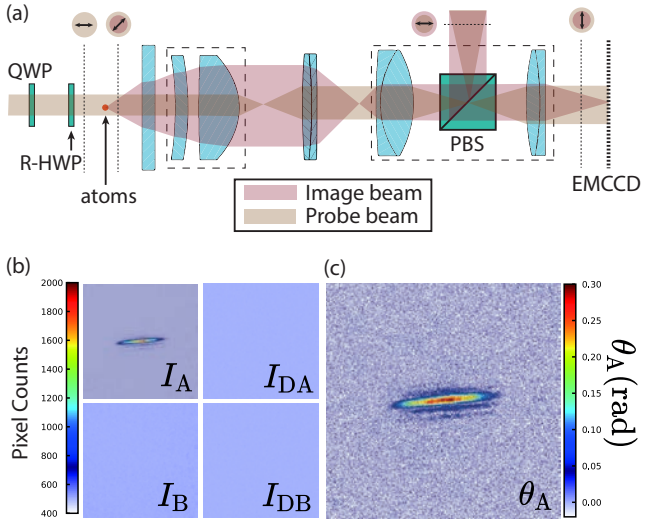

Figure 2.6: (a) Scheme of the polarization phase contrast set-up. A linearly polarized beam is sent through the atoms, which rotate its polarization due to its birefringent character. In the middle of the imaging system a polarization beam splitter works as a polarization analyzer which measures the rotation of the polarization induced by the atoms. The images are taken on an EMCCD camera. To adjust the polarization we use true zero order quarter and half waveplates (768.4 nm). The half waveplate is mounted on a motorized rotating mount to probe the atomic cloud with different input polarizations. (b) Images taken with the EMCCD camera in dark field configuration. In the absence of atoms no light goes to the camera. Top left: I_A. Bottom left: I_B. Top right: I_{DA}. Bottom right: I_{DB}. The color scale shows the pixel counts. (c) Atomic polarization phase shift retrieved from the images in (b). The color scale shows θ_A.

2.3.1 Concept

How do we implement the polarization phase contrast technique in our experiment? In Fig. 2.6(a) we show a schematic of the experimental implementation. First of all we prepare a laser light beam with linear polarization. The laser setup that we use is described in section 2.3.2. A rotating $\lambda/2$ waveplate[2] is used to adjust the polarization orientation. The imaging beam is sent through the vacuum chamber to image the atoms. Once the imaging beam crosses the atomic cloud the scattered light picks up a scalar and vector phase shift. The imaging beam crosses the imaging system presented in section 1.4. In the middle of the imaging system a polarization beam splitter[3] acts as a polarization analyzer. By contrast with the non-scattered light, we image the polarization phase shift introduced by the atoms in an electron multiplying charged-coupled device camera[4].

In the imaging process we take four pictures, see Fig. 2.6(b). First we take an image of the atomic cloud I_{A} followed[5] by a picture without atoms, which we call bright image I_{B}. After 1 second of readout time, we take two more pictures without any light that we use to remove the background from the atoms and bright pictures. They are called respectively dark atoms I_{DA} and dark bright I_{DB} pictures. The signal that we get on the camera, assuming that the polarization is perfectly linear is:

$$I_{\mathrm{A}}(i,j) = \beta(i,j) \cdot \sin^2(\theta_{\mathrm{A}}(i,j) + \theta) + I_{\mathrm{DA}}(i,j) \tag{2.3.1a}$$

$$I_{\mathrm{B}}(i,j) = \beta(i,j) \cdot \sin^2(\theta) + I_{\mathrm{DB}}(i,j) \tag{2.3.1b}$$

where β is the probe beam intensity, θ is the input polarization angle with respect to the polarization beam splitter axis, θ_{A} is the polarization phase shift introduced by the atoms and (i,j) indicate the pixel index.

There are two main configurations that can be used to image the atomic

[2]True zero order $\lambda/2$ waveplate from FOCtek (WPF212H 768.4 nm) installed on a motorized precision rotation stage from Thorlabs (PRM1Z8) driven by the K-Cube Brushed DC Servo Motor Controller (KDC101).

[3]Thin film polarizer from Qioptiq (Size: 25 mm × 25 mm × 25 mm. Extinction ratio 10^{-4}.)

[4]EMCCD: Andor iXon Ultra 897

[5]There is a 1.7 ms delay between both pictures due to the frame transfer of the camera.

clouds. If we set $\theta = 0$, most of the light from the probe beam is discarded and the images are taken in the dark-field configuration. For small polarization phase shifts θ_A the signal I_A is quadratic on the polarization phase shift. Instead, if we set $\theta = \pi/4$, the probe beam is split in half in the polarization analyzer and the signal I_A is linear for small polarization phase shifts.

In our experiment we generally take images in the dark field configuration. In section 2.3.3 we will detail the analysis of the pictures in order to extract the column density of the imaged cloud and introduce the advantages and disadvantages of working in dark field. In the following section we will explain the experimental set-up to image the atomic cloud *in situ* using the polarization phase contrast technique.

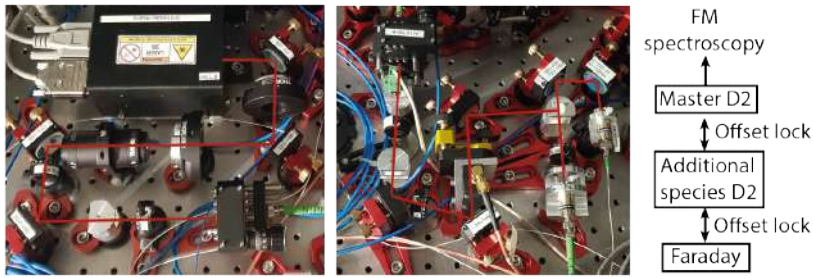

Figure 2.7: Faraday laser set-up. Left panel: The DFB Faraday laser beam is shaped using cylindrical lenses and coupled into a single mode polarization maintaining fiber after passing through an optical isolator. Middle panel: The Faraday laser is split in two. The left path goes into the fiber which sends the light into the experiment table. We use an AOM to adjust the probe beam intensity and as a switch together with a mechanical shutter. The right path goes into a polarization maintaining fiber optic 2×2 coupler, which mixes the light from the Faraday laser with the ^{39}K D2 laser to generate the offset lock. The ^{39}K D2 is offset locked with respect to the Master D2 laser, which is locked on a hot potassium vapor cell using frequency modulated spectroscopy (right panel).

2.3.2 Experimental Faraday set-up

The experimental Faraday set-up is divided in two parts. The laser set-up which we use to prepare the laser light to probe the atomic cloud and the imaging set-up. Since the imaging set-up has been described in detail in section 1.4, we will focus on the particular details concerning the polarization phase contrast imaging and detail the Faraday laser set-up.

Faraday laser set-up

The light that we use to probe the atomic clouds with this technique is produced by a DFB laser[6], which we name Faraday laser. In contrast to absorption imaging, we do not need a laser with a narrow linewidth because the imaging is performed far from resonance. Whereas for absorption time of flight imaging we employ light with $\sim$ 300 kHz linewidth[7] for these technique we use a $\sim$ 1 MHz linewidth DFB laser. The laser setup that we use is shown in Fig. 2.7. The light from the Faraday laser is offset locked to the additional species D2 laser which is offset locked to the D2 master laser [65, 109]. A Voltage Controlled Oscillator (VCO) on the offset lock of the Faraday laser is used to be able to tune the frequency of the laser. We will call this frequency the Faraday beat detuning $\Delta^{\mathrm{FAR}}_{\mathrm{BEAT}}$. In Fig. 2.8(a) and (b) we plot the Faraday coefficients that will be relevant throughout this thesis with respect to this detuning. The relation between the frequency of the Faraday laser light that we shine on the atoms and $\Delta^{\mathrm{FAR}}_{\mathrm{BEAT}}$ is described in appendix B.

Faraday imaging set-up

The set-up which we use to image the atomic clouds *in situ* has been detailed in section 1.4. In particular, for the Faraday imaging set-up we need to ensure that the polarization that we send to the atoms is linear. We designed the optical set-up in order to have the least possible number of components before the probe beam reaches the atoms. Nevertheless the probe beam still crosses several optical elements that could introduce a circular component on the polarization,

[6] EYP-DFB-0767-00050-1500-TOC03-0005 - Eagleyard photonics
[7] Generated with an External Cavity Diode Laser (ECDL). SYST DL PRO 780 - TOPTICA

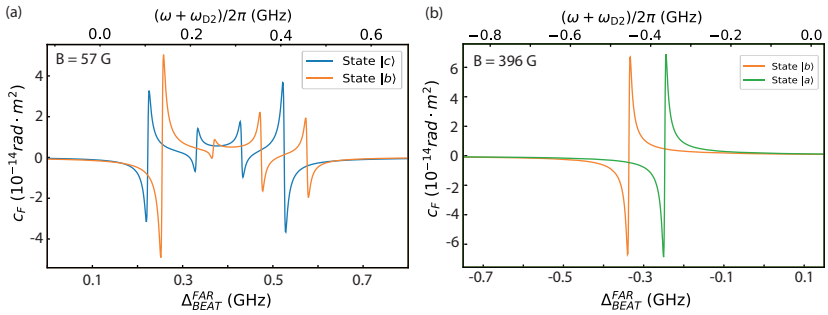

Figure 2.8: Faraday coefficient vs Faraday detuning at B = 57 G (a) and B = 396 G (b) for states $|a\rangle$ (green line), $|b\rangle$ (orange line) and $|c\rangle$ (blue line).

see Fig. 1.9. Ideally, we would crosscheck the polarization right before the vacuum chamber. However the physical access makes it difficult to measure the polarization before. Instead, we adjust the polarization with a true zero order $\lambda/4$ and a $\lambda/2$ waveplate to get into the dark field configuration. The polarization analyzer we use is a polarization beam splitter with a 10^{-4} extinction ratio. In the dark field configuration we have a polarization impurity of $1.5 \cdot 10^{-3}$ before the polarization analyzer and of 1% after the imaging objective. For all practical purposes, we will consider the incident polarization on the atoms as if it was purely linear in the imaging analysis.

2.3.3 Imaging analysis of the atomic polarization rotation

The imaging analysis of the data taken in the experiments shown in chapters 3 and 4 was done in collaboration with L. Tanzi.

In order to extract the polarization phase shift θ_{A} from the pictures in Fig. 2.6(b), we use the equations (2.3.1a) and (2.3.1b). In the dark field configuration ($\theta = 0$) we have that:

$$\theta_{\mathrm{A}} = \arcsin\left(\sqrt{\frac{I_{\mathrm{A}}(i,j) - I_{\mathrm{DA}}(i,j)}{\beta(i,j)}}\right). \tag{2.3.2}$$

Since in the dark field configuration $I_{\mathrm{B}} = I_{\mathrm{DB}}$, we have to calibrate $\beta(i,j)$ inde-

pendently. We calibrate it by measuring the intensity on the camera at $\theta = \pi/2$. Since the probe beam has a waist on the order of[8] 1 mm and the atomic clouds have sizes on the order of 10 μm, we consider the probe beam as homogeneous. Thus, we take an average of the pixel counts $\bar{\beta}$ around the cloud position and perform the analysis of the images considering $\beta(i,j) = \bar{\beta}$.

The images in Fig. 2.6(b) are taken with a 3μs pulse in order to avoid the atomic blurring due to photon scattering. The imaging pulses are so short that we cannot stabilize the intensity of the imaging beam easily. For this reason we have crosschecked that the intensity of the probe beam is stable from shot to shot to the 5% level. Moreover, we have observed that the intensity of the bright image I_{B} is systematically 10% higher than the intensity on the atoms image I_{A}. We take this into account to extract the polarization phase shift θ_A, which is shown in Fig. 2.6(c).

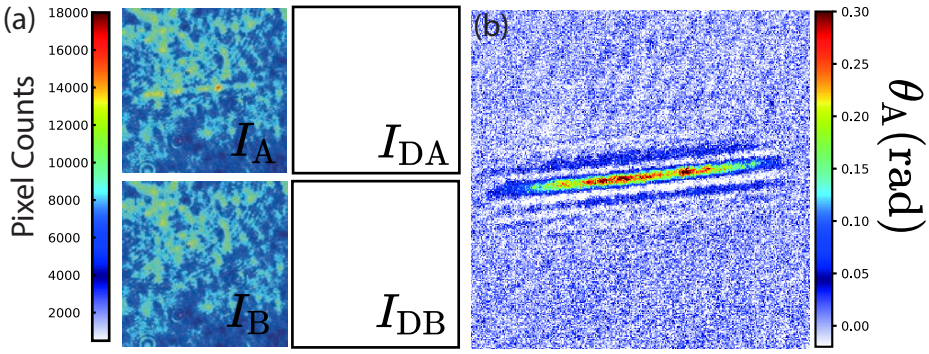

Figure 2.9: (a) Images taken with the EMCCD camera in the $\theta = \pi/4$ configuration. In this configuration the probe beam is split evenly in the two ports of the polarization analyzer. Top left: I_{A}. Bottom left: I_{B}. Top right: I_{DA}. Bottom right: I_{DB}. The color scale shows the pixel counts. (b) Atomic polarization phase shift retrieved from the images in (a). The color scale shows θ_{A}.

In the $\theta = \pi/4$ configuration we have that

[8] In the experiments performed in chapters 3 and 4 the waist was 1 mm. In the experiments performed in chapter 5 the beam waist was reduced to 0.5 mm due to the installation of the addressing microscope.

$$\frac{I_{\mathrm{A}} - I_{\mathrm{DA}}}{2\,(I_{\mathrm{B}} - I_{\mathrm{DB}})} = \sin^2\left(\theta_{\mathrm{A}} + \frac{\pi}{4}\right) \approx \theta_{\mathrm{A}} + \frac{1}{2}. \tag{2.3.3}$$

For small θ_{A} the signal is proportional to θ_{A}. In Fig. 2.9(a) we show the I_{A}, I_{B}, I_{DA} and I_{DB} pictures taken in such configuration. Fig. 2.9(b) shows the retrieved polarization phase shift θ_{A}.

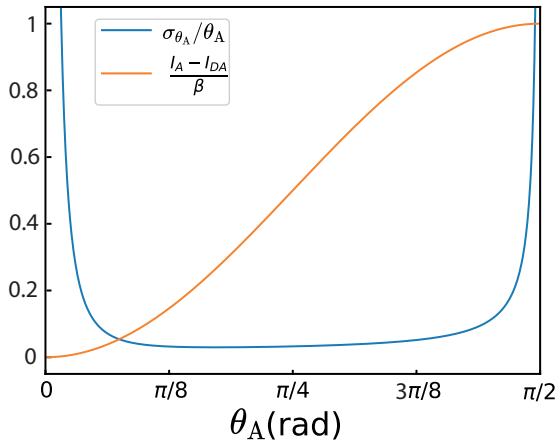

Figure 2.10: Orange: Atomic signal scaled $\sin^2(\theta_A)$. Blue: Relative error on the atomic polarization rotation $\sigma_{\theta_{\mathrm{A}}}/\theta_{\mathrm{A}}$.

Since the polarization phase contrast technique is non-linear the signal to noise ratio for different θ_{A} is different. In the dark field configuration the relative error on θ_{A} is really big for $\theta_{\mathrm{A}} \approx 0, \pi/2$, see Fig. 2.10. Instead, for $\theta = \pi/4$ the relative error on θ_{A} should be smaller at $\theta_A \approx 0$ and bigger for $\theta_{\mathrm{A}} \approx \pm\pi/4$. However, if we compare Fig. 2.6(c) and 2.9(b) we observe that for similar $\theta_{\mathrm{A}} \sim 0.3$ rad, the signal to noise ratio is smaller in the dark field configuration. Since the top bread board is just below the air conditioning of the experimental apparatus, it might be that there is air turbulence which slightly modifies the index of refraction in the imaging path in between the atom and bright images. Moreover, the $\theta = \pi/4$ configuration is limited to measure signals $\theta_{\mathrm{A}} < \pi/4$. For $\theta_{\mathrm{A}} > \pi/4$ the atomic signal I_{A} cannot be unequivocally related with a polarization rotation shift θ_{A}. Although the same phenomena happens in dark field, in this configuration the

range is twice as large. In order to extract the atomic phase shift of an atomic cloud when $\max(\theta_A(i,j)) > \pi/2$, we would need to use a phase unwrapping algorithm [110]. For this reason, and unless stated otherwise, we have decided to work in the dark field configuration.

Up to now we have explained how to retrieve the polarization phase shift θ_A. In order to relate the shift with a column density, we need to calibrate the Faraday coefficient c_F. In the following section I introduce the method that I have developed to calibrate the Faraday coefficient.

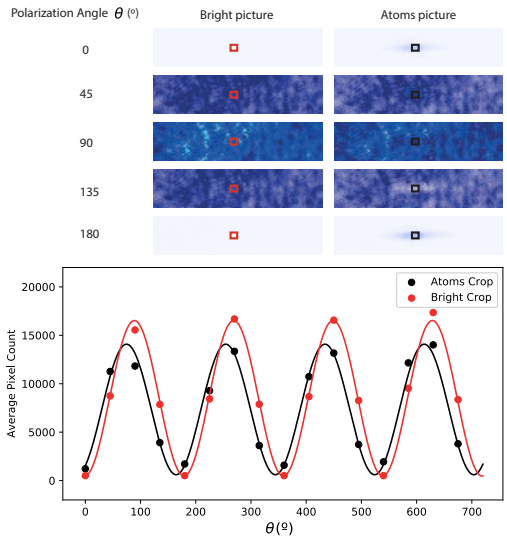

Figure 2.11: Scheme for calibrating the Faraday rotation induced by an atomic cloud. Top panel: bright I_B and atom I_A pictures taken for different input polarizations. The images are taken in a configuration where the imaging is destructive and there are no atoms left in the bright picture. Bottom panel: We measure the polarization phase shift on the light scattered by the atoms. The plot shows the average pixel counts on the area delimited in the figures from the top panel vs. the input polarization θ. To scan θ we rotate the $\lambda/2$ waveplate which is installed in the motorized rotating mount. As it can be seen there is a polarization shift θ_A between both curves. The difference in amplitude between the bright and atom pictures is due to the difference in intensity between the first and second imaging pulse.

2.3.4 Calibration of the Faraday coefficient

The main idea to calibrate the Faraday coefficient is to measure the polarization phase shift θ_{A} for different known column densities n_i in order to find the coefficient of proportionality $\theta_{\mathrm{A}} = c_{\mathrm{Fi}} n_i$. To do so, we probe a Bose-Einstein condensate with a well-known spatial density profile for different input linear polarizations. By contrast with the images taken in the absence of atoms we are able to observe the polarization phase shift θ_{A} introduced by the atoms, see Fig. 2.11.

In Fig. 2.12(a) and (b) we show the measurement of the polarization phase shift for different column densities at low (B = 57 G) and high field (B = 396 G). As it can be observed there is a linear relation between them. The proportionallity factor is the Faraday coefficient. To scan the column densities, we have probed the expansion dynamics of a BEC in an optical waveguide after releasing it from a crossed dipole trap. To calibrate the Faraday coefficient we need to calibrate the absolute atom number of the BECs which we probe. Before analyzing the results obtained in the measurements from Fig. 2.12(a) and (b) we will explain the method to calibrate the atom number.

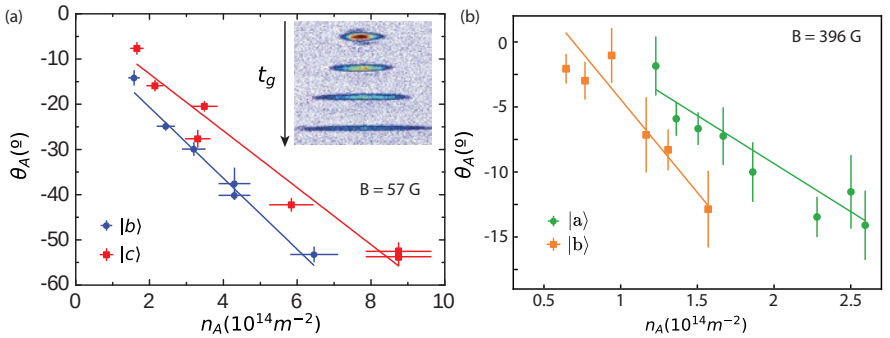

Figure 2.12: (a) Calibration of the Faraday coefficient c_F for B = 57 G and states $|b\rangle$ (blue circles) and $|c\rangle$ (red squares) at a detuning $\Delta_{BEAT}^{FAR} = 153$ MHz (see section C). We measure θ_A for various column densities that are scanned by expanding a BEC in an optical waveguide (see inset). (b) Calibration of the Faraday coefficient c_F for B = 396 G and states $|a\rangle$ (green circles) and $|b\rangle$ (orange squares) at a detuning $\Delta_{\mathrm{BEAT}}^{\mathrm{FAR}} = -515$ MHz (see section C).

Atom number calibration

In order to calibrate the Faraday coefficient it is very important to calibrate the atom number N. To do so we have used two different techniques. The first technique consists on measuring the critical temperature of Bose-Einstein condensation with time of flight absorption imaging as done in reference [65]. The critical temperature T_c of an interacting BEC in a trap is $T_c = T_c^0 + \delta T_c^{\rm int} + \delta T_c^{\rm size}$ [111], where $T_c^0 \approx 0.94\hbar\omega N^{1/3}/k_{\rm B}$ is the critical temperature of the non-interacting BEC in the thermodynamic limit and $\delta T_c^{\rm int}/T_c^0 \approx -1.33aN^{1/6}/a_{\rm HO}$ and $\delta T_c^{\rm size}/T_c^0 \approx -0.73N^{-1/3}\bar{\omega}/\omega$ are the shifts due to the interactions and finite size of the BEC, see Fig. 1.21 from chapter 1. Here $k_{\rm B}$ is the Boltzmann constant, a is the scattering length, N is the atom number, $\bar{\omega} = (\omega_x + \omega_y + \omega_z)/3$, $\omega = (\omega_x\omega_y\omega_z)^{1/3}$ and $a_{\rm HO} = (\hbar/m\omega)^{1/2}$. Thus the relative error on the critical atom number N_c is given by:

$$\left(\frac{\sigma_{N_c}}{N_c}\right)^2 \approx \left(\frac{3\sigma_{T_c}}{T_c}\right)^2 + \left(\frac{3\sigma_\omega}{\omega}\right)^2, \tag{2.3.4}$$

where typical measurements on T_c and ω have relative errors on the order of 8% and 3% respectively. Therefore this technique allows us to measure the atom number with relative uncertainties of $\sim 25\%$.

The second technique consists on measuring the expansion of a BEC in an optical dipole trap in the Thomas-Fermi regime. In this regime the size of the BEC after expansion follows a scaling law such that:

$$R_{\rm TFx}(t) = \lambda(t)R_{\rm TFx}(t=0), \tag{2.3.5}$$

where $\lambda(t)$ is a function that only depends on the initial and final trap frequencies [112]. To measure the Thomas-Fermi radius $R_{\rm TFx}$ in trap, we compute $\lambda(t)$ for our experimental parameters and fit the measured $R_{\rm TFx}(t)$ with the scaling law from equation 2.3.5 leaving $R_{\rm TFx}(t=0)$ as a free parameter. Moreover, in this regime the Thomas-Fermi radius of the BEC in the trap is:

$$R_{\rm TFx} = \sqrt{\frac{2\mu}{m\omega_x^2}}, \tag{2.3.6}$$

where $\mu = \frac{1}{2}(15Na\hbar^2\sqrt{m}\omega_x\omega_y\omega_z)^{2/5}$ is the chemical potential, m is the mass of ^{39}K, $\omega_{x,y,z}$ are the trap frequencies. Hence, the atom number is:

$$N = \frac{m^2\omega_x^4 R_{\mathrm{TFx}}^5}{15\hbar^2 a\omega_y\omega_z}, \tag{2.3.7}$$

and we can extract the atom number from the measured trapping frequencies and R_{TFx}. In this case the main relative error on the calibration of the atom number comes from the measurement of ω_x and R_{TFx}:

$$\left(\frac{\sigma_N}{N}\right)^2 \approx \left(\frac{4\sigma_{\omega_x}}{\omega_x}\right)^2 + \left(\frac{5\sigma_{R_{\mathrm{TFx}}}}{R_{\mathrm{TFx}}}\right)^2, \tag{2.3.8}$$

where typical measurements on ω_x and R_{TFx} have relative errors on the order of 1% and 3% respectively. Therefore this technique allows us to measure the atom number with relative uncertainties of $\sim 16\%$. Additionally, a systematic uncertainty which underestimates the atom number is introduced due to the Thomas-Fermi approximation. For typical parameters used in the calibration of the Faraday coefficient the radius computed by solving the Gross-Pitaevskii equation numerically (for an equivalent atom number and scattering length) is $\sim 3\%$ smaller than the Thomas-Fermi radius from equation (2.3.6). We include this systematic correction to calibrate the atom number.

We have crosschecked that both calibration methods agree with each other. Although the second technique may seem more precise, it is more prone to systematic errors on the measurement. Thus, we normally attribute a 25% error to the Faraday coefficient unless stated otherwise. In the future, we could improve the calibration on the atom number by using the technique described in reference [96].

In the following section we summarize the errors on the measurement of the column density.

Column density errors

The column density of an atomic cloud is extracted from $n_i = \theta_{\mathrm{A}}/c_{\mathrm{Fi}}$. Hence, the relative column density error is given by the following equation:

$$\left(\frac{\sigma_{n_\mathrm{A}}}{n_\mathrm{A}}\right)^2 = \left(\frac{\sigma_{\theta_\mathrm{A}}}{\theta_\mathrm{A}}\right)^2 + \left(\frac{\sigma_{c_\mathrm{F}}}{c_\mathrm{F}}\right)^2 \tag{2.3.9}$$

Therefore we need to take into account the error on the measurement of the Faraday coefficient as well as the error in the measurement of θ_A. As introduced previously, the sinusoidal dependence of I_A on θ_A imposes certain limits on the applicability of this imaging technique. On the one hand, $\theta_\mathrm{A}(I_\mathrm{A})$ is not a single-valued function. We have restricted the application of this technique to signals such that $\theta_\mathrm{A} < \pi/2$. On the other hand, the error on the retrieval of θ_A is really big for $\theta_\mathrm{A} \sim 0, \pi/2$, see Fig. 2.10.

In summary, in the dark field configuration, the error on the measurement on the column density can be limited either by the 25% error on the calibration of the atom number or by the measurement of θ_A for $\theta_\mathrm{A} \approx 0, \pi/2$. For reference, if we limit ourselves to $\sigma_{\theta_\mathrm{A}}/\theta_\mathrm{A} < \sigma_{c_\mathrm{F}}/c_\mathrm{F}$, we are limited to measure column densities on the range (0.1 rad/c_F, 1.5 rad/c_F).

2.3.5 Results

In the previous sections we have developed the methods to retrieve the atomic polarization phase shift, calibrate the Faraday coefficients and extract the column densities using a polarization phase contrast technique. In this section, we will first discuss the measurements performed for a single spin state and then we will show how this technique can be used to image a spin mixture to extract the total column density and the spin column density imbalance.

Experimental measurement of the Faraday coefficient

The calibration of the Faraday coefficients which have been performed at low (B = 57 G) and high field (B = 396 G) are shown in Fig. 2.12(a) and (b) and are summarized in table 2.1. All the measurements have been performed using a 3 μs imaging pulse with 250 mW/cm^2 peak intensity. The imaging beam that we have used to probe the $|b\rangle$ and $|c\rangle$ states at $B = 57$ G is red detuned by -17.5Γ and -12.2Γ from the closest transitions to measure the total atom number (black arrow in Fig. 2.4 which corresponds to $\Delta^{\mathrm{FAR}}_{\mathrm{BEAT}} = 153$ MHz). The imaging beam

that we have used to probe the $|a\rangle$ and $|b\rangle$ states at $B = 396$ G is red detuned by -44.7Γ and -29.7Γ from the closest transitions to measure the total atom number (black arrow in Fig. 2.4, which corresponds to $\Delta^{\mathrm{FAR}}_{\mathrm{BEAT}} = -515$ MHz). For these detunings, the imaging is destructive. As it can be seen in Fig. 2.6(b) and Fig. 2.9(a) there are no atoms in the bright image I_{B}. However, the imaging pulse is so short that the photon recoil does not blur the atoms image. Moreover we have crosschecked that the response of the atomic cloud is linear with the intensity and that no saturation and lensing effects are observed at these detunings (see appendix C for details).

Since the transitions that we probe are not closed, atoms may fall into other states during the exposure. This process is called optical depumping and is produced by the spontaneous emission of the excited states to other ground states. The characteristic time $\tau \sim 10\ \mu s$ of this process is very similar for both fields. Hence, 25% of the atoms fall into other ground states and the effective Faraday coefficient may differ from the theoretical expectations (see appendix C for details).

Whereas at low field there is a discrepancy between the measured and theoretical Faraday coefficient, at high field the measurements agree well with theory. This is presumably due to the fact that the imaging at high field is farther from resonance than at low field and the fact that at high field the optical transitions have more resemblance with a two-level system.

Additionally, we have performed an independent crosscheck at low field by transferring $|c\rangle$ to the $|d\rangle = |m_I = -3/2, m_J = -1/2\rangle$ streched state (see Fig. 2.3) and probing the cycling transition:

$$|m_I = -3/2, m_J = -1/2\rangle \rightarrow |m_{I'} = -3/2, m_{J'} = -3/2\rangle \tag{2.3.10}$$

This allows us to compare our calibration with the expected two-level system prediction, finding good agreement. Second, by transferring a variable fraction of atoms to $|m_I = -3/2, m_J = -1/2\rangle$, we confirm the linearity of our imaging scheme and rule out the existence of collective atom-light interaction effects in the imaging.

In summary we have been able to characterize the effective Faraday coeffi-

cients at B = 57 G for the $|b\rangle$ and $|c\rangle$ states and at B = 396 G for the $|a\rangle$ and $|b\rangle$ states. This allows us to measure the column density of each state and extract its size and atom number. But how does the imaging perform in the presence of a mixture?

B (G)	$\Delta^{\mathrm{FAR}}_{\mathrm{BEAT}}$ (MHz)	$\|state\rangle$	$c_{\mathrm{F}}^{\mathrm{exp}}(10^{-15} rad \cdot m^2)$	$c_{\mathrm{F}}^{\mathrm{th}}(10^{-15} rad \cdot m^2)$
57	153	b	-1.4	-2.44
57	153	c	-1.1	-2.24
396	-515	a	-1.3	-1.47
396	-515	b	-2.6	-2.21

Table 2.1: Summary of the Faraday coefficients c_F which have been measured at low (B = 57 G) and high field (B = 396 G) for ^{39}K. The relative error on the Faraday coefficient is 25%.

Imaging mixtures *in situ*

In the presence of a mixture the polarization rotation contains the contribution of both components and is described by equation (2.2.24). As explained previously there are two interesting cases: if $c_{\mathrm{F1}} = c_{\mathrm{F2}}$, θ_{A} reflects the sum of the column densities whereas if $c_{\mathrm{F1}} = -c_{\mathrm{F2}}$ it reflects the difference.

The experiments performed in chapters 3, 4 and 5 are done in a configuration where $c_{\mathrm{F1}} \approx c_{\mathrm{F2}}$ to measure the total atom number. Moreover, we have started to explore the regime where $c_{\mathrm{F1}} \approx -c_{\mathrm{F2}}$ at high field in order to measure the difference of column densities. We have performed some experiments in the linear configuration $\theta = \pi/4$ with light whose frequency lies in the middle of the $|a\rangle \rightarrow m_{J'} = -3/2$ and $|b\rangle \rightarrow m_{J'} = 1/2$ transitions where $c_{Fa} \approx -c_{Fb}$. This light is is red (blue) detuned from the $|a\rangle$ ($|b\rangle$)$\rightarrow m_{J'} = -3/2(1/2)$ transitions by 7.5Γ (red arrow in Fig. 2.5).

To illustrate the ability to image a mixture insitu we prepared a BEC in state $|a\rangle$ in an optical dipole trap formed by two intersecting beams. We switched off the vertical beam and let the BEC expand in a waveguide[9] to reduce its density and avoid lensing effects. Then we apply a radio-frequency pulse for a variable

[9]The waveguide is aligned within the depth of focus of the imaging objective.

time to transfer atoms to state $|b\rangle$ and immediately image the cloud *in situ*. With this method we ensure that the density profile of both states is identical and only the ratio of population is modified. In Fig. 2.13 we can observe the signal of the Rabi oscillations measured *in situ*. In this case:

$$\theta_{\mathrm{A}} = \frac{n}{2}\left[(c_{\mathrm{Fb}} - c_{\mathrm{Fa}})P + (c_{\mathrm{Fb}} + c_{\mathrm{Fa}})\right], \tag{2.3.11}$$

where n is the total column density $n = n_a + n_b$ and P is the polarization $P = \frac{n_b - n_a}{n_b + n_a}$. The column densities we used are such that θ_{A} is small and therefore we can use the linear approximation from equation (2.3.3). If all atoms are in state $|a\rangle$ ($|b\rangle$) we expect that $\theta_{\mathrm{A}} = c_{\mathrm{Fa}} n (c_{\mathrm{Fb}} n)$. Since $c_{Fa} \approx -c_{Fb}$ we expect that the polarization rotates in opposite directions and in equal amount, as it is observed in Fig. 2.13.

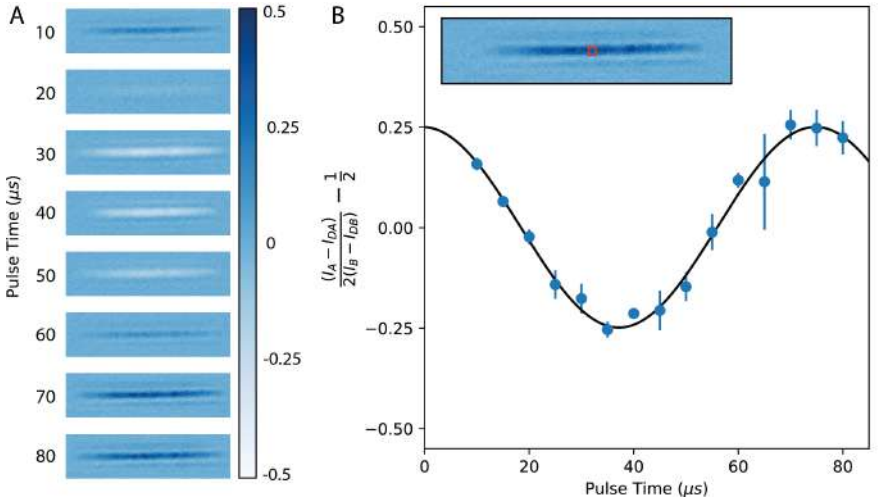

Figure 2.13: Rabi oscillations measured in situ in the linear configuration for B = 396 G and $\Delta_{\mathrm{BEAT}}^{\mathrm{FAR}} = -292$ MHz. (a) Images of the signal vs. pulse time. The colorbar corresponds to the value of $\frac{I_{\mathrm{A}} - I_{\mathrm{DA}}}{2(I_{\mathrm{B}} - I_{\mathrm{DB}})} - \frac{1}{2}$. (b) $\frac{I_{\mathrm{A}} - I_{\mathrm{DA}}}{2(I_{\mathrm{B}} - I_{\mathrm{DB}})} - \frac{1}{2}$ vs. pulse time. The inset shows the cropped region used to average the signal. Blue points: Measurement. Black line: Fit to $A \cdot \sin(\Omega t) + B$

In Fig. 2.14 we represent the data plotted in Fig. 2.13 with respect to the polarization P. We can observe that there is a linear relation between θ_{A} and P.

By doing a linear fit we obtain that $c_{\mathrm{Fb}}/c_{\mathrm{Fa}} = -1.01(25)$ as expected. Therefore, with this technique we can measure the difference in column densities between both spin states.

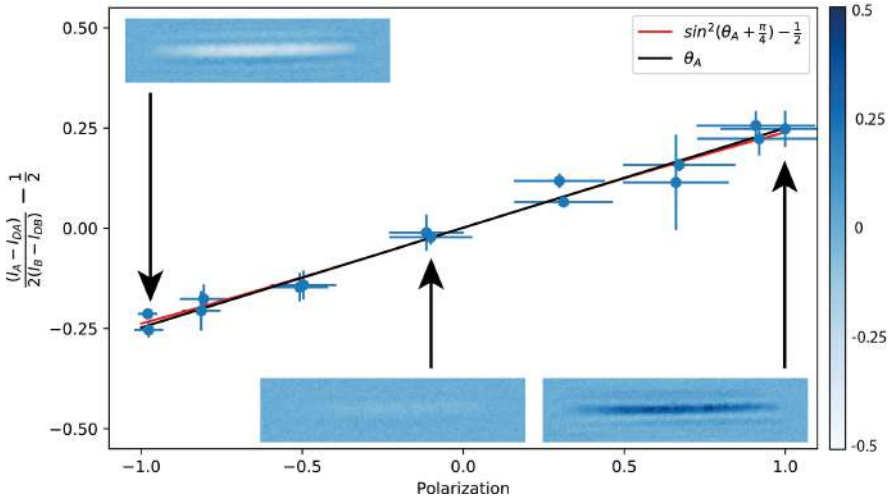

Figure 2.14: Spin dependent imaging. We plot $\frac{I_{\mathrm{A}}-I_{\mathrm{DA}}}{2(I_{\mathrm{B}}-I_{\mathrm{DB}})} - \frac{1}{2}$ vs. polarization measured at $B = 396$ G and $\Delta^{\mathrm{FAR}}_{\mathrm{BEAT}} = -292$ (blue circles). Black line: Fit to $A \cdot P + B$. Red line: We plot $\sin^2(A \cdot P + B + \pi/4)$ for comparison. The insets show exemplary figures for all atoms in $|a\rangle$, a balanced mixture and all atoms in $|b\rangle$.

2.4 Conclusions and outlook

In conclusion, we have developed an imaging method based on the Faraday effect in order to probe the real space distribution of an atomic cloud *in situ* at different magnetic fields. In particular, we have focused on the measurement of the effective Faraday coefficient at B = 57 G and B = 396 G in non-closed transitions. We have measured a Faraday coefficient for the $|b\rangle$ and $|c\rangle$ states of $c_{\mathrm{Fb}} = -1.4 \cdot 10^{-15}\mathrm{rad} \cdot \mathrm{m}^2$ and $c_{\mathrm{Fc}} = -1.1 \cdot 10^{-15}\mathrm{rad} \cdot \mathrm{m}^2$ at low field and $c_{\mathrm{Fa}} = -1.3 \cdot 10^{-15}\mathrm{rad} \cdot \mathrm{m}^2$ and $c_{\mathrm{Fb}} = -2.6 \cdot 10^{-15}\mathrm{rad} \cdot \mathrm{m}^2$ for the $|a\rangle$ and $|b\rangle$ ground states at high field in fair agreement with the theoretical predictions.

This configuration allows us to measure the total column density of the cloud, regardless of the spin composition. Finally, we have explored a regime at B = 396 G in which the Faraday coefficients of the $|a\rangle$ and $|b\rangle$ states are opposite and allow to measure the difference in column density.

Currently, we are working to extend this technique in order to measure both the sum and difference of column densities. Performing a non-destructive imaging pulse further from resonance would allow to measure the sum. A second imaging pulse in the middle of both transitions would allow to measure the difference. Since lensing effects may play an important role closer to resonance, we will consider performing highly saturated absorption imaging exactly on resonance to measure the composition of a single state and be able to retrieve the difference in column densities. The implementation of this method remains as a future perspective.